Draft version September 6, 2019
Typeset using LaTeX **twocolumn** style in AASTeX63

The CARMA-NRO Orion Survey: Protostellar Outflows and Filamentary Alignment

Jesse R. Feddersen,[1] Héctor G. Arce,[1] Shuo Kong,[1] You?,

[1] *Department of Astronomy, Yale University, P.O. Box 208101, New Haven, CT 06520-8101, USA*

ABSTRACT

We identify 45 protostellar outflows in CO maps of the Orion A giant molecular cloud from the CARMA-NRO Orion survey. Our sample includes 11 newly detected outflows. We measure the mass and energetics of the outflows, including material at low-velocities by correcting for cloud contributions. The total momentum and kinetic energy injected by outflows is comparable to the turbulent dissipation of the cloud. We also compare the outflow position angles to the orientation of $C^{18}O$ filaments. We find that the full sample of outflows is consistent with being randomly oriented with respect to the filaments. A subsample of the most reliable measurements shows a moderately perpendicular outflow-filament alignment which may reflect accretion of mass across filaments and onto the protostellar cores.

Keywords: ISM: clouds — ISM: individual objects (Orion A) — stars: formation

1. INTRODUCTION

Stars form inside the densest parts of giant molecular clouds (GMCs) (McKee & Ostriker 2007). Bipolar, high-velocity flows of molecular gas, called outflows, are launched from forming protostars. These structures are so ubiquitous they can be observed even when the protostar itself is unseen (Kong et al. 2019). While it is unclear how exactly outflows are launched, they likely arise from the interaction of the accretion disk with magnetic fields near the protostar (e.g. Konigl & Pudritz 2000; Shu et al. 2000; Frank et al. 2014).

Outflows have long been sought as a mechanism for sustaining turbulence and slowing star formation in GMCs (Nakamura & Li 2007; Carroll et al. 2009; Federrath 2015). Surveys of outflows have repeatedly shown that they have enough aggregate momentum and kinetic energy to significantly offset the dissipation of turbulence, especially on cluster scales (Arce et al. 2010; Nakamura et al. 2011; Plunkett et al. 2013; Plunkett et al. 2015; Li et al. 2015). More uncertain is the efficiency with which outflows inject momentum at larger scales in order to maintain the observed turbulence in GMCs (Brunt et al. 2009; Padoan et al. 2009; Carroll et al. 2010). For a comprehensive review of outflows, see Bally (2016).

In many GMCs, most of the star formation takes place in relatively narrow, dense filaments (Arzoumanian et al. 2011; Suri et al. 2019). If the angular momentum of a growing protostar is inherited from the mass accretion onto a filament, the protostellar spin and the filament direction will be correlated (Bodenheimer 1995; André et al. 2014; Li & Klein 2019). If, however, the link between mass accretion at filament scales and protostellar scales is disrupted, e.g. by turbulence or interaction with protostellar companions, then the protostellar spin may not be correlated with the filament orientation (Offner et al. 2016; Lee et al. 2017).

To distinguish between these scenarios, several studies have recently considered the relative orientation of outflows and filaments. Assuming the outflow direction traces the angular momentum of the protostar, a correlation between the outflow and filament direction could mean a connection between scales as small as a few hundred AU, where the outflow is launched, to the 0.1 pc width of a typical filament. Davis et al. (2009) measured the position angle of H_2 outflows in the Orion A GMC and found no correlation with the large-scale integral-shaped-filament (ISF). Stephens et al. (2017) compared CO outflows with filaments extracted from *Herschel* dust maps in the Perseus molecular cloud and likewise found a random outflow-filament alignment. However, Kong et al. (2019) recently found a preferentially perpendicular outflow-filament alignment in the IRDC G28.37+0.07

The Orion A GMC is an ideal environment for studying protostellar outflows and their connection to fila-

jesse.feddersen@yale.edu

ments. At a distance of 414 pc (Menten et al. 2007), [1] it is one of the closest clouds forming both low- and high-mass stars. Following earlier outflow studies, Tanabe et al. (2019, submitted) recently carried out a systematic search of CO outflows in Orion. While our study overlaps with theirs, we use different methods to identify outflows and derive their physical properties. We also use the $C^{18}O$ filament catalog from Suri et al. (2019) for an entirely new analysis of the outflow-filament connection.

In this paper, we present a study of protostellar outflows in the CARMA-NRO Orion survey. In Section 2, we describe the CARMA-NRO Orion CO data and protostar catalogs. In Section 3, we describe how we search for outflows in the CO maps and present the outflow catalog. In Section 4, we calculate the physical properties of the outflows and discuss their impact on the cloud. In Section 5, we discuss the relative orientation of outflows and $C^{18}O$ filaments and compare to models for random, parallel, and perpendicular outflow-filament alignment. Finally, in Section 6, we summarize our conclusions and discuss future directions. The entire outflow catalog is presented in the Appendix.

2. OBSERVATIONS

2.1. *CO Maps*

The CARMA-NRO Orion survey combines interferometric observations from the Combined Array for Research in Millimeter-wave Astronomy (CARMA) with single-dish observations from the 45 m telescope at the Nobeyama Radio Observatory (NRO). The combination of interferometric and single-dish observations results in an unprecedented spatial dynamic range of 0.01 - 10 pc in the Orion A molecular cloud.

We use the $^{12}CO(1\text{-}0)$, $^{13}CO(1\text{-}0)$, and $C^{18}O(1\text{-}0)$ data first presented in Kong et al. (2018). The ^{12}CO data have a resolution of $10'' \times 8''$ and velocity resolution of 0.25 km s^{-1}. The original ^{13}CO data have a resolution of $8'' \times 6''$ and a velocity resolution of 0.22 km s^{-1}, but we smooth the ^{13}CO data to match the resolution of ^{12}CO. The $C^{18}O$ data have a resolution of $10'' \times 8''$ and a velocity resolution of 0.22 km s^{-1}.

2.2. *Source Catalogs*

We primarily use the Herschel Orion Protostar Survey (HOPS; Furlan et al. 2016) to assign driving sources to outflow. The HOPS catalog is the result of *Herschel* PACS 70-160 μm observations of the protostars identified in the *Spitzer* Orion survey by Megeath et al. (2012). Furlan et al. (2016) fit the spectral energy distribution (SED) of these 330 protostars from 1.2-870 μm with models to derive a variety of protostar, disk, and envelope properties.

We also use the study of H_2 outflows by Davis et al. (2009) to guide our search. Davis et al. (2009) surveyed Orion A using narrow-band images of the ro-vibrational H_2 2.122 μm line. Their work builds on previous H_2 mapping by Stanke et al. (2002). We search for outflows around the 17 sources of H_2 flows that are not in the HOPS catalog. In addition to the driving sources of H_2 outflows, Davis et al. (2009) catalog H_2 features with no obvious driving source. We also search for the CO counterpart to the 29 H_2 flows without an identified source within the CO data footprint. Davis et al. (2009) measure the proper motions of 33 flows. We use the H_2 images and, when available, the proper motions to help assign especially difficult CO outflows to driving sources.

2.3. *Other Outflow Studies*

Orion A has been mapped extensively in CO over the past 30 years (e.g. Bally et al. 1987; Wilson et al. 2005; Shimajiri et al. 2011; Buckle et al. 2012; Ripple et al. 2013; Berné et al. 2014). Several studies have searched for outflows in the cloud using these CO observations. In the northern part of the cloud, previous searches have identified 18 outflows along the OMC 2/3 ridge (Chini et al. 1997; Aso et al. 2000; Williams et al. 2003; Takahashi et al. 2008; Shimajiri et al. 2008, 2009). In the L1641N cluster in the southern part of the cloud, Stanke & Williams (2007) and Nakamura et al. (2012) found six outflows. In the NGC 1999 region further south, previous studies have found five outflows (Morgan et al. 1991; Moro-Martín et al. 1999; Davis et al. 2000; Choi et al. 2017).

Tanabe et al. (2019, submitted) have carried out a systematic search for outflows across the Orion A cloud, using the same single-dish NRO observations which are used in our CARMA-NRO Orion survey. They identify a total of 44 outflows across the cloud, including 17 new detections. Eleven of these are in the OMC 4/5 region where no outflows had previously been found. Although we expect our catalog to largely overlap with Tanabe et al. (2019, submitted), they use an automated outflow search procedure which may include false positives. We describe our procedure for identifying outflows below.

3. OUTFLOW IDENTIFICATION

[1] We adopt a distance of 414 pc throughout this paper to be consistent with Tanabe et al. (2019, submitted). Recent parallax measurements from GAIA Data Release 2 place Orion A slightly closer, at 380-400 pc (Kounkel et al. 2018; Großschedl et al. 2018; Kuhn et al. 2019).

We search for CO outflows around every HOPS protostar in Furlan et al. (2016) and every source of an H_2 jet in Davis et al. (2009). For each source, we first fit an average ^{12}CO spectrum with a Gaussian. Next, we integrate the ^{12}CO emission farther than 2σ away from the mean velocity on either side. We inspect the contour maps of the blue-shifted and red-shifted emission to look for collimated structures centered on the source which are detected above 5σ in these integrated blue- and red-shifted intensity maps.

In addition to the ^{12}CO blue/red contour maps, we use NIR images from the VISTA survey (Meingast et al. 2016) and the H_2 outflows in Davis et al. (2009) to guide our assignment of high-velocity CO to driving sources. These ancillary data are especially useful in areas of overlapping outflows, or where outflow lobes are spatially removed from the driving source. When a series of H_2 bow shocks or NIR nebulosity which are clearly associated with a particular source overlap a region of high-velocity CO emission, we can be more confident in the assignment of this CO outflow to its source.

Tanabe et al. (2019, submitted) automatically defines any blue or redshifted emission above 5σ near a protostar as an outflow. By restricting our catalog to structures that have the expected morphology, or are correlated with H_2 flows, we limit the risk of false positives. Several of the outflows in Tanabe et al. (2019, submitted) are not included here for these reasons (see Table 1).

Some regions (e.g. OMC 2/3) contain several overlapping outflows. In these cases, we try to follow previous authors' assignment of the high-velocity emission, unless we strongly disagree with their assessment. In Section 4.1.1, we describe the outflow region extraction.

Once we have identified an outflow, we adjust the velocity range over which we integrate ^{12}CO to produce contour maps that most clearly separate the blue/red lobes from surrounding cloud emission. Table 1 lists these visually determined velocities ($v_{\rm blue}$ and $v_{\rm red}$).

For each outflow, we determine a confidence rating of "Definite" or "Marginal". Definite outflows are clearly associated with their driving source, are clearly distinct from surrounding outflows and cloud emission, and are often clearly correlated with H_2 outflows. Most definite outflows have been identified previously. Marginal outflows either have an unclear source assignment, are not clearly separated from the cloud or overlapping outflow emission, or are simply very weakly detected. In some cases, we are more confident of either the blue or red outflow lobe, so we assign confidence ratings independently to each. We expect the subset of definite outflows will have more reliable physical properties and position angles (see Section 4).

While many studies have identified energetic outflows in the OMC 1 region (e.g. Schmid-Burgk et al. 1990; Zapata et al. 2005; Teixeira et al. 2016; Bally et al. 2017), we avoid this region in our outflow search. Neither Davis et al. (2009) nor Furlan et al. (2016) cover the central part of the Orion Nebula, due to saturation and confusion with the bright nebulosity. Aside from the lack of good source catalogs in this region, the CO velocity dispersion in OMC 1 is as high as 100 km s^{-1}, due to the BN/KL "explosion" (Bally et al. 2017), making it hard to define blue/red outflow lobes. Thus, in this study we focus our outflow search outside of OMC 1.

In total, we identify 45 outflows with 67 individual lobes. Of these, 11 were not identified by Tanabe et al. (2019, submitted). We do not detect 10 of the outflows included in Tanabe et al. (2019, submitted). Most of these non-detections consist of the most dubious outflows in that study, which we suspect are spurious due to the automated identification method they use. Of the 67 outflow lobes, we classify 38 as "definite" and 29 as "marginal". Table 1 lists the source, location, $v_{\rm blue}$ and $v_{\rm red}$, confidence score, and the corresponding outflow in Tanabe et al. (2019, submitted) for our entire catalog. Figure 1 shows the outflow catalog on a map of the peak ^{12}CO temperature.

Figure 2 shows an outflow in OMC 2 driven by HOPS 68. This outflow is well-known in the literature (Outflow 12 in Tanabe et al. 2019, submitted and FIR 2 in Takahashi et al. 2008). We use this outflow in Figures 3-9 to demonstrate our methods for calculating outflow properties. We present the entire outflow catalog in Appendix B.

4. PHYSICAL PROPERTIES OF OUTFLOWS

4.1. *Calculating Physical Properties*

To calculate the physical properties of outflows, we adapt the methods described by Arce & Goodman (2001), Dunham et al. (2014), and Zhang et al. (2016).

4.1.1. *Extracting Outflow Emission*

To measure the outflow mass, we must first extract each outflow from the surrounding cloud. This is particularly difficult in Orion, where many outflows are clustered and overlapping. We use a two-step approach to extract each outflow lobe.

First, we integrate the ^{12}CO cube over the visually estimated velocity range of the outflow lobe (discussed in Section 3). We select pixels above 5σ in this integrated map of high-velocity emission, excluding insignificant noise from the outflow. Next, we draw a region around each outflow lobe by hand to remove other overlapping outflows or other cloud structures in the area.

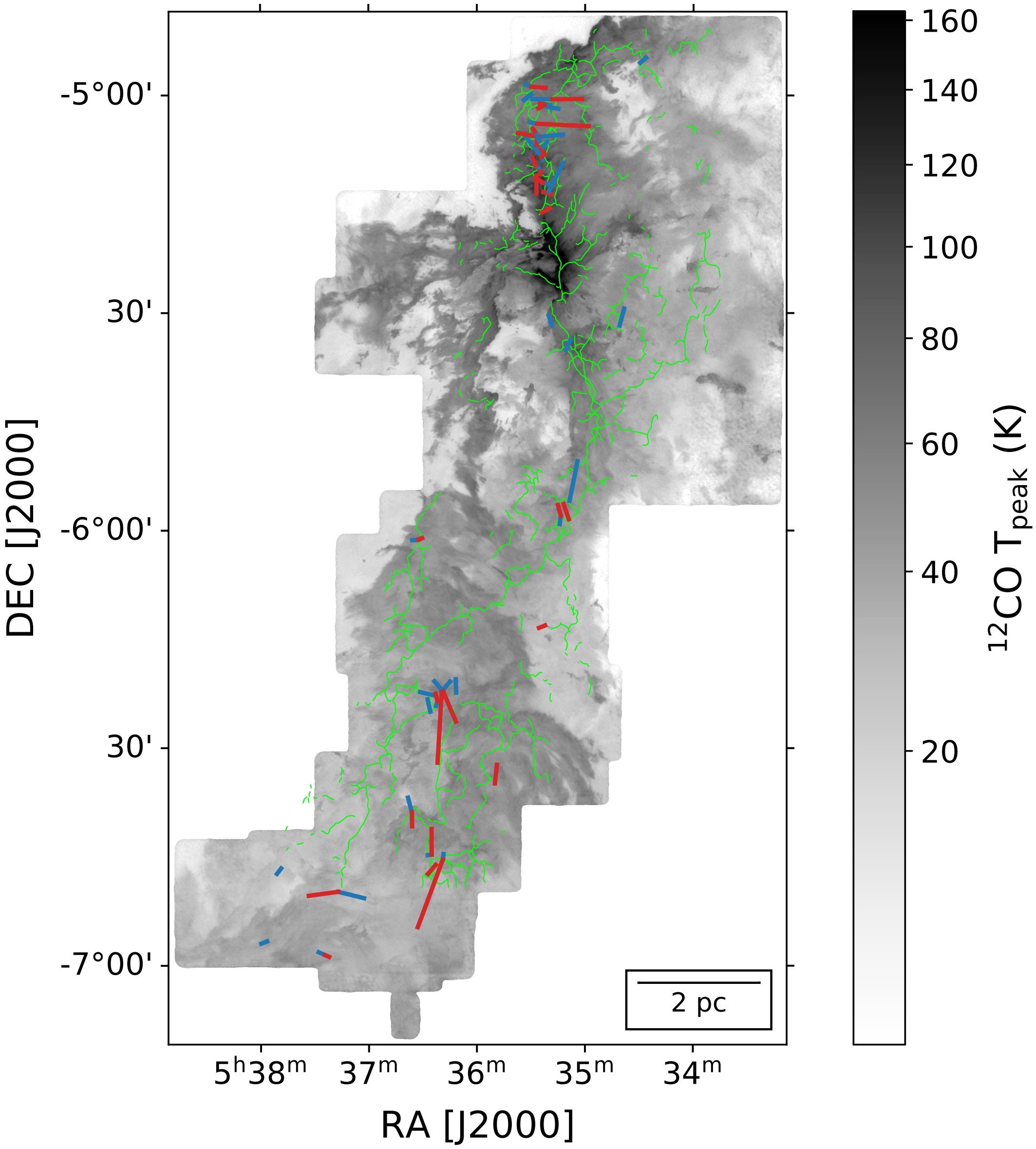

Figure 1: Peak ^{12}CO temperature in Orion A with outflows. The blue (red) lines indicate blue (red) outflow lobes. The length of the lines denote the maximum length of the outflow lobe, $R_{\rm max}$(Section 4.1.8. The orientation of the outflow lobes indicate the measured position angle (Section 4.1.9). The green lines indicate C^{18}O filaments from Suri et al. (2019) (Section 5).

To summarize, those pixels above 5σ in integrated high-velocity ^{12}CO and which are visually inside the outflow are included in determining the physical properties of the outflow. Figure 2 shows the regions extracted for the HOPS 68 outflow. The regions extracted for the other outflows are shown in the Appendix.

4.1.2. *Systemic Velocity*

To calculate outflow energetics, we need to know the systemic velocity $v_{\rm sys}$ of the outflow source. We use the CARMA-NRO Orion C^{18}O data (Kong et al. 2018) for this purpose. We fit a Gaussian model to the average C^{18}O spectrum within a 15″ radius around the outflow source and define the mean of this gaussian to be $v_{\rm sys}$. In most cases, there is only one significant velocity component in the C^{18}O spectrum. In the few outflows where multiple velocity components are detected, we use the velocity of the component with the highest peak intensity. Figure 3 shows the C^{18}O spectrum and fit for the HOPS 68 outflow.

4.1.3. *Excitation Temperature*

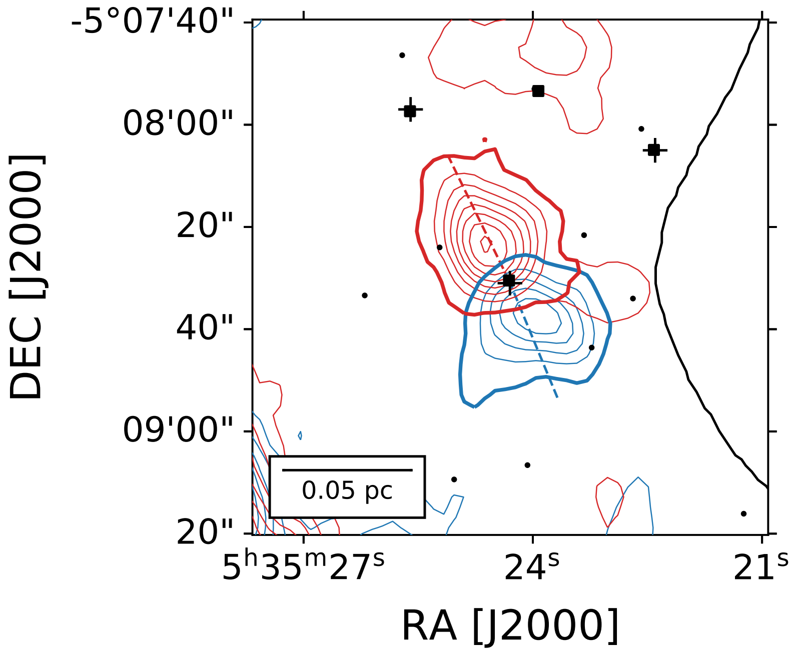

Figure 2: Outflow around HOPS 68. The blue (red) *contours* show ^{12}CO integrated from -2 km s^{-1} to $v_{\rm blue}$ ($v_{\rm red}$ to 20 km s^{-1}), where $v_{\rm blue}$ and $v_{\rm red}$ are given in Table 1. Contour levels go from 5 to 50σ, in steps of 5σ where σ is the RMS error in the integrated map. The *thick contours* show the region we extract for each lobe. The *shaded wedges* show the best-fit position angle and opening angle for the outflow lobes. The *black dotted line* shows the closest C^{18}O filament from Suri et al. (2019). *Black squares* indicate HOPS protostars from Furlan et al. (2016), *black crosses* indicate H_2 outflow sources from Davis et al. (2009), and small *black points* indicate all *Spitzer* YSOs from Megeath et al. (2012).

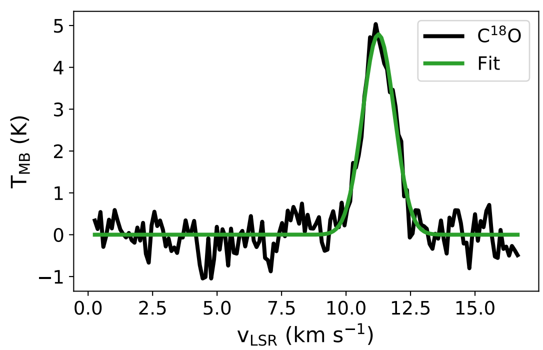

Figure 3: C^{18}O spectrum of the HOPS 68 outflow. The black line shows the average C^{18}O spectrum within a radius of 15″ around HOPS 68. The green line is a gaussian fit to the spectrum. We define the mean of this fit to be $v_{\rm sys}$ (see Section 4.1.2).

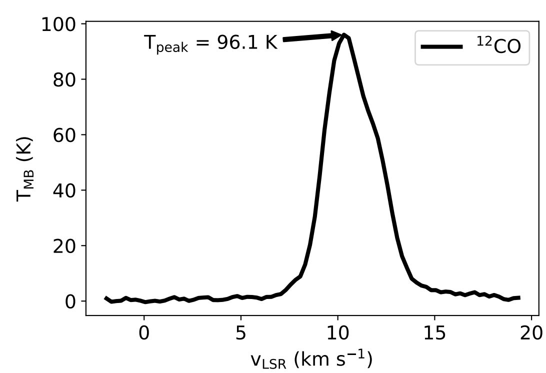

Figure 4: ^{12}CO spectrum of the HOPS 68 outflow. The black line shows the average ^{12}CO spectrum within the outflow mask shown in Figure 2. We use the peak of this spectrum, $T_{\rm peak}$, to calculate $T_{\rm ex}$ (see Section 4.1.3).

We estimate the excitation temperature of ^{12}CO, $T_{\rm ex}$, using the equation from Rohlfs & Wilson (1996), which assumes ^{12}CO is optically thick in the line core:

$$T_{\rm ex} = \frac{5.53}{ln(1 + [5.53/(T_{\rm peak} + 0.82)])}. \quad (1)$$

We define $T_{\rm peak}$ for each outflow to be the peak temperature of the average ^{12}CO spectrum toward the outflow area defined in Section 4.1.1. Figure 4 shows the average ^{12}CO spectrum with $T_{\rm peak}$ indicated for the HOPS 68 outflow.

4.1.4. ^{12}*CO Opacity Correction*

In Orion, ^{12}CO is usually optically thick (Kong et al. 2018). Therefore, if we do not correct for opacity we may miss a substantial amount of outflow mass. By comparing to more optically thin tracers, studies have long shown that outflows tend to be optically thick in ^{12}CO, at least at lower velocities (e.g., Goldsmith et al. 1984; Arce & Goodman 2001). Dunham et al. (2014) find that correcting for the optical depth of outflows increases their mass by a factor of 3 on average. Despite this, outflow studies that lack an optically thin tracer often assume that all ^{12}CO outflow emission is optically thin (e.g. in Orion, Morgan et al. 1991; Takahashi et al. 2008).

Tanabe et al. (2019, submitted) adopt an average ^{12}CO optical depth of 5 for their entire outflow catalog. They apply this constant correction factor to every velocity channel. But Dunham et al. (2014) show that the optical depth varies with velocity: optical depth decreases with increasing velocity away from the cloud core. We follow Dunham et al. (2014) and Zhang et al. (2016) and use the ratio of ^{12}CO / ^{13}CO to derive a velocity-dependent opacity correction for each outflow.

We assume both ^{12}CO and ^{13}CO are in LTE with the same excitation temperature and ^{13}CO is optically thin. Then the ratio between the two isotopes is

$$\frac{T_{^{12}\mathrm{CO}}}{T_{^{13}\mathrm{CO}}} = \frac{[^{12}\mathrm{CO}]}{[^{13}\mathrm{CO}]} \frac{1 - e^{-\tau_{12}}}{\tau_{12}}, \tag{2}$$

where we assume the abundance ratio [^{12}CO]/[^{13}CO] is 62 (Langer & Penzias 1993) and τ_{12} is the optical depth of ^{12}CO. In each velocity channel, we calculate the average ratio between ^{12}CO and ^{13}CO in pixels in the outflow region with both lines detected at 5σ or higher.

^{13}CO is usually too weak to be detected more than 2-3 km s^{-1} away from the line core. Thus we extrapolate the measured ratio spectrum by fitting it with a 2nd-order polynomial, weighting each velocity channel by the standard deviation of the ratio in that channel. For most of the outflows, we use a fitting range of 1.5 km s^{-1} on either side of the minimum ratio. This fitting range is adjusted for the few outflows with multiple velocity components to ensure that the component corresponding to v_{sys} is fit. For each velocity, we use the value of this fit and Equation 2 to calculate the correction factor $\tau_{12}/(1 - e^{-\tau_{12}})$ with which we multiply the observed ^{12}CO. Because the opacity correction factor cannot be less than unity for any value of τ_{12}, the ratio spectrum fit is capped at the value of [^{12}CO]/[^{13}CO] and in this regime we consider ^{12}CO optically thin. In Figure 5, we show an example of the ^{12}CO/^{13}CO ratio spectrum and fit for the HOPS 68 outflow.

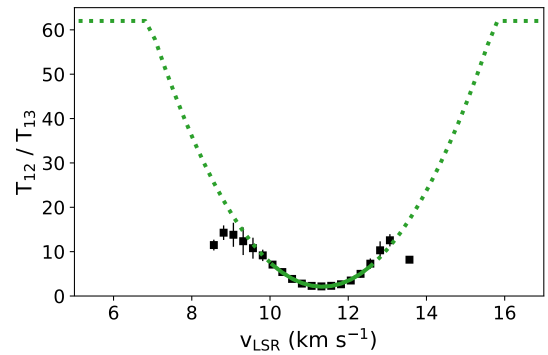

Figure 5: ^{12}CO/^{13}CO ratio of the HOPS 68 outflow. The black points show the average ratio between ^{12}CO and ^{13}CO in each velocity channel using only pixels where both lines are detected at 5σ. The error bars indicate the standard deviation of the ratio. The green parabola is the weighted least-squares fit to the ratio. The solid line shows the fitting range used, while the dotted line is an extrapolation of this fit. The parabola is capped at the assumed isotopic ratio of 62 (see Section 4.1.4).

4.1.5. *Outflow Mass*

After correcting for opacity, we use the ^{12}CO emission to calculate the H_2 column density in each velocity channel. From Equation A6 in Zhang et al. (2016),

$$\frac{dN}{dv} = \left(\frac{8\pi k \nu_{ul}^2}{hc^3 A_{ul} g_u}\right) Q_{\mathrm{rot}}(T_{\mathrm{ex}})\ e^{E_u/kT_{\mathrm{ex}}} \frac{T_R(v)}{f} \tag{3}$$

where $\nu_{ul} = 115.271$ GHz is the frequency of the ^{12}CO(1-0) transition, $A_{ul} = 7.203 \times 10^{-8}$ s^{-1} is the Einstein A coefficient, $E_u/k = 5.53$ K is the energy of the upper level, $g_u = 3$ is the degeneracy of the upper level, Q_{rot} is the partition function (calculated to $j = 100$), T_{ex} is the excitation temperature defined in Section 4.1.3, $T_R(v)$ is the opacity-corrected brightness temperature of ^{12}CO, and f is the abundance ratio of ^{12}CO/H_2. We assume an abundance ratio of $f = 1 \times 10^{-4}$ (Frerking et al. 1982).

We then calculate the mass in each voxel:

$$M = \mu_{\mathrm{H}_2} m_{\mathrm{H}} A_{\mathrm{pixel}} N_{\mathrm{H}_2}, \tag{4}$$

where $\mu_{\mathrm{H}_2} = 2.8$ is the mean molecular weight of H_2 (Kauffmann et al. 2008), $m_{\mathrm{H}} = 1.674 \times 10^{-24}$ g is the mass of the hydrogen atom, and $A_{\mathrm{pixel}} = 1.6 \times 10^{-5}$ pc^2 is the spatial area subtended by each pixel at the distance of the cloud. In blue (red) outflow lobes we sum the total mass in each velocity channel blueward (redward) of v_{sys} and arrive at the outflow mass spectrum dM/dv. We only consider pixels above 3σ and within

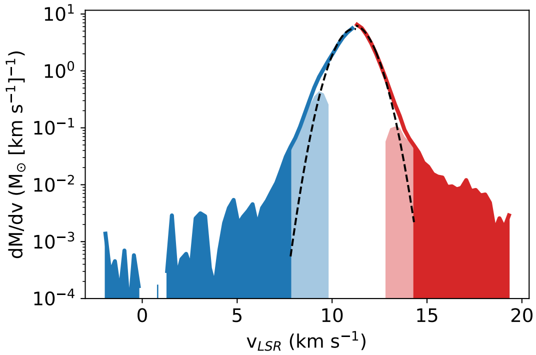

Figure 6: Mass spectrum of the HOPS 68 outflow. The blue (red) lines show the opacity-corrected mass spectrum in the blue (red) lobe region. The black dashed lines are gaussian fits to these mass spectra. The dark blue (dark red) shaded regions indicate the region integrated to get the high-velocity mass. The light blue (light red) shaded regions show the low-velocity mass after subtracting the cloud mass spectrum fit (see Section 4.1.5).

their respective outflow lobe region in this mass calculation. Figure 6 shows an example mass spectrum for the HOPS 68 outflow.

The total mass of each outflow lobe is obtained by integrating the mass spectrum over the relevant velocity range. For a lower limit on the mass, we consider only the high-velocity component: all velocity channels farther from $v_{\rm sys}$ than the minimum visually determined outflow velocity (Section 3). These velocities were chosen to include as much outflow emission as possible while avoiding contamination by the main cloud. However, if we only consider this high-velocity outflow material, we may miss a significant fraction of the total mass.

4.1.6. *Low-Velocity Outflow Emission*

Outflows are conspicuous because of their high-velocity emission. But outflows also exist at lower velocities. Dunham et al. (2014) note that escape velocities from protostars can be as low as 0.1 km s^{-1}. As these velocities are much lower than typical cloud CO linewidths, this low-velocity outflow material is often difficult to disentangle from the CO emission arising from the turbulent host molecular cloud.

The low-velocity contribution to the total outflow mass can be quite significant. Dunham et al. (2014) found that adding the inferred low-velocity emission increased the mass of outflows by a factor of 7.7 on average, with some outflows increasing by an order of magnitude or more. Outflow momentum and energy increased by factors of 3 to 5, on average. Offner et al. (2011) found that using only high-velocity outflow emission underestimated the total outflow mass by a factor of 5 in synthetic observations of simulated outflows. Clearly, low-velocity emission should be accounted for when assessing the absolute impact of outflows on the cloud. We describe our method, adapted from Dunham et al. (2014) for recovering this low-velocity outflow mass below.

For each outflow lobe, we fit the opacity-corrected mass spectrum with a Gaussian. For "low" velocities between $v_{\rm sys}$ and the visually determined minimum outflow velocity ($v_{\rm blue}$ or $v_{\rm red}$), we subtract this Gaussian fit from the mass spectrum and define any excess mass as low-velocity outflow mass. To reduce the amount of extraneous cloud mass introduced with this method, we exclude all velocity channels within 1 km s^{-1} of $v_{\rm sys}$. Figure 6 demonstrates this procedure for the HOPS 68 outflow.

Generally, the low-velocity outflow mass is significantly greater than the mass at high velocities. Because this method assumes the cloud mass spectrum is fit well by a Gaussian, we expect that the low-velocity mass will often be contaminated by ambient cloud material. Thus, for each outflow lobe, we consider the high-velocity outflow mass to be a lower limit and the high-velocity plus low-velocity mass to be an upper limit on the total outflow lobe mass. We report these mass ranges for each outflow lobe in Table 2.

4.1.7. *Momentum and Kinetic Energy*

We define the momentum per velocity channel to be $dP/dv = (dM/dv)v_{\rm out}$, where dM/dv is the mass spectrum discussed in Section 4.1.5 and $v_{\rm out}$ is the velocity relative to $v_{\rm sys}$. Similarly, the kinetic energy per velocity channel is $dE/dv = (1/2)(dM/dv)v_{\rm out}^2$. We sum the momentum and kinetic energy separately for low velocities, with the ambient cloud corrected mass spectrum, and high velocities. In Table 2, we report the momentum and kinetic energy of each outflow lobe.

4.1.8. *Dynamical Time*

We use the same method as Curtis et al. (2010) to estimate the dynamical time $t_{\rm dyn}$ of each outflow lobe. Assuming the outflow has been expanding uniformly at the same velocity since it was launched, $t_{\rm dyn} = R/v_{\rm max}$, where R is the length of the outflow and $v_{\rm max}$ is the maximum outflow velocity. We define R to be the projected distance from the outflow source to the farthest part of the outflow lobe and $v_{\rm max}$ as the minimum velocity relative to $v_{\rm sys}$ where ^{12}CO is not detected at 3σ. Some outflows are detectable all the way to the limits of the ^{12}CO spectral coverage (-2 km s^{-1} in the blue, 20 km s^{-1} in the red, relative to the LSR). In these

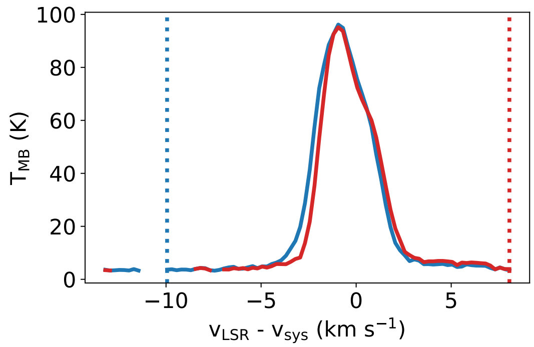

Figure 7: Maximum velocity of the HOPS 68 outflow. The blue (red) lines show the mean ^{12}CO spectrum in the blue (red) lobe regions. The blue (red) dotted line marks the maximum blue (red) outflow velocity, defined as the first channel where ^{12}CO is not detected at 3σ (see Section 4.1.8).

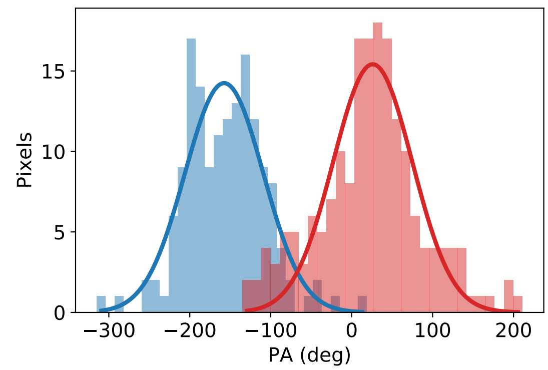

Figure 8: Position angle and opening angle of HOPS 68 outflow. The blue (red) histograms show the position angle distribution of all pixels in the blue (red) lobe region. The curves are gaussian fits to these distributions. We adopt the mean of each lobe as the position angle and the full-width at quarter maximum as the opening angle (see Section 4.1.9).

cases, $v_{\rm max}$ is a lower limit, as are the mass and mass-derived properties. Figure 7 shows our determination of $v_{\rm max}$ for the HOPS 68 outflow. We report R, $v_{\rm max}$, and $t_{\rm dyn}$, for each outflow lobe in Table 2.

We also calculate the mass loss rate, momentum injection rate, and energy injection rate by dividing the outflow mass, momentum, and kinetic energy by $t_{\rm dyn}$. In Section 4.2, we use these quantities to compare the impact of outflows on the cloud to the turbulent dissipation.

4.1.9. *Outflow Position Angle and Opening Angles*

Most studies estimate the outflow position angle (PA) by eye (e.g. Morgan et al. 1991; Takahashi et al. 2008; Plunkett et al. 2013; Stephens et al. 2017; Kong et al. 2019; Tanabe et al. 2019, submitted). We adopt a more reproducible and objective method to measure outflow position and opening angles (OA) suggested by M. Dunham (2019, private communication) and modeled after the simulated outflow analysis carried out by Offner et al. (2011).

For each outflow lobe, we make an initial guess of the PA, measured counterclockwise (east) from the north celestial pole by convention. This initial guess is the angle from the outflow source to the peak of the integrated ^{12}CO over the velocity range of the outflow lobe. Then, we calculate the angle of every pixel in the outflow lobe relative to this initial guess. We fit the distribution of these angles with a Gaussian and define the mean of the Gaussian to be the PA of that outflow lobe. We define the opening angle of the outflow to be the full-width at quarter maximum (FWQM) of the Gaussian, following the definition by Offner et al. (2011). We find this automated method does a suitable job producing a similar PA and OA to a visual determination. Furthermore, when comparing the outflow PA with with filament orientation (Section 5), we avoid the risk of an artificial correlation produced by unintentional measurement bias. Figure 8 shows the distribution of pixel position angles and Gaussian fit for the HOPS 68 outflow.

4.2. *Impact of Outflows on the Cloud*

Protostellar outflows may be important in the maintenance of turbulence in clouds, at least at cluster scales (Nakamura & Li 2007). The efficiency of turbulent driving by outflows is highly uncertain, depending on the transfer of momentum from outflowing gas to the cloud. To be even a plausible source of turbulence, the aggregate impact of outflows must be of a similar magnitude to the observed turbulent dissipation.

The total outflow momentum, kinetic energy, and their injection rates are given in the last row of Table 2. We report lower and upper limits on these aggregate values by summing each outflow's high-velocity component and high-velocity + low-velocity components, respectively (see Section 4.1.6).

We compare the aggregate outflow impact with the cloud turbulent statistics summarized in Table 9 of Tanabe et al. (2019, submitted). Using methods from Mac Low (1999), McKee & Ostriker (2007), and Li et al. (2015), they estimate the turbulent momentum dissipation rate ($\dot{P}_{\rm turb}$) and kinetic energy dissipation rate ($\dot{E}_{\rm turb}$). Excluding the OMC 1 region, they report $\dot{P}_{\rm turb} = 2.83 \times 10^{-2}\ M_\odot$ km s^{-1} yr^{-1} and $\dot{E}_{\rm turb} = 1.36 \times 10^{34}$ erg s^{-1}.

We compare these turbulent dissipation rates to the aggregate outflow injection rates in Table 2 $\dot{P}$ and $\dot{E}$. If we only account for the high-velocity outflow components, $\dot{P}$ is 7% of $\dot{P}_{\rm turb}$ and $\dot{E}$ is 19% of $\dot{E}_{\rm turb}$. If we add the low-velocity outflow emission, $\dot{P}$ is 25% of $\dot{P}_{\rm turb}$ and $\dot{E}$ is 51% of $\dot{E}_{\rm turb}$.

The outflow physical properties tabulated in Table 2 are not corrected for the inclination of outflows to the line-of-sight. Essentially, this means we assume that the radial velocity of outflow emission with respect to the source velocity is equivalent to the actual velocity of the outflowing gas. The closer an outflow is to the plane of the sky, the larger the discrepancy between observed and actual velocities. The outflow length $R_{\rm max}$, which we use to calculate $t_{\rm dyn}$ and all the derived injection rates, should also be corrected for the outflow inclination.

Because we do not know the actual inclination of each outflow, we estimate the effect of inclination on the aggregate outflow impact by assuming the same average inclination for every outflow. The average inclination angle, assuming any orientation is equally likely, is 57.3° (where 0° is a pole-on outflow). Dunham et al. (2014) summarize the inclination dependence of each outflow property in their Table 8. If all of the outflows are inclined 57.3°, the total $\dot{P}$ ($\dot{E}$) will increase by a factor of 2.9 (5.3). Thus, after correcting for average inclination, $\dot{P}$ is 20-72% of $\dot{P}_{\rm turb}$ and $\dot{E}$ is 103-281% of $\dot{E}_{\rm turb}$ (depending on whether low-velocity emission is included).

We note this inclination correction assumes that all outflow motions are along the axis of the flow, with no transverse motions. Dunham et al. (2014) caution that the inclination correction factors may be significantly smaller if transverse motions are present, as demonstrated by simulations from Downes & Cabrit (2007). The same simulations show that accounting for *atomic* gas results in additional momentum and energy of about the same magnitude as the inclination corrections discussed above. While the absolute impact of outflows in Orion A remains highly uncertain, it is safe to say a significant fraction of the turbulent dissipation could be offset if outflows couple efficiently to the cloud.

5. OUTFLOW-FILAMENT ALIGNMENT

Outflows are ejected along the angular momentum axis of the protostar. If mass accretion proceeds hierarchically, from larger scales of the cloud down to the protostellar scale, then the angular momentum axis of the protostar will trace the orientation of mass accretion flows (Bodenheimer 1995). Protostars tend to form along narrow filaments of dense gas (Arzoumanian et al. 2011), and may accrete mass either along (parallel to) or across (perpendicular to) their host filaments. If protostars predominately accrete mass along filaments, their outflows should be ejected perpendicular to the long axis of the filament. Conversely, if protostars accrete mostly across filaments, their outflows will be ejected parallel to the filament axis.

In simulations, Offner et al. (2016) find that turbulent fragmentation of protostellar cores produce outflows with variable position angles, and they predict a random distribution of outflow orientations under this turbulent fragmentation model. Li et al. (2018) find outflows form preferentially perpendicular to filaments in their simulations of a strongly magnetized cloud.

The alignment between CO outflows and filaments has been studied in Perseus by Stephens et al. (2017) and in a massive infrared dark cloud (IRDC, Kong et al. 2019). In Perseus, Stephens et al. (2017) showed that outflows are consistent with being randomly oriented with respect to the filament, neither parallel nor perpendicular. In the IRDC G28.37+0.07, Kong et al. (2019) showed that outflows are preferentially perpendicular to the filament axis. It remains to be seen whether this discrepancy arises from some meaningful difference between these clouds (e.g. evolutionary state or magnetic field strength) or by chance.

In Orion, Davis et al. (2009) showed that H_2 outflows appear randomly oriented on the sky, showing no preferential alignment to the North-South integral-shaped filament. Tanabe et al. (2019, submitted) studied the outflows in single-dish CO maps, finding no evidence for alignment between outflows and the large-scale filamentary structure in the cloud. However, the filamentary structure in Orion A is more complex than a single North-South integral-shaped filament. Therefore, we use the $C^{18}O$ filaments identified by Suri et al. (2019) in our analysis.

5.1. *$C^{18}O$ Filaments*

Suri et al. (2019) apply the Discrete Persistent Structures Extractor, DisPerSE (Sousbie 2011) to extract filaments from the $C^{18}O$ spectral cube. DisPerSE connects local maxima and saddle points in the intensity distribution, which are defined as filaments. Suri et al. (2019) identify a total of 625 filaments across the Orion A cloud, each of which are defined by their PPV coordinates, allowing filaments that overlap spatially to be separated in velocity space.

For each outflow source, we search for the closest filament. Because most of the outflow sources are located along lines of sight with a single significant $C^{18}O$ velocity component, we ignore the filament velocity information and only consider projected distance on the sky. We use cubic spline interpolation to approximate the

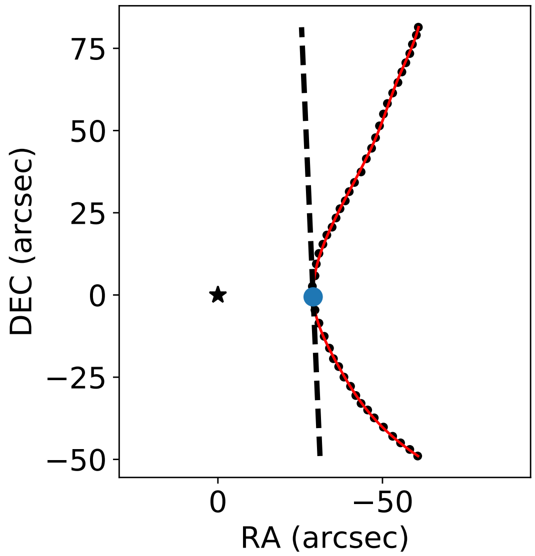

Figure 9: $C^{18}O$ filament near HOPS 68. The black dots show the filament closes to HOPS 68 from the Suri et al. (2019) catalog. The red curve is a smooth cubic spline interpolation of the filament. The outflow source (HOPS 68) is marked with a black star. The blue circle shows the closest point on the filament to the source. To derive the filament position angle, we find the tangent at this nearest point, shown as a black dashed line (see Section 5).

discrete filament coordinates with a smooth curve. For this spline interpolation, we used the splrep and splev functions from the scipy.interpolate package. After experimenting with the smoothing parameter s to find an optimal trade-off between smoothness and goodness-of-fit, we adopt $s = 0.1 \times d_{\rm min}$ where $d_{\rm min}$ is the minimum distance between the filament and outflow source.

We take the slope of the tangent to the filament curve at the closest point to the outflow source to be the position angle of the filament, which is constrained to be between −180 and 180°. Figure 9 shows an example of the spline interpolation and tangent fitting for the closest filament to the HOPS 68 outflow.

5.2. *Projected Angle Between Outflows and Filaments*

We follow Stephens et al. (2017) and Kong et al. (2019) in our definition of the angular separation between outflow and filament position angles, γ. For each outflow lobe, we define γ to be

$$\gamma = \mathrm{MIN}\{|\mathrm{PA_{out}} - \mathrm{PA_{fil}}|, 180^\circ - |\mathrm{PA_{out}} - \mathrm{PA_{fil}}|\}, \quad (5)$$

where $\mathrm{PA_{out}}$ and $\mathrm{PA_{fil}}$ are the position angles of the outflow lobe and the closest filament, respectively. The value of γ for each outflow lobe is given in Table 3.

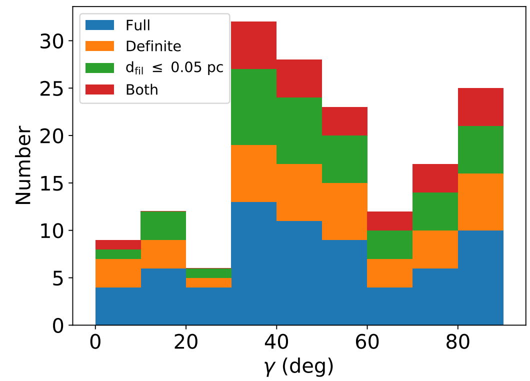

Figure 10: Distribution of projected angle between outflows and filaments. The blue histogram shows the distribution of γ in 10° bins for the full sample of 67 outflow lobes. The orange bars show the distribution of γ for the subsample of 38 outflow lobes with a confidence grade of "Definite" (Table 1). The green bars show the subsample of 37 outflow lobes whose sources are within 0.05 pc of the nearest filament (Table 3). The red bars show the subsample of 22 outflow lobes which satisfy both of these conditions. Note that the total height of the stacked bars does not equal the size of the full sample, since the subsamples are already contained within the full sample shown in blue.

Figure 10 shows the distribution of γ. The full sample of γ shows no obvious clustering at either 0 or 90°.

Many of the outflows in our catalog are not as clear as our example outflow driven by HOPS 68. Outflows categorized as "Marginal" in Table 1 are likely to have less reliable position angles. In these cases, we either have difficulty disentangling the high-velocity emission near these sources and/or we are unsure of which protostar is driving the outflow. Both of these factors could greatly affect the measured position angle and, by extension, γ. Stephens et al. (2017) argue that the incorrect assignment of driving sources led Anathpindika & Whitworth (2008) to erroneously conclude that outflows and filaments are perpendicular in the Perseus molecular cloud.

To test whether more reliable outflows have a different distribution of γ, we consider a subsample of outflow lobes which we consider "Definite" (Table 1). Figure 10 shows that these outflows are not distributed significantly differently from the full sample.

Aside from the uncertainties in calculating the outflow position angles discussed above, we consider the difficulty of assigning even a well-known outflow to a particular filament. Even though we select for the closest filament to each outflow source, we cannot exclude the possibility that other nearby filaments may be important to the environment of an outflow. In particular, the OMC-4 region contains spatially overlapping filaments which are distinct in velocity space (Suri et al. 2019) similar to the fibers identified by Hacar et al. (2013). The incorrect assignment of outflows to filaments may introduce noise to the distribution of γ and mask an underlying correlation between outflow and filament orientations. To address this concern, we compare the full sample to the closest outflow-filament pairs. We adopt a threshold on the projected outflow-filament distance ($d_{\rm fil}$) based on the typical filament width.

Suri et al. (2019) found an average filament FWHM of approximately 0.1 pc, similar to the "characteristic" filament width found using *Herschel* dust continuum maps (e.g. Arzoumanian et al. 2011; Koch & Rosolowsky 2015) However, Suri et al. (2019) find a much larger spread in filament widths (about an order of magnitude around the mean). This is likely due to the fact that they allow the filament width to vary along its length, while most studies average the width over the entire filament. Motivated by the mean filament width, we choose a threshold of $d_{\rm fil} \leq 0.05$ pc, which corresponds to an outflow source within the FWHM of an average filament. Figure 10 shows the distribution of γ for this subset of outflows.

Figure 10 shows that limiting the sample to the closest outflow-filament pairs with the highest confidence reduces the fraction of outflows at projected angles of 0-30° with respect to their filaments. We stress that these angles are projected on the plane of the sky. To determine whether these outflows are preferentially aligned with the filaments, we must consider the underlying distribution of deprojected γ: the outflow-filament alignment in 3D.

5.3. *3D Outflow-Filament Alignment*

An outflow-filament pair can appear at various relative orientations on the plane of the sky, depending on the line-of-sight. For example, an outflow observed perpendicular to a nearby filament may actually be parallel in space. Thus, we follow Stephens et al. (2017) and Kong et al. (2019) and run Monte Carlo simulations[2] of random vector pairs to project different underlying distributions of $\gamma_{\rm 3D}$ onto the plane of the sky.

We fist generate 10^7 pairs of unit vectors uniformly distributed around the unit sphere. From this random uniform distribution, we draw two samples. In the parallel sample, we keep only those vector pairs separated by 0-20°. In the perpendicular sample, we keep the pairs separated by 70-90°. Then, we project these vectors onto the plane of the sky by setting one coordinate to 0 and calculate the projected angle between them, γ. By comparing the distribution of the observed γ with the random, parallel, and perpendicular models, we investigate which of these underlying scenarios is most likely given the observations.

Figure 11 shows the cumulative distribution of γ for the Monte Carlo simulations and each of the outflow-filament samples discussed in Section 5.2. Compared to the random distribution of γ, the outflow samples have a deficit of $\gamma < 40°$. In particular, the "Both" subsample with the 22 definite outflow lobes closest to their filaments contains only one lobe with $\gamma < 33°$ (the blue lobe of the SMZ 17 outflow) compared to the ~ 8 which would be expected if γ were distributed randomly.

While Figure 11 shows that the "Parallel" scenario is clearly inconsistent with the observed distribution of γ, the "Perpendicular" distribution is more difficult to rule out. We apply the Anderson-Darling (AD) test (Stephens 1974) to determine if the perpendicular or random distributions can be rejected for each outflow subsample. The AD p-values listed in Table 4 represent the likelihood that the observed outflow-filament γ distribution is drawn from either the random or perpendicular distribution. We do not report the results of AD tests for the parallel case; the p-values for the parallel distribution are all close to zero.

Based on the AD test, we reject the hypothesis that the full outflow sample is drawn from a perpendicular distribution with $> 99.9\%$ confidence ($p < 0.001$), while the random distribution is not ruled out. For the definite subsample the results are similar, though we can only rule out the perpendicular distribution with 94% confidence ($p = 0.06$). For the $d_{\rm fil} \leq 0.05$ pc subsample, we can rule out the perpendicular distribution with 98% confidence ($p = 0.02$). Though these subsamples are unlikely to be drawn from a purely perpendicular distribution, their p-values are higher than the equivalent in Stephens et al. (2017). We do not test models with a mixture of perpendicular and parallel outflow-filament alignment, but such a bimodal distribution may be a better fit to our data than either random or perpendicular model alone.

If we limit the sample to the definite outflows with $d_{\rm fil} \leq 0.05$ pc ("Both"), and compare to the perpendicular model, we calculate an AD p-value of > 0.25. While we cannot rule out with better than 94% confidence ($p = 0.06$) that this subsample of outflows is drawn from a random distribution, the perpendicular model more closely matches the angular distribution of these close outflow-filament pairs. We tentatively con-

[2] See Appendix A of Stephens et al. (2017) for a detailed description of the Monte Carlo simulations.

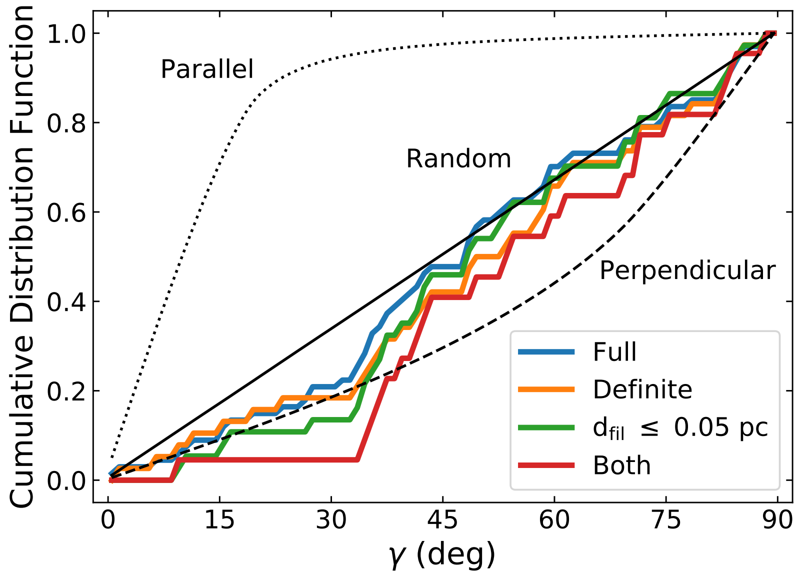

Figure 11: Cumulative distribution of projected angle between outflows and filaments. The colored lines show the distribution of γ for different subsets of our outflow catalog. The black lines show the expected distribution given three different model distributions. The parallel case contains only 3D angles between 0 and 20°, the random case contains all 3D angles between 0 and 90°, and the perpendicular case contains 3D angles between 70 and 90°. The results of Anderson-Darling tests between the observed and modeled distributions are in Table 4 (see Section 5.2).

clude that the clearest outflow-filament pairs in Orion A are perpendicularly aligned.

In Perseus, Stephens et al. (2017) found a random distribution of outflow-filament angles. This random alignment could reflect processes at large or small scales. At large scales, the orientation of filaments may not determine the accretion of mass onto them, contradicting simulations of filament formation (e.g. Chen & Ostriker 2014; Clarke et al. 2017). At core scales, no matter the orientation of mass accretion, perhaps the protostellar angular momentum may be randomized by multiplicity or turbulence, as seen in simulations by Offner et al. (2016) and Lee et al. (2017). Therefore, our finding of moderate perpendicular alignment between outflows and filaments in Orion A may mean that filament formation or protostellar mass accretion is different in these two GMCs.

In the IRDC G28, Kong et al. (2019) found a remarkably perpendicular outflow-filament alignment, rejecting a random distribution at high confidence (see Table 4). Such a strong perpendicular alignment is predicted in simulations of IRDCs by Li et al. (2018) and Li & Klein (2019) resulting from filament formation perpendicular to a strong magnetic field and continuous mass accretion along the magnetic field lines onto protostellar cores. As IRDCs are generally considered to be in the earliest phase of massive star formation (Rathborne et al. 2006), the outflow-filament alignment may evolve with evolutionary stage. A comprehensive study of γ across many different star forming environments is necessary to answer this question.

While we find some evidence for perpendicular outflow-filament alignment in Orion A, previous studies have concluded that outflows and filaments in this cloud are randomly aligned. Davis et al. (2009) show that the position angles of H_2 jets in Orion A are distributed uniformly and oriented randomly with respect to the ∼pc-scale integral shaped filament. Tanabe et al. (2019, submitted) conclude the same using their CO outflow catalog. Our study is not directly comparable to these, as we use the C^18O filaments, which reveal the integral-shaped filament to be made up of many smaller filamentary structures.

6. CONCLUSIONS

We have identified 45 outflows in the CARMA-NRO Orion CO maps of Orion A. Eleven of these outflows are new detections. For the previously known outflows, we improve the earlier estimates of their mass by including a correction for low-velocity mass as well as a velocity-dependent opacity correction. Most of the outflows have HOPS protostars associated with them, and many are correlated with H_2 flows. The outflows contain significant momentum and kinetic energy compared to estimates for the turbulent dissipation in Orion A. If outflows couple efficiently to the cloud, they can maintain cloud turbulence and slow star-formation. There is still considerable uncertainty in the outflow impact and a mechanism for transporting momentum from the outflow length scale to the larger cloud is needed (see Offner & Liu 2018 for an option).

We compare the outflow position angles to the orientation of nearby filaments from the $C^{18}O$ catalog of Suri et al. (2019). The full outflow catalog is consistent with random outflow-filament alignment. The most reliable outflows which are closest to their filaments show a moderately perpendicular outflow-filament alignment and a random distribution is ruled out with high confidence.

While we improve the specificity of the outflow-filament comparison compared to previous studies of Orion A by using the $C^{18}O$ filament catalog, there is still uncertainty in pairing outflows and filaments. Future work should investigate the outflow-filament alignment over multiple length scales, and take into account the varying filament width.

The outflow-filament alignment may change as protostars evolve. A detailed comparison should be made between this alignment and protostellar properties such as bolometric temperature, multiplicity, and evolutionary stage. A combination of this sample with the studies in other clouds could provide enough statistical power to answer these more specific questions about outflow-filament alignment and the mass assembly of protostars.

Table 1. Outflow Catalog.

Source[a]	R.A. (J2000)	Decl. (J2000)	$v_{\rm blue}/v_{\rm red}$ [b] (km s^{-1})	Confidence	Tanabe
SMZ 11	$5^h35^m23.30^s$	$-5°07'10.00''$	7.5/-	M/-	9
SMZ 17	$5^h35^m27.00^s$	$-5°09'54.00''$	3/18	D/D	
SMZ 21	$5^h35^m26.90^s$	$-5°11'07.00''$	-/14	-/M	15
SMZ 30	$5^h35^m18.30^s$	$-5°31'42.00''$	4.5/-	M/-	20
SMZ 50	$5^h36^m11.50^s$	$-6°22'22.00''$	4.5/-	M/-	33
HOPS 10	$5^h35^m09.00^s$	$-5°58'27.48''$	-/12.6	-/D	27
HOPS 11	$5^h35^m13.42^s$	$-5°57'57.96''$	4.7/12.8	D/D	26
HOPS 12	$5^h35^m08.59^s$	$-5°55'54.12''$	4.7/-	D/-	25
HOPS 44	$5^h35^m10.58^s$	$-5°35'06.36''$	4.4/-	M/-	
HOPS 50	$5^h34^m40.90^s$	$-5°31'44.40''$	5.8/-	M/-	21
HOPS 56	$5^h35^m19.46^s$	$-5°15'32.76''$	-/14	-/M	19
HOPS 58	$5^h35^m18.50^s$	$-5°13'38.28''$	-/14	-/M	
HOPS 59	$5^h35^m20.14^s$	$-5°13'15.60''$	6.9/-	M/-	17
HOPS 60	$5^h35^m23.33^s$	$-5°12'03.24''$	7.0/14.2	D/D	16
HOPS 68	$5^h35^m24.31^s$	$-5°08'30.48''$	7.8/14.5	D/D	12
HOPS 70	$5^h35^m22.42^s$	$-5°08'04.92''$	-/14	-/M	11
HOPS 71	$5^h35^m25.61^s$	$-5°07'57.36''$	7.5/-	D/-	10
HOPS 75	$5^h35^m26.66^s$	$-5°06'10.44''$	-/14.3	-/M	8
HOPS 78	$5^h35^m25.82^s$	$-5°05'43.80''$	6/15	D/D	7
HOPS 81	$5^h35^m27.96^s$	$-5°04'58.08''$	7.5/13.5	M/M	
HOPS 84	$5^h35^m26.57^s$	$-5°03'55.08''$	8.5/13.8	D/D	6
HOPS 87	$5^h35^m23.47^s$	$-5°01'28.56''$	8.6/13.8	M/M	5
HOPS 88	$5^h35^m22.44^s$	$-5°01'14.16''$	8.1/13.8	D/D	4
HOPS 92	$5^h35^m18.31^s$	$-5°00'33.12''$	7.6/13.7	D/D	3
HOPS 96	$5^h35^m29.71^s$	$-4°58'48.72''$	9.8/13.9	D/D	1
HOPS 99	$5^h34^m29.50^s$	$-4°55'30.72''$	8.3/-	M/-	

Table 1 *continued*

Table 1 *(continued)*

Source[a]	R.A. (J2000)	Decl. (J2000)	$v_{\rm blue}/v_{\rm red}$[b] (km s^{-1})	Confidence	Tanabe
HOPS 157	$5^{h}37^{m}56.57^{s}$	$-6°56'39.12''$	3.5/-	M/-	
HOPS 158	$5^{h}37^{m}24.46^{s}$	$-6°58'32.88''$	5/9.5	M/M	
HOPS 160	$5^{h}37^{m}51.05^{s}$	$-6°47'20.40''$	4.7/-	D/-	
HOPS 166	$5^{h}36^{m}25.13^{s}$	$-6°44'41.64''$	5.5/11.5	M/D	40
HOPS 168	$5^{h}36^{m}18.94^{s}$	$-6°45'22.68''$	4.9/12.1	D/D	41
HOPS 169	$5^{h}36^{m}36.12^{s}$	$-6°38'51.72''$	4.7/10	D/D	39
HOPS 174	$5^{h}36^{m}25.85^{s}$	$-6°24'58.68''$	4/-	M/-	36
HOPS 177	$5^{h}35^{m}50.02^{s}$	$-6°34'53.40''$	-/10.3	-/D	37
HOPS 178	$5^{h}36^{m}24.60^{s}$	$-6°22'41.16''$	4.3/-	D/-	34
HOPS 179	$5^{h}36^{m}21.84^{s}$	$-6°23'29.76''$	4.5/11.9	D/M	35
HOPS 181	$5^{h}36^{m}19.51^{s}$	$-6°22'12.36''$	4/12	D/D	32
HOPS 182	$5^{h}36^{m}18.84^{s}$	$-6°22'10.20''$	4/11.7	D/D	31
HOPS 192	$5^{h}36^{m}32.45^{s}$	$-6°01'16.32''$	7.5/10	M/M	
HOPS 198	$5^{h}35^{m}22.18^{s}$	$-6°13'06.24''$	-/10	-/M	
HOPS 203	$5^{h}36^{m}22.85^{s}$	$-6°46'06.24''$	-/11.7	-/D	42
HOPS 355	$5^{h}37^{m}17.09^{s}$	$-6°49'49.44''$	4.3/10.5	M/M	
HOPS 368	$5^{h}35^{m}24.72^{s}$	$-5°10'30.36''$	7/14	D/D	14
HOPS 370	$5^{h}35^{m}27.62^{s}$	$-5°09'33.48''$	5/17	M/M	13
HOPS 383	$5^{h}35^{m}29.81^{s}$	$-4°59'51.00''$	9.6/-	D/-	2

[a] HOPS sources are protostars in the catalog from Furlan et al. (2016). SMZ sources are sources of H_2 outflows in Davis et al. (2009) which are not in the HOPS catalog.

[b] These are the visually determined velocities at which the outflow lobes are most prominent. Entries marked with '-' indicate that one of the outflow lobes is not detected. See Section 3 for details.

[c] Each entry has two values, referring to the blue/red lobes separately. Entries marked 'D' for Definite, are clearly outflows. Entries marked 'M' for Marginal are unclear. See Section 3 for details.

Table 2. Outflow Physical Properties

Source	Lobe	M[a] ($M_\odot$)	P ($M_\odot$ km s^{-1})	E (10^{43} erg)	$R_{\rm max}$ (pc)	$v_{\rm max}$ (km s^{-1})	$t_{\rm dyn}$ (10^4 yr)	$\dot{M}$ (10^{-6} $M_\odot$ yr^{-1})	$\dot{P}$ (10^{-6} $M_\odot$ km s^{-1} yr^{-1})	$\dot{E}$ (10^{30} erg s^{-1})
SMZ 11	B	0.10 - 1.63	0.47 - 3.94	2.3 - 10.6	0.11	7.1	1.5	6.5 - 105.9	30.8 - 255.9	47.0 - 219.0
SMZ 17	B	0.00 - 0.17	0.01 - 0.52	0.1 - 1.9	0.03	9.0	0.3	0.2 - 50.2	2.2 - 150.2	6.2 - 178.2
-	R	0.01 - 0.24	0.05 - 0.71	0.4 - 2.6	0.05	8.3	0.6	1.2 - 40.9	8.8 - 121.8	20.8 - 140.8
SMZ 21	R	0.11 - 1.33	0.36 - 2.63	1.2 - 5.7	0.29	5.1	5.5	1.9 - 24.1	6.5 - 47.6	7.0 - 32.8
SMZ 30	B	0.65 - 0.99	1.15 - 1.56	2.0 - 2.5	0.16	2.6	6.1	10.7 - 16.3	18.8 - 25.6	10.6 - 13.2
SMZ 50	B	0.08 - 0.23	0.23 - 0.50	0.7 - 1.2	0.22	4.8	4.6	1.8 - 5.0	5.1 - 11.0	4.6 - 8.2
HOPS 10	R	0.08 - 1.57	0.44 - 4.90	2.7 - 16.6	0.27	11.2	2.3	3.3 - 66.9	19.0 - 209.0	36.4 - 224.4
HOPS 11	B	0.13 - 0.19	0.53 - 0.63	2.2 - 2.4	0.14	9.7	1.4	9.5 - 13.2	37.6 - 44.9	50.0 - 54.8

Table 2 *continued*

Table 2 *(continued)*

Source	Lobe	M^a	P	E	$R_{\max}$	$v_{\max}$	$t_{\rm dyn}$	$\dot{M}$	$\dot{P}$	$\dot{E}$
		($M_\odot$)	($M_\odot$ km s^{-1})	(10^{43} erg)	(pc)	(km s^{-1})	(10^4 yr)	(10^{-6} $M_\odot$ yr^{-1})	(10^{-6} $M_\odot$ km s^{-1} yr^{-1})	(10^{30} erg s^{-1})
-	R	0.06 - 1.23	0.42 - 3.82	3.0 - 13.5	0.18	11.6	1.6	3.9 - 78.6	26.7 - 244.8	60.9 - 273.9
HOPS 12	B	2.11 - 3.13	8.78 - 10.22	37.6 - 40.1	0.67	10.0	6.6	32.2 - 47.6	134.0 - 156.0	181.0 - 193.1
HOPS 44	B	1.42 - 2.84	5.43 - 9.63	20.9 - 33.4	0.18	9.8	1.8	77.5 - 155.1	296.6 - 526.5	362.0 - 579.0
HOPS 50	B	0.13 - 0.13	0.24 - 0.24	0.5 - 0.5	0.29	5.4	5.2	2.6 - 2.6	4.6 - 4.6	2.9 - 2.9
HOPS 56	R	0.22 - 1.57	0.89 - 3.82	3.7 - 10.4	0.15	7.7	1.9	11.3 - 82.0	46.4 - 199.4	61.7 - 172.7
HOPS 58	R	0.09 - 1.15	0.35 - 2.81	1.4 - 7.3	0.14	6.1	2.3	3.9 - 49.8	15.2 - 121.2	19.3 - 100.6
HOPS 59	B	0.09 - 2.27	0.44 - 4.23	2.2 - 9.3	0.53	8.6	6.0	1.6 - 37.7	7.3 - 70.1	11.5 - 48.9
HOPS 60	B	0.02 - 0.37	0.07 - 0.86	0.3 - 2.2	0.14	6.7	2.1	0.7 - 17.6	3.4 - 40.7	5.2 - 33.2
-	R	0.02 - 0.47	0.06 - 0.79	0.3 - 1.5	0.15	7.8	1.9	0.8 - 24.4	3.3 - 41.1	4.5 - 25.1
HOPS 68	B	0.03 - 0.55	0.16 - 1.25	1.0 - 3.4	0.05	9.9	0.5	6.1 - 109.1	32.1 - 250.4	61.8 - 214.8
-	R	0.05 - 0.19	0.25 - 0.55	1.3 - 2.0	0.06	8.1	0.7	7.9 - 27.5	37.2 - 81.1	59.3 - 91.5
HOPS 70	R	0.13 - 0.39	0.45 - 1.06	1.6 - 3.0	0.10	5.6	1.8	7.2 - 21.6	24.9 - 58.6	27.4 - 52.7
HOPS 71	B	0.19 - 3.95	0.83 - 8.19	3.8 - 19.7	0.35	6.8	5.0	3.7 - 78.4	16.5 - 162.5	23.7 - 123.6
HOPS 75	R	0.03 - 0.27	0.10 - 0.53	0.3 - 1.1	0.08	4.6	1.6	2.0 - 16.5	6.4 - 32.2	6.6 - 21.9
HOPS 78	B	0.34 - 8.42	2.30 - 23.47	16.1 - 76.6	0.41	13.3	3.0	11.2 - 278.3	76.0 - 775.6	168.0 - 802.0
-	R	0.19 - 3.69	0.85 - 7.55	4.0 - 17.9	0.34	8.0	4.2	4.5 - 87.2	20.1 - 178.1	29.6 - 134.6
HOPS 81	B	0.08 - 1.08	0.38 - 2.51	2.0 - 6.9	0.17	10.1	1.7	4.6 - 64.9	23.0 - 151.0	38.6 - 132.5
-	R	0.02 - 0.09	0.05 - 0.16	0.1 - 0.3	0.05	3.2	1.6	1.2 - 5.7	2.9 - 9.9	2.3 - 5.7
HOPS 84	B	0.02 - 0.13	0.05 - 0.20	0.1 - 0.4	0.13	4.4	2.8	0.7 - 4.5	1.8 - 7.3	1.6 - 4.2
-	R	0.86 - 2.81	3.01 - 7.74	10.6 - 22.3	0.86	8.7	9.7	8.8 - 28.9	30.9 - 79.6	34.6 - 72.6
HOPS 87	B	1.14 - 2.24	3.69 - 6.03	12.4 - 17.4	0.26	7.2	3.6	31.8 - 62.4	103.0 - 168.4	110.0 - 154.6
-	R	0.02 - 0.29	0.06 - 0.48	0.2 - 0.9	0.08	4.6	1.8	1.2 - 16.2	3.4 - 26.6	3.1 - 15.1
HOPS 88	B	0.18 - 1.09	0.75 - 2.63	3.3 - 7.3	0.09	9.1	0.9	19.5 - 115.2	78.7 - 277.7	109.0 - 245.0
-	R	0.05 - 0.11	0.16 - 0.28	0.5 - 0.8	0.08	6.9	1.1	4.5 - 10.0	14.2 - 24.8	14.9 - 21.6
HOPS 92	B	0.40 - 2.61	1.61 - 6.11	6.8 - 16.5	0.33	8.8	3.7	10.9 - 71.5	44.2 - 167.2	59.4 - 142.9
-	R	0.13 - 0.19	0.44 - 0.51	1.5 - 1.6	0.50	6.2	7.9	1.7 - 2.4	5.6 - 6.4	6.0 - 6.3
HOPS 96	B	0.04 - 0.09	0.11 - 0.17	0.3 - 0.4	0.11	4.0	2.6	1.6 - 3.5	4.2 - 6.4	3.9 - 4.6
-	R	0.35 - 1.65	0.73 - 2.61	1.6 - 4.3	0.23	4.7	4.8	7.2 - 34.1	15.1 - 53.9	10.1 - 28.0
HOPS 99	B	0.04 - 0.07	0.07 - 0.10	0.1 - 0.2	0.13	2.6	4.9	0.7 - 1.4	1.3 - 2.1	0.8 - 1.1
HOPS 157	B	0.03 - 0.03	0.08 - 0.08	0.2 - 0.2	0.10	3.4	3.0	1.1 - 1.1	2.6 - 2.6	2.1 - 2.1
HOPS 158	B	0.08 - 0.18	0.22 - 0.39	0.6 - 0.9	0.12	4.1	2.7	3.0 - 6.6	7.9 - 14.4	6.7 - 10.4
-	R	0.03 - 0.04	0.07 - 0.08	0.2 - 0.2	0.08	3.9	1.9	1.4 - 1.9	3.8 - 4.3	3.7 - 3.9
HOPS 160	B	0.07 - 0.07	0.10 - 0.10	0.2 - 0.2	0.11	3.2	3.4	2.0 - 2.0	3.0 - 3.0	1.6 - 1.6
HOPS 166	B	0.03 - 0.50	0.10 - 1.10	0.4 - 2.6	0.07	5.8	1.1	2.4 - 45.1	8.8 - 99.2	10.4 - 73.2
-	R	1.00 - 2.83	3.70 - 7.77	14.6 - 23.8	0.42	10.7	3.9	25.6 - 73.0	95.4 - 200.4	120.0 - 194.7
HOPS 168	B	0.01 - 0.05	0.03 - 0.11	0.2 - 0.3	0.09	6.1	1.5	0.5 - 3.5	2.1 - 7.5	3.4 - 6.5
-	R	1.03 - 7.47	4.61 - 16.30	22.4 - 45.7	1.20	10.4	11.3	9.1 - 66.0	40.7 - 143.7	62.8 - 128.1
HOPS 169	B	0.10 - 0.24	0.49 - 0.71	2.8 - 3.1	0.25	8.9	2.7	3.5 - 8.8	17.9 - 25.7	32.0 - 35.8
-	R	0.14 - 1.18	0.79 - 2.50	5.1 - 8.1	0.23	12.3	1.8	7.7 - 64.2	43.0 - 135.3	88.3 - 139.7
HOPS 174	B	0.07 - 0.16	0.22 - 0.39	0.7 - 1.0	0.21	4.4	4.6	1.6 - 3.4	4.7 - 8.6	4.5 - 7.2
HOPS 177	R	0.77 - 1.06	1.52 - 1.87	3.2 - 3.6	0.31	7.3	4.2	18.5 - 25.5	36.3 - 44.7	24.5 - 27.7
HOPS 178	B	0.19 - 0.55	0.62 - 1.42	2.0 - 3.8	0.21	8.9	2.4	8.2 - 23.4	26.3 - 60.1	27.2 - 51.3
HOPS 179	B	0.06 - 0.06	0.16 - 0.16	0.4 - 0.4	0.09	4.6	1.8	3.3 - 3.3	8.7 - 8.7	7.4 - 7.4
-	R	0.04 - 0.90	0.24 - 3.13	1.6 - 11.8	0.12	12.4	1.0	4.0 - 93.7	25.1 - 326.9	51.2 - 391.2
HOPS 181	B	0.51 - 0.98	2.08 - 3.39	8.9 - 12.6	0.21	9.1	2.3	22.1 - 42.3	90.2 - 147.2	122.0 - 173.0
-	R	0.26 - 10.68	1.57 - 26.51	9.7 - 77.1	1.18	12.1	9.5	2.8 - 111.8	16.4 - 277.8	32.3 - 256.3

Table 2 *continued*

Table 2 *(continued)*

Source	Lobe	M^a	P	E	$R_{\rm max}$	$v_{\rm max}$	$t_{\rm dyn}$	$\dot{M}$	$\dot{P}$	$\dot{E}$
		($M_\odot$)	($M_\odot$ km s^{-1})	(10^{43} erg)	(pc)	(km s^{-1})	(10^4 yr)	(10^{-6} $M_\odot$ yr^{-1})	(10^{-6} $M_\odot$ km s^{-1} yr^{-1})	(10^{30} erg s^{-1})
HOPS 182	B	0.31 - 0.55	1.34 - 2.01	6.1 - 8.0	0.22	9.1	2.4	13.3 - 23.5	57.0 - 85.4	82.1 - 107.2
-	R	0.11 - 1.35	0.66 - 4.52	4.1 - 16.5	0.55	11.1	4.8	2.3 - 28.2	13.8 - 94.0	27.1 - 109.0
HOPS 192	B	0.78 - 0.78	0.98 - 0.98	1.4 - 1.4	0.10	4.1	2.5	31.2 - 31.2	39.3 - 39.3	18.2 - 18.2
-	R	0.03 - 0.08	0.05 - 0.14	0.1 - 0.2	0.07	3.7	1.8	1.4 - 4.8	3.0 - 7.8	2.2 - 4.4
HOPS 198	R	0.01 - 0.20	0.03 - 0.51	0.1 - 1.4	0.11	6.0	1.8	0.3 - 11.6	1.5 - 28.9	2.2 - 25.9
HOPS 203	R	0.45 - 0.45	0.98 - 0.98	2.3 - 2.3	0.20	5.7	3.4	13.0 - 13.0	28.6 - 28.6	21.0 - 21.0
HOPS 355	B	0.40 - 0.47	1.40 - 1.48	5.0 - 5.1	0.45	8.9	4.9	8.2 - 9.6	28.6 - 30.2	32.7 - 33.3
-	R	0.03 - 0.21	0.13 - 0.55	0.5 - 1.5	0.49	7.8	6.2	0.5 - 3.5	2.1 - 8.8	2.8 - 7.7
HOPS 368	B	0.03 - 0.54	0.13 - 1.37	0.6 - 3.8	0.06	6.7	0.9	3.1 - 62.0	14.4 - 158.4	21.8 - 139.8
-	R	0.02 - 0.05	0.09 - 0.16	0.4 - 0.5	0.04	6.3	0.6	3.8 - 8.3	14.2 - 24.9	17.6 - 25.7
HOPS 370	B	0.05 - 0.35	0.40 - 1.40	3.5 - 7.2	0.14	13.1	1.0	4.7 - 34.3	39.5 - 136.5	109.0 - 222.0
-	R	0.02 - 0.60	0.11 - 1.35	0.8 - 3.9	0.13	8.1	1.5	1.1 - 39.2	7.5 - 88.7	16.0 - 80.4
HOPS 383	B	0.29 - 0.37	0.74 - 0.88	2.0 - 2.2	0.16	5.4	2.8	10.2 - 12.9	25.9 - 30.7	22.0 - 24.8
Total[b]		16.5 - 82.4	59.6 - 206.3	249 - 614				516 - 2710	1920 - 7063	2640 - 6900

[a] Mass and all properties derived from mass are given as lower and upper limits. The lower limit refers to the high-velocity component of the outflow only. The upper limit refers to the sum of the high-velocity and low-velocity components. See Section 4.1.5 for details.

[b] The total of the lower-limits and upper-limits for each column are given. The physical properties in this table are not corrected for inclination angle. See Section 4.2 for a discussion of the inclination correction.

Table 3. Outflow Angles and Filament Comparison.

Source	Position Angle[a]	Opening Angle	γ^b	$d_{\rm fil}{}^c$
	(°)	(°)	(°)	(pc)
SMZ 11	-35 ± 3.1/-	157 ± 10/-	27/-	0.066
SMZ 17	$-118 \pm 11/34 \pm 3.1$	$193 \pm 38/79 \pm 10$	10/38	0.01
SMZ 21	-/179 ± 0.5	-/35 ± 2	-/43	0.016
SMZ 30	20 ± 20/-	120 ± 120/-	35/-	0.11
SMZ 50	2 ± 1.4/-	77 ± 8.8/-	36/-	0.19
HOPS 10	-/19 ± 2	-/58 ± 6.8	-/71	0.003
HOPS 11	$172 \pm 1.2/16 \pm 1.7$	$92 \pm 4.1/68 \pm 5.6$	62/86	0.052
HOPS 12	-11 ± 0.1/-	39 ± 0.4/-	54/-	0.032
HOPS 44	-24 ± 2.4/-	120 ± 8.9/-	70/-	0.013
HOPS 50	-15 ± 0.4/-	42 ± 1.3/-	16/-	0.005
HOPS 56	-/119 ± 6	-/191 ± 23	-/33	0.048
HOPS 58	-/74 ± 0.6	-/44 ± 1.9	-/88	0.058
HOPS 59	-26 ± 0.2/-	15 ± 0.7/-	38/-	0.054
HOPS 60	$-104 \pm 0.3/57 \pm 0.3$	$22 \pm 1.1/24 \pm 0.9$	78/83	0.057
HOPS 68	$-158 \pm 3.8/26 \pm 3.7$	$161 \pm 13/163 \pm 12$	20/24	0.058
HOPS 70	-/48 ± 2	-/83 ± 7.5	-/74	0.015
HOPS 71	39 ± 0.6/-	35 ± 2.3/-	59/-	0.11

Table 3 *continued*

Table 3 *(continued)*

Source	Position Angle[a]	Opening Angle	γ[b]	$d_{\rm fil}$[c]
	(°)	(°)	(°)	(pc)
HOPS 75	-/175 ± 1.6	-/95 ± 5.5	-/17	0.003
HOPS 78	$-85 \pm 0.5/80 \pm 0.2$	$41 \pm 1.5/37 \pm 0.8$	59/43	0.046
HOPS 81	$-154 \pm 0.6/34 \pm 3.1$	$51 \pm 2/83 \pm 12$	40/32	0.067
HOPS 84	$78 \pm 0.7/-93 \pm 0.2$	$38 \pm 2.4/18 \pm 0.6$	58/49	0.056
HOPS 87	$-100 \pm 0.3/118 \pm 1.2$	$49 \pm 1.2/47 \pm 4.5$	27/11	0.008
HOPS 88	$-100 \pm 3.5/82 \pm 1.7$	$210 \pm 12/99 \pm 6.1$	36/35	0.023
HOPS 92	$89 \pm 0.3/-89 \pm 0.2$	$33 \pm 1.2/24 \pm 0.4$	43/41	0.019
HOPS 96	$69 \pm 0.8/-95 \pm 5$	$46 \pm 2.8/142 \pm 19$	55/71	0.007
HOPS 99	-49 ± 1.3/-	64 ± 4.8/-	48/-	0.003
HOPS 157	112 ± 1.4/-	66 ± 4.8/-	84/-	1.5
HOPS 158	$66 \pm 1.4/-114 \pm 2.7$	$84 \pm 4.7/113 \pm 9.1$	50/50	1.2
HOPS 160	-38 ± 1.1/-	68 ± 3.6/-	2/-	0.43
HOPS 166	$99 \pm 4.9/0 \pm 1.1$	$239 \pm 17/80 \pm 3.7$	59/40	0.036
HOPS 168	$-7 \pm 3.2/160 \pm 0.2$	$101 \pm 11/33 \pm 0.6$	83/69	0.001
HOPS 169	$15 \pm 0.5/-179 \pm 0.9$	$46 \pm 1.7/62 \pm 2.9$	49/35	0.004
HOPS 174	13 ± 0.4/-	35 ± 1.3/-	85/-	0.004
HOPS 177	-/-6 ± 0.7	-/54 ± 2.4	-/6	0.095
HOPS 178	77 ± 2/-	94 ± 6.7/-	76/-	0.042
HOPS 179	$164 \pm 1.1/16 \pm 0.8$	$60 \pm 3.6/71 \pm 2.6$	60/28	0.091
HOPS 181	$-40 \pm 2/177 \pm 0.4$	$131 \pm 7.8/24 \pm 1.2$	48/12	0.2
HOPS 182	$41 \pm 2.5/-157 \pm 0.1$	$77 \pm 8.2/9 \pm 0.3$	33/16	0.23
HOPS 192	$95 \pm 2.8/-67 \pm 1.6$	$104 \pm 9.3/105 \pm 5.3$	53/34	0.045
HOPS 198	-/112 ± 4.2	-/64 ± 14	-/0	0.12
HOPS 203	-/139 ± 4.5	-/60 ± 15	-/85	0.011
HOPS 355	$-104 \pm 0.4/98 \pm 0.1$	$45 \pm 1.3/8 \pm 0.3$	75/84	0.099
HOPS 368	$30 \pm 12/175 \pm 4.5$	$289 \pm 44/135 \pm 15$	61/84	0.034
HOPS 370	$36 \pm 1.3/24 \pm 0.5$	$66 \pm 4.8/40 \pm 1.9$	37/48	0.044
HOPS 383	128 ± 0.5/-	49 ± 1.7/-	88/-	0.019

[a] Columns with two entries refer to the blue/red outflow lobes separately. Entries marked '-' refer to lobes that are not detected.

[b] γ is the projected angle between the outflow and filament. See Section 5 for details.

[c] $d_{\rm fil}$ is the minimum distance between the outflow source and filament.

REFERENCES

Anathpindika, S., & Whitworth, A. P. 2008, A&A, 487, 605

André, P., Di Francesco, J., Ward-Thompson, D., et al. 2014, in Protostars and Planets VI, ed. H. Beuther, R. S. Klessen, C. P. Dullemond, & T. Henning, 27

Arce, H. G., Borkin, M. A., Goodman, A. A., Pineda, J. E., & Halle, M. W. 2010, ApJ, 715, 1170

Arce, H. G., & Goodman, A. A. 2001, ApJL, 551, L171

Arce, H. G., & Sargent, A. I. 2006, ApJ, 646, 1070

Arzoumanian, D., André, P., Didelon, P., et al. 2011, A&A, 529, L6

Aso, Y., Tatematsu, K., Sekimoto, Y., et al. 2000, ApJS, 131, 465

Table 4: Anderson-Darling p-values.

Sample	Random	Perpendicular
Full	0.23	< 0.001
Definite	> 0.25	0.06
$d_{\rm fil} \leq 0.05$ pc	0.13	0.02
Both	0.06	> 0.25
Stephens et al. (2017)[a]	0.20	0.0045
Kong et al. (2019)[b]	6.5×10^{-5}	0.53

[a]Perseus outflows; $\gamma_{\rm F}$ in their Table 3.

[b]IRDC G28 outflows

Bally, J. 2016, ARA&A, 54, 491

Bally, J., Ginsburg, A., Arce, H., et al. 2017, ApJ, 837, 60

Bally, J., Langer, W. D., Stark, A. A., & Wilson, R. W. 1987, ApJL, 312, L45

Berné, O., Marcelino, N., & Cernicharo, J. 2014, ApJ, 795, 13

Bodenheimer, P. 1995, ARA&A, 33, 199

Brunt, C. M., Heyer, M. H., & Mac Low, M. M. 2009, A&A, 504, 883

Buckle, J. V., Davis, C. J., Francesco, J. D., et al. 2012, MNRAS, 422, 521

Carroll, J. J., Frank, A., & Blackman, E. G. 2010, ApJ, 722, 145

Carroll, J. J., Frank, A., Blackman, E. G., Cunningham, A. J., & Quillen, A. C. 2009, ApJ, 695, 1376

Chen, C.-Y., & Ostriker, E. C. 2014, ApJ, 785, 69

Chini, R., Reipurth, B., Ward-Thompson, D., et al. 1997, ApJL, 474, L135

Choi, M., Kang, M., Lee, J.-E., et al. 2017, ApJS, 232, 24

Clarke, S. D., Whitworth, A. P., Duarte-Cabral, A., & Hubber, D. A. 2017, MNRAS, 468, 2489

Curtis, E. I., Richer, J. S., Swift, J. J., & Williams, J. P. 2010, MNRAS, 408, 1516

Davis, C. J., Dent, W. R. F., Matthews, H. E., Coulson, I. M., & McCaughrean, M. J. 2000, MNRAS, 318, 952

Davis, C. J., Froebrich, D., Stanke, T., et al. 2009, A&A, 496, 153

Downes, T. P., & Cabrit, S. 2007, A&A, 471, 873

Dunham, M. M., Arce, H. G., Mardones, D., et al. 2014, ApJ, 783, 29

Federrath, C. 2015, MNRAS, 450, 4035

Frank, A., Ray, T. P., Cabrit, S., et al. 2014, Protostars and Planets VI, 451

Frerking, M. A., Langer, W. D., & Wilson, R. W. 1982, ApJ, 262, 590

Furlan, E., Fischer, W. J., Ali, B., et al. 2016, ApJS, 224, 5

Goldsmith, P. F., Snell, R. L., Hemeon-Heyer, M., & Langer, W. D. 1984, ApJ, 286, 599

Großschedl, J. E., Alves, J., Meingast, S., et al. 2018, A&A, 619, A106

Hacar, A., Tafalla, M., Kauffmann, J., & Kovács, A. 2013, A&A, 554, A55

Kauffmann, J., Bertoldi, F., Bourke, T. L., Evans, N. J., I., & Lee, C. W. 2008, A&A, 487, 993

Koch, E. W., & Rosolowsky, E. W. 2015, MNRAS, 452, 3435

Kong, S., Arce, H. G., José Maureira, M., et al. 2019, ApJ, 874, 104

Kong, S., Arce, H. G., Feddersen, J. R., et al. 2018, ApJS, 236, 25

Konigl, A., & Pudritz, R. E. 2000, in Protostars and Planets IV, ed. V. Mannings, A. P. Boss, & S. S. Russell, 759

Kounkel, M., Covey, K., Suárez, G., et al. 2018, AJ, 156, 84

Kuhn, M. A., Hillenbrand, L. A., Sills, A., Feigelson, E. D., & Getman, K. V. 2019, ApJ, 870, 32

Langer, W. D., & Penzias, A. A. 1993, ApJ, 408, 539

Lee, J. W. Y., Hull, C. L. H., & Offner, S. S. R. 2017, ApJ, 834, 201

Li, H., Li, D., Qian, L., et al. 2015, ApJS, 219, 20

Li, P. S., & Klein, R. I. 2019, MNRAS, 485, 4509

Li, P. S., Klein, R. I., & McKee, C. F. 2018, MNRAS, 473, 4220

Mac Low, M.-M. 1999, ApJ, 524, 169

McKee, C. F., & Ostriker, E. C. 2007, ARA&A, 45, 565

Megeath, S. T., Gutermuth, R., Muzerolle, J., et al. 2012, AJ, 144, 192

Meingast, S., Alves, J., Mardones, D., et al. 2016, A&A, 587, A153

Menten, K. M., Reid, M. J., Forbrich, J., & Brunthaler, A. 2007, A&A, 474, 515

Morgan, J. A., Schloerb, F. P., Snell, R. L., & Bally, J. 1991, ApJ, 376, 618

Moro-Martín, A., Cernicharo, J., Noriega-Crespo, A., & Martín-Pintado, J. 1999, ApJL, 520, L111

Myers, P. C., & Ladd, E. F. 1993, ApJL, 413, L47

Nakamura, F., & Li, Z.-Y. 2007, ApJ, 662, 395

Nakamura, F., Kamada, Y., Kamazaki, T., et al. 2011, ApJ, 726, 46

Nakamura, F., Miura, T., Kitamura, Y., et al. 2012, ApJ, 746, 25

Offner, S. S. R., Dunham, M. M., Lee, K. I., Arce, H. G., & Fielding, D. B. 2016, ApJL, 827, L11

Offner, S. S. R., Lee, E. J., Goodman, A. A., & Arce, H. 2011, ApJ, 743, 91

Offner, S. S. R., & Liu, Y. 2018, NatAs, 2, 896

Padoan, P., Juvela, M., Kritsuk, A., & Norman, M. L. 2009, ApJ, 707, L153

Plunkett, A. L., Arce, H. G., Corder, S. A., et al. 2015, ApJ, 803, 22

Plunkett, A. L., Arce, H. G., Corder, S. A., et al. 2013, ApJ, 774, 22

Rathborne, J. M., Jackson, J. M., & Simon, R. 2006, ApJ, 641, 389

Ripple, F., Heyer, M. H., Gutermuth, R., Snell, R. L., & Brunt, C. M. 2013, MNRAS, 431, 1296

Rohlfs, K., & Wilson, T. L. 1996, Tools of Radio Astronomy, 127

Schmid-Burgk, J., Guesten, R., Mauersberger, R., Schulz, A., & Wilson, T. L. 1990, ApJL, 362, L25

Shimajiri, Y., Takahashi, S., Takakuwa, S., Saito, M., & Kawabe, R. 2008, ApJ, 683, 255

—. 2009, PASJ, 61, 1055

Shimajiri, Y., Kawabe, R., Takakuwa, S., et al. 2011, PASJ, 63, 105

Shu, F. H., Najita, J. R., Shang, H., & Li, Z. Y. 2000, in Protostars and Planets IV, ed. V. Mannings, A. P. Boss, & S. S. Russell, 789–814

Sousbie, T. 2011, MNRAS, 414, 350

Stanke, T., McCaughrean, M. J., & Zinnecker, H. 2002, A&A, 392, 239

Stanke, T., & Williams, J. P. 2007, AJ, 133, 1307

Stephens, I. W., Dunham, M. M., Myers, P. C., et al. 2017, ApJ, 846, 16

Stephens, M. A. 1974, Journal of the American Statistical Association, 69, 730

Suri, S., Sánchez-Monge, Á., Schilke, P., et al. 2019, A&A, 623, A142

Takahashi, S., Saito, M., Ohashi, N., et al. 2008, ApJ, 688, 344

Tanabe, Y., Nakamura, F., Tsukagoshi, T., et al. 2019, submitted, PASJ

Teixeira, P. S., Takahashi, S., Zapata, L. A., & Ho, P. T. P. 2016, A&A, 587, A47

Williams, J. P., Plambeck, R. L., & Heyer, M. H. 2003, ApJ, 591, 1025

Wilson, B. A., Dame, T. M., Masheder, M. R. W., & Thaddeus, P. 2005, A&A, 430, 523

Zapata, L. A., Rodríguez, L. F., Ho, P. T. P., et al. 2005, ApJL, 630, L85

Zhang, Y., Arce, H. G., Mardones, D., et al. 2016, ApJ, 832, 158

APPENDIX

A. PROTOSTELLAR PROPERTIES

The HOPS catalog from Furlan et al. (2016) compiles photometric measurements for protostars from 1.2-870 μm. From these SEDs, they calculate the bolometric luminosity $L_{\rm bol}$ and temperature $T_{\rm bol}$. $L_{\rm bol}$ is calculated by integrating the observed SED directly. $L_{\rm bol}$, if dominated by accretion luminosity, is a function of the accretion rate and protostellar mass (Takahashi et al. 2008). Since accretion adds mass to the protostar, $L_{\rm bol}$ may be considered a proxy for the protostellar mass. $T_{\rm bol}$ is the temperature of a blackbody with the same mean frequency as the observed SED. $T_{\rm bol}$ increases as a protostar evolves and clears its envelope, making it a proxy for protostellar age (Myers & Ladd 1993). While $L_{\rm bol}$ and $T_{\rm bol}$ are generally thought to trace the protostellar mass and age, respectively, other factors such as extinction and inclination may also affect these measurements. For the 40 outflows presented here with associated HOPS sources, we show the correlation between the protostellar $L_{\rm bol}$ and $T_{\rm bol}$ and outflow properties in Figure 12. Arce & Sargent (2006) discovered a correlation between outflow opening angle and protostellar age, as traced by $T_{\rm bol}$. They found that more evolved (hotter $T_{\rm bol}$) protostars drive wider outflows. Figure 12 shows that our measured outflow opening angles are not correlated with $T_{\rm bol}$ or $L_{\rm bol}$.

Takahashi et al. (2008) investigated the relationship between momentum flux (identical to our $\dot{P}$) and $L_{\rm bol}$ in the outflows they identified in OMC-2/3. In their Figure 12, they show these outflows are consistent with a trend of increasing with increasing $L_{\rm bol}$ spanning six orders of magnitude in $L_{\rm bol}$. As shown in Figure 12, we find no evidence for a correlation between and $L_{\rm bol}$ within our outflow sample. However, our measurements are consistent with the scatter seen in Figure 12 of Takahashi et al. (2008). Figure 12 also shows the lack of correlation between the protostellar $T_{\rm bol}$ or $L_{\rm bol}$ with the outflow momentum P, kinetic energy E, energy injection rate , and dynamical time $t_{\rm dyn}$.

We also look for any difference in the outflow-filament alignment as a function of protostellar $T_{\rm bol}$ and $L_{\rm bol}$. In Perseus, older, less embedded, hotter $T_{\rm bol}$ protostars show a slightly more perpendicular outflow-filament alignment than younger protostars (Stephens et al. 2017). In Figure 13, we show the outflow-filament alignment in Orion A among HOPS protostars, split into low- and high-$T_{\rm bol}$ and $L_{\rm bol}$ samples. There is no significant difference between the low- and high-$T_{\rm bol}$ outflow-filament alignment. The high-$L_{\rm bol}$ outflows are slightly more consistent with a perpendicular outflow-filament alignment compare to the low-$L_{\rm bol}$ sample.

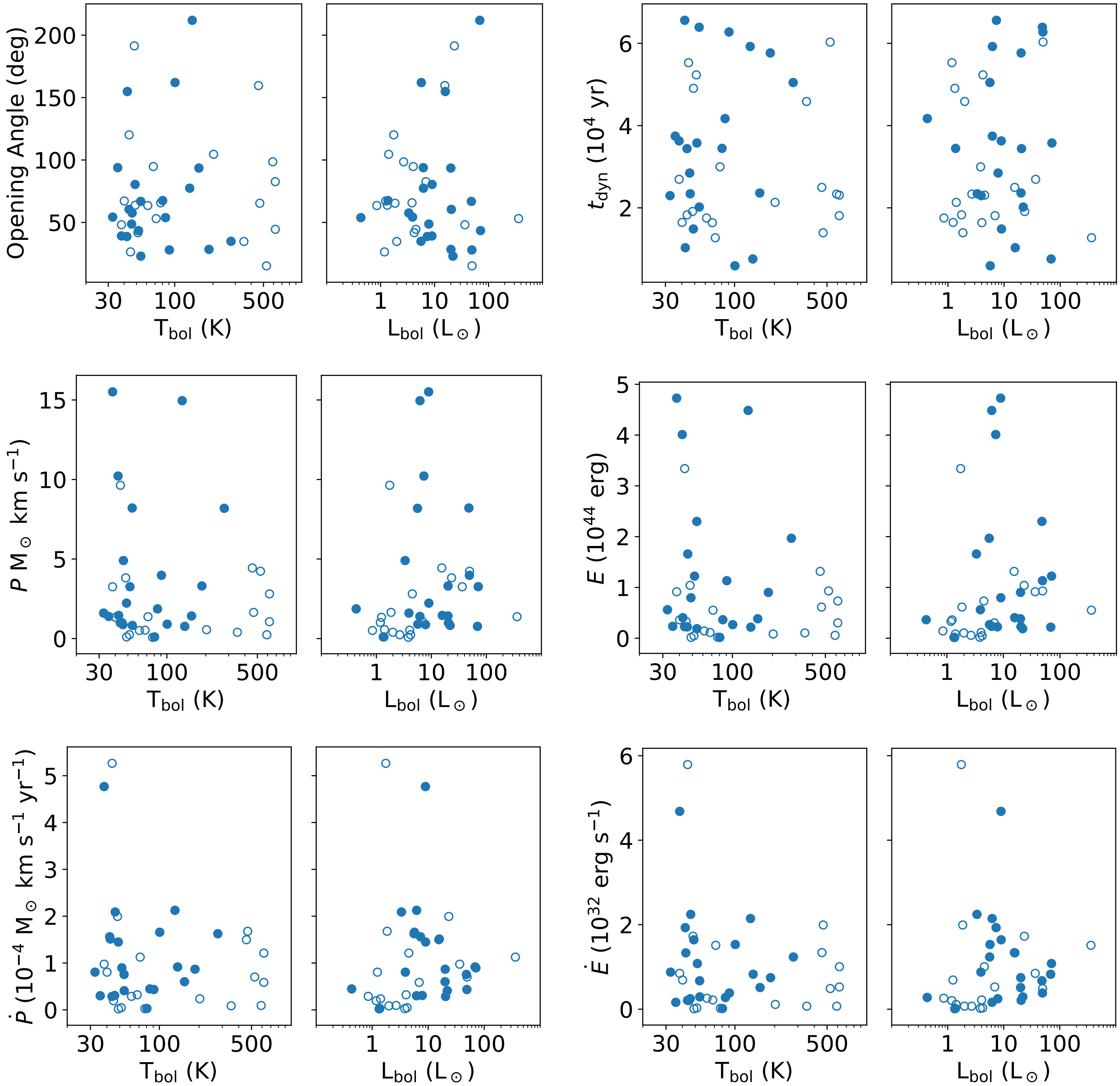

Figure 12: Protostellar $T_{\rm bol}$ and $L_{\rm bol}$ plotted against outflow properties for 40 outflows driven by HOPS sources. The outflow properties are the average of both lobes, when detected. Filled circles indicate outflows with a confidence level of "definite" for all detected lobes. Open circles indicate outflows with at least one "marginal" lobe. The outflow properties are given in Tables 2 and 3.

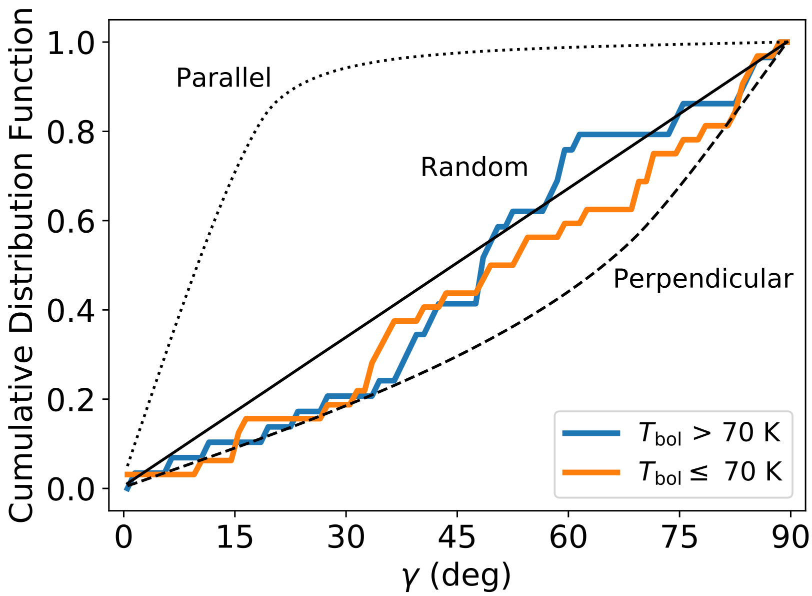

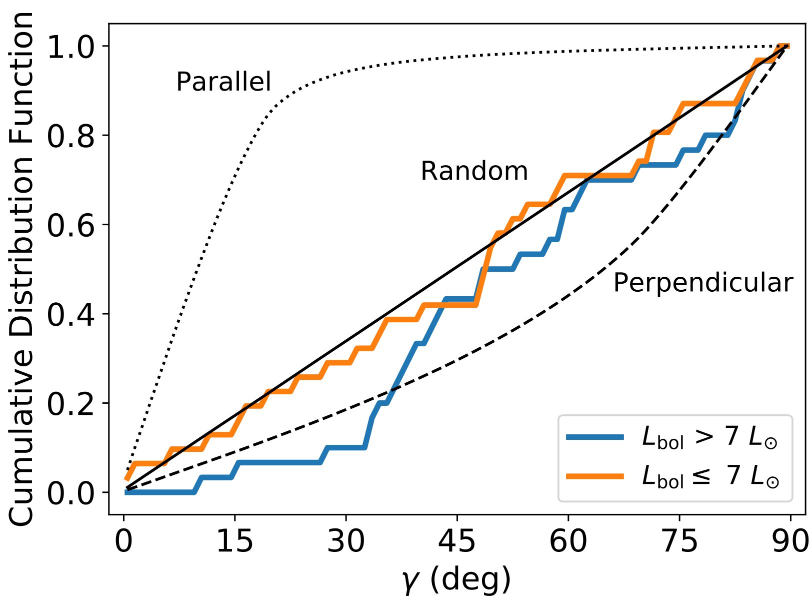

Figure 13: Outflow-filament alignment in low- and high-$T_{\rm bol}$ and $L_{\rm bol}$ samples. Symbols are the same as Figure 11.

B. ALL OUTFLOWS IN CARMA-NRO ORION

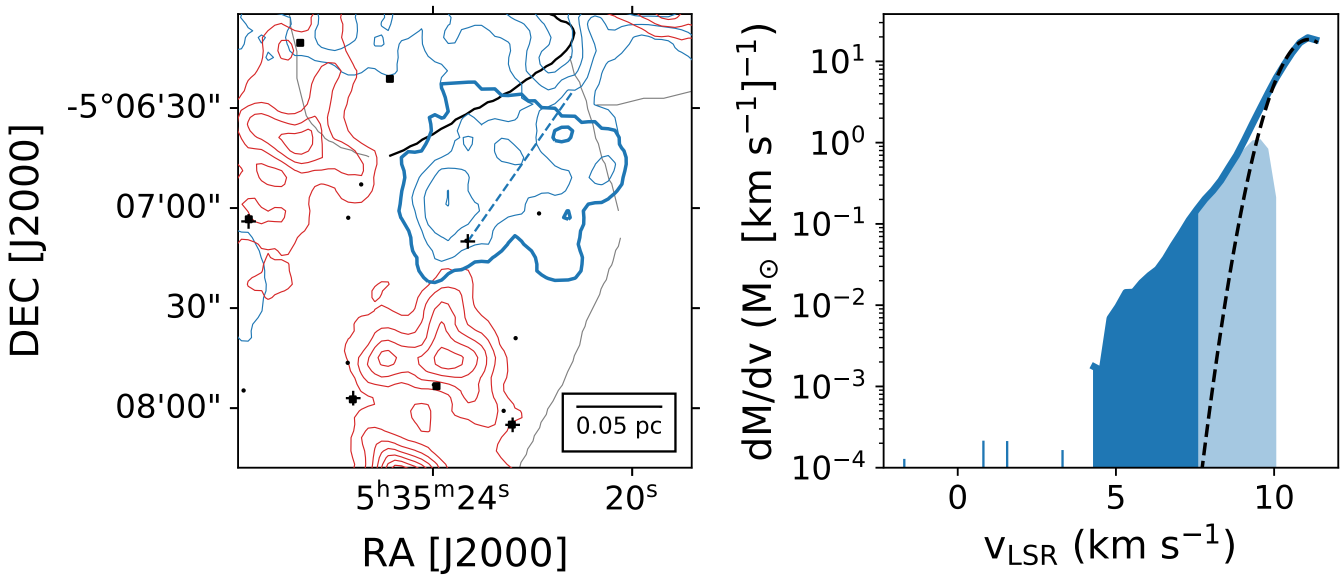

Figure 14: SMZ 11 outflow. The left panel shows the outflow, position angle, nearby sources, and filaments. The velocity range of integration is given by v_{blue}/v_{red} in Table 1 and the contours go from 5 to 50σ in steps of 5σ. Symbols are the same as Figure 2. The right panel shows the mass spectrum with fit. Symbols are the same as Figure 6.

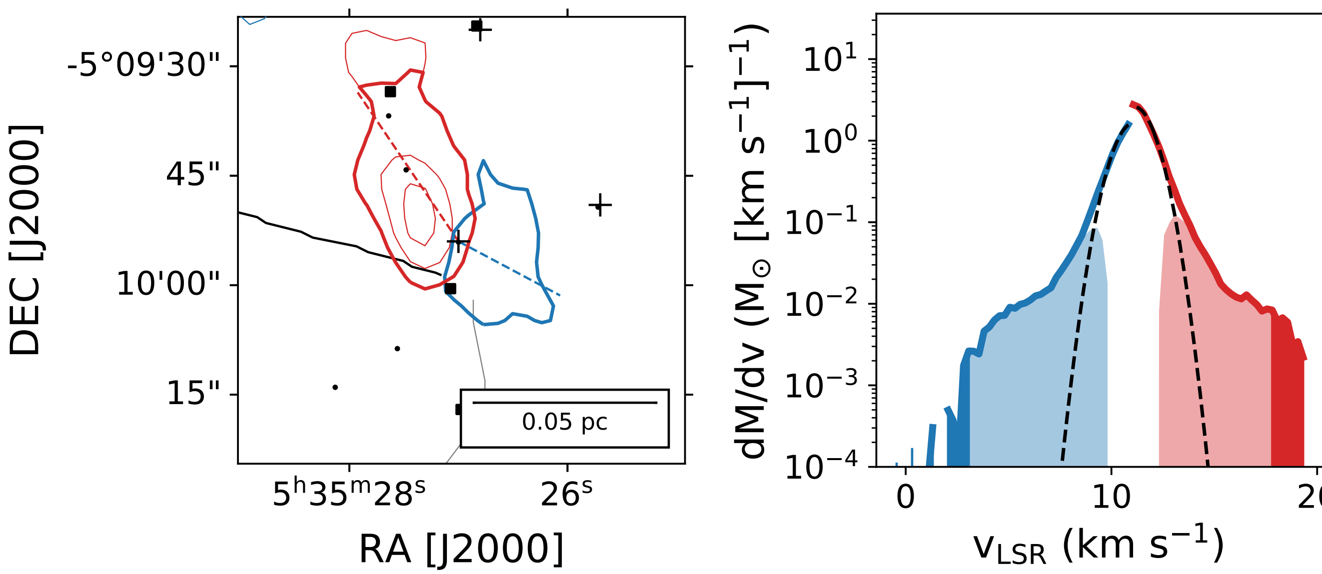

Figure 15: SMZ 17 outflow. The left panel shows the outflow, position angle, nearby sources, and filaments. The velocity range of integration is given by v_{blue}/v_{red} in Table 1 and the contours go from 5 to 50σ in steps of 5σ. Symbols are the same as Figure 2. The right panel shows the mass spectrum with fit. Symbols are the same as Figure 6.

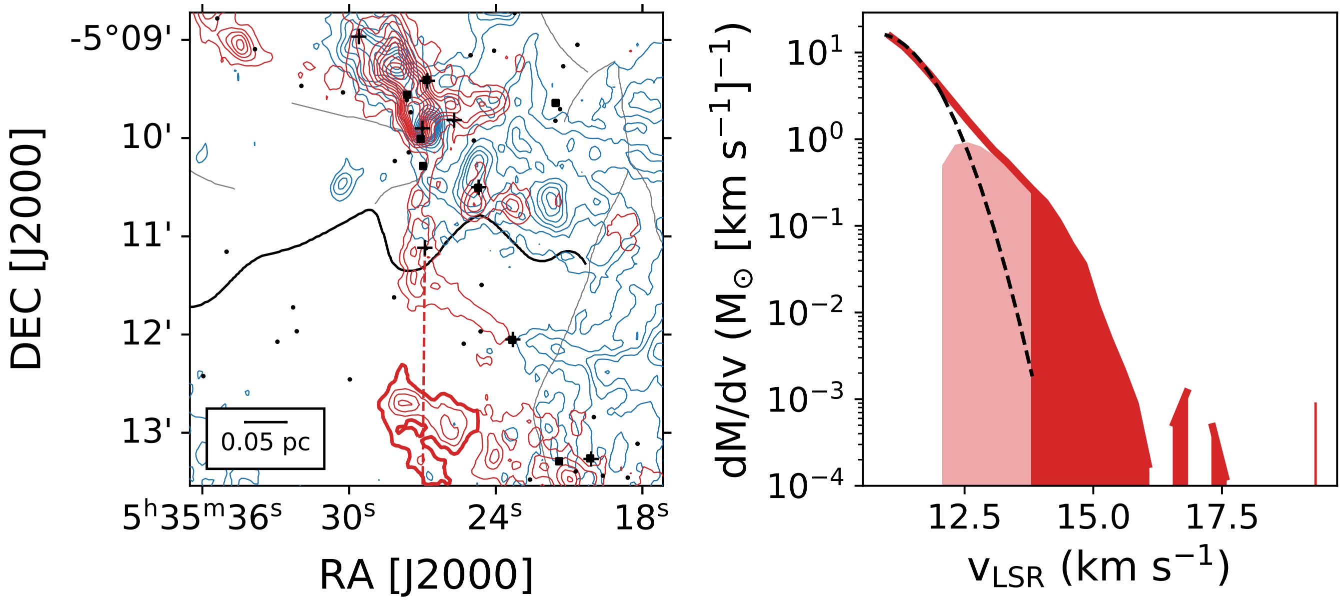

Figure 16: SMZ 21 outflow. The left panel shows the outflow, position angle, nearby sources, and filaments. The velocity range of integration is given by v_{blue}/v_{red} in Table 1 and the contours go from 5 to 50σ in steps of 5σ. Symbols are the same as Figure 2. The right panel shows the mass spectrum with fit. Symbols are the same as Figure 6.

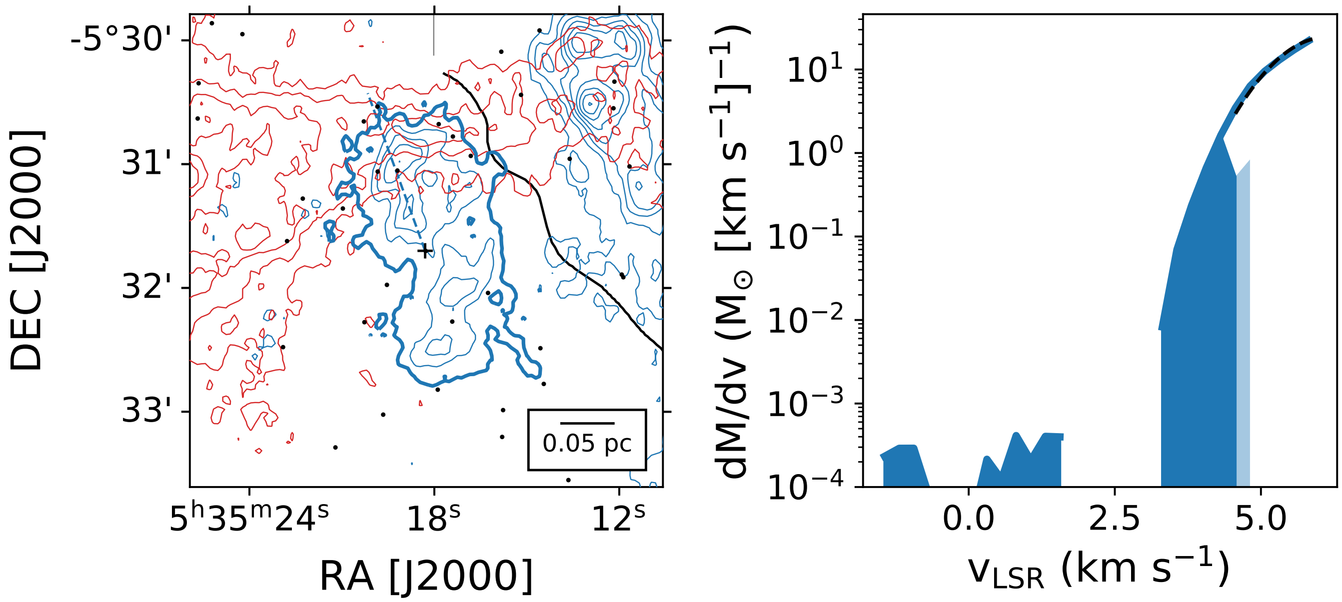

Figure 17: SMZ 30 outflow. The left panel shows the outflow, position angle, nearby sources, and filaments. The velocity range of integration is given by v_{blue}/v_{red} in Table 1 and the contours go from 5 to 50σ in steps of 5σ. Symbols are the same as Figure 2. The right panel shows the mass spectrum with fit. Symbols are the same as Figure 6.

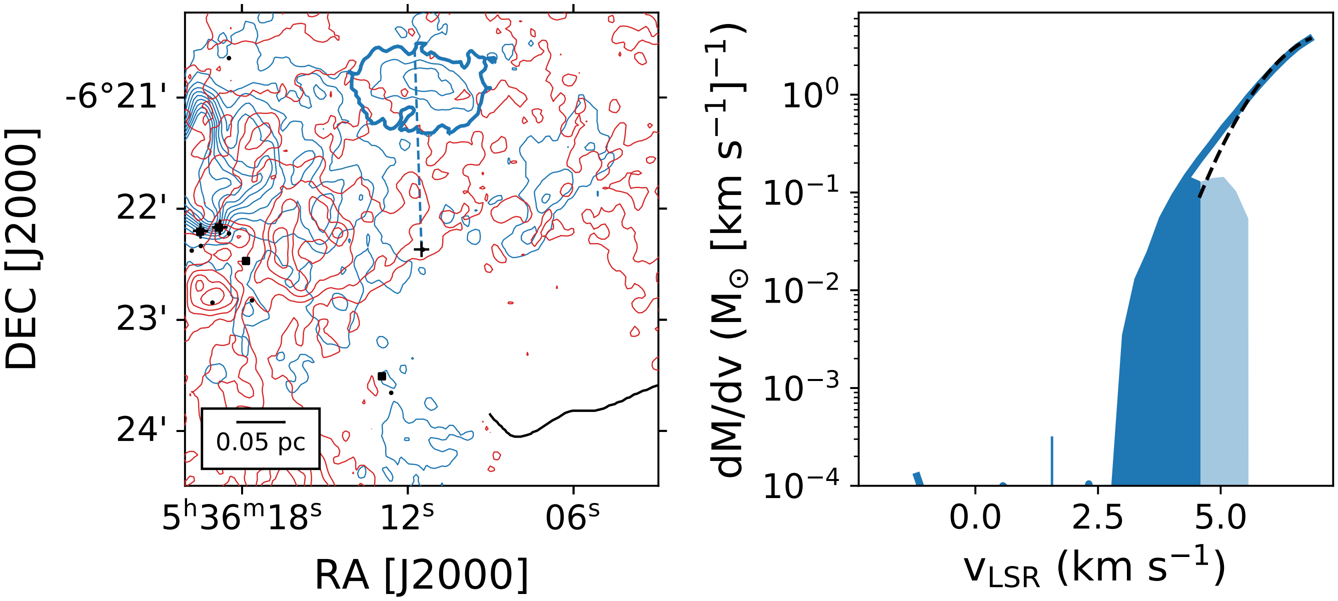

Figure 18: SMZ 50 outflow. The left panel shows the outflow, position angle, nearby sources, and filaments. The velocity range of integration is given by v_{blue}/v_{red} in Table 1 and the contours go from 5 to 50σ in steps of 5σ. Symbols are the same as Figure 2. The right panel shows the mass spectrum with fit. Symbols are the same as Figure 6.

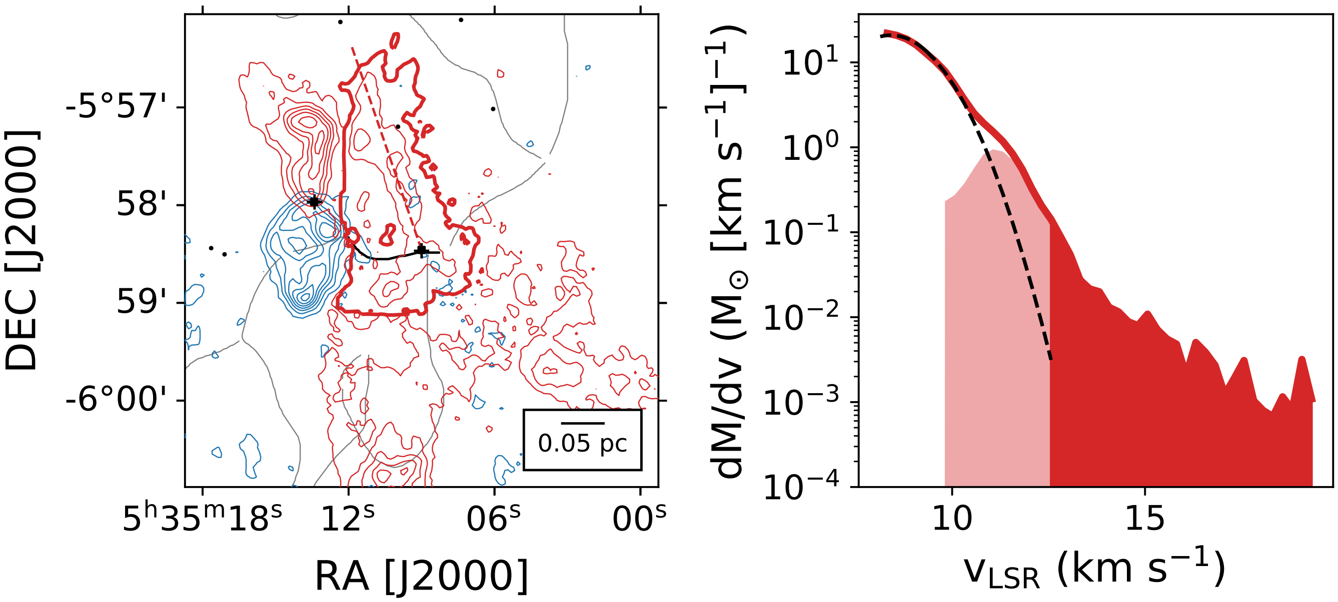

Figure 19: HOPS 10 outflow. The left panel shows the outflow, position angle, nearby sources, and filaments. The velocity range of integration is given by v_{blue}/v_{red} in Table 1 and the contours go from 5 to 50σ in steps of 5σ. Symbols are the same as Figure 2. The right panel shows the mass spectrum with fit. Symbols are the same as Figure 6.

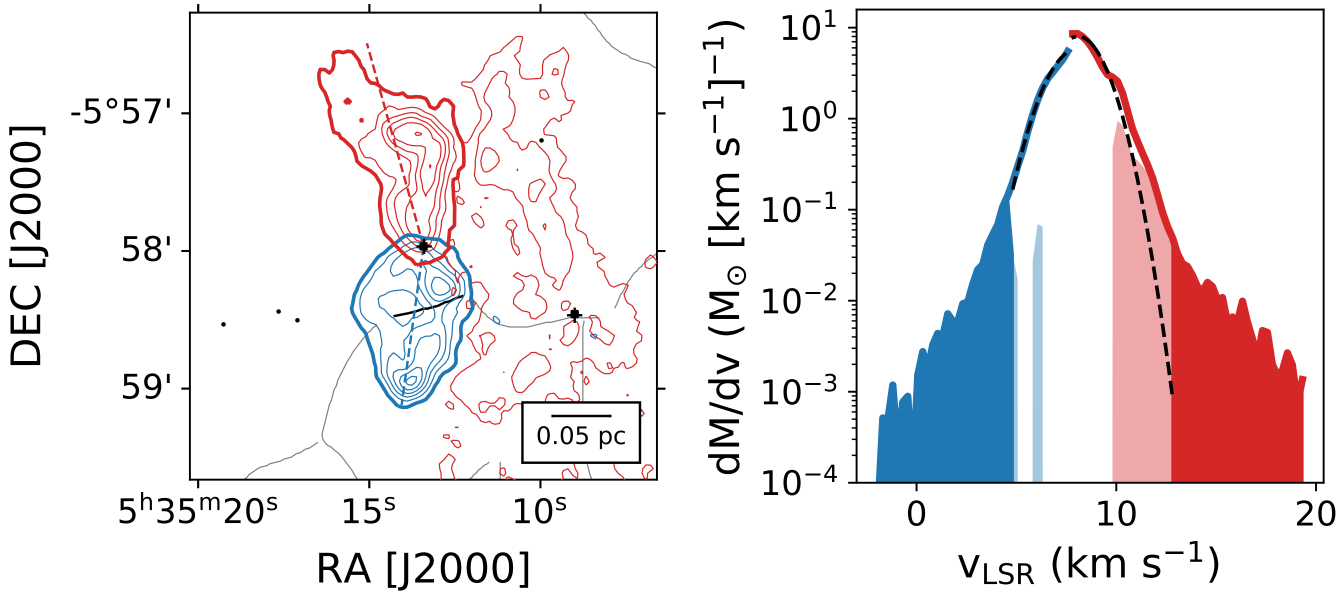

Figure 20: HOPS 11 outflow. The left panel shows the outflow, position angle, nearby sources, and filaments. The velocity range of integration is given by $v_{\rm blue}/v_{\rm red}$ in Table 1 and the contours go from 5 to 50σ in steps of 5σ. Symbols are the same as Figure 2. The right panel shows the mass spectrum with fit. Symbols are the same as Figure 6.

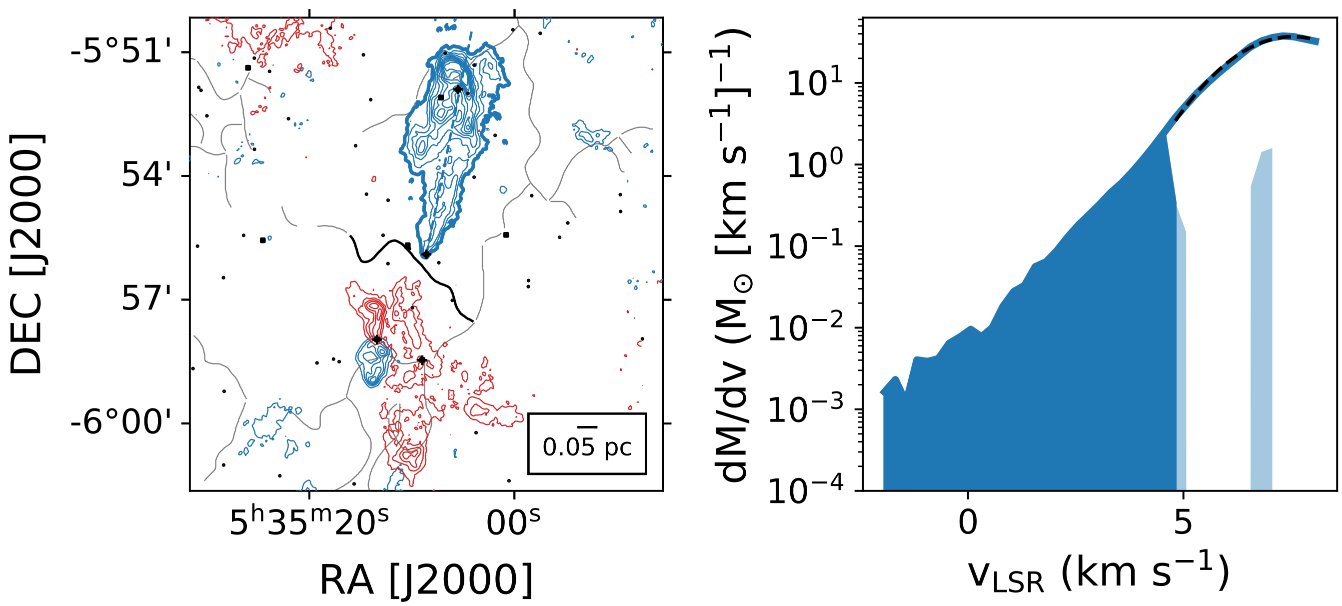

Figure 21: HOPS 12 outflow. The left panel shows the outflow, position angle, nearby sources, and filaments. The velocity range of integration is given by $v_{\rm blue}/v_{\rm red}$ in Table 1 and the contours go from 5 to 50σ in steps of 5σ. Symbols are the same as Figure 2. The right panel shows the mass spectrum with fit. Symbols are the same as Figure 6.

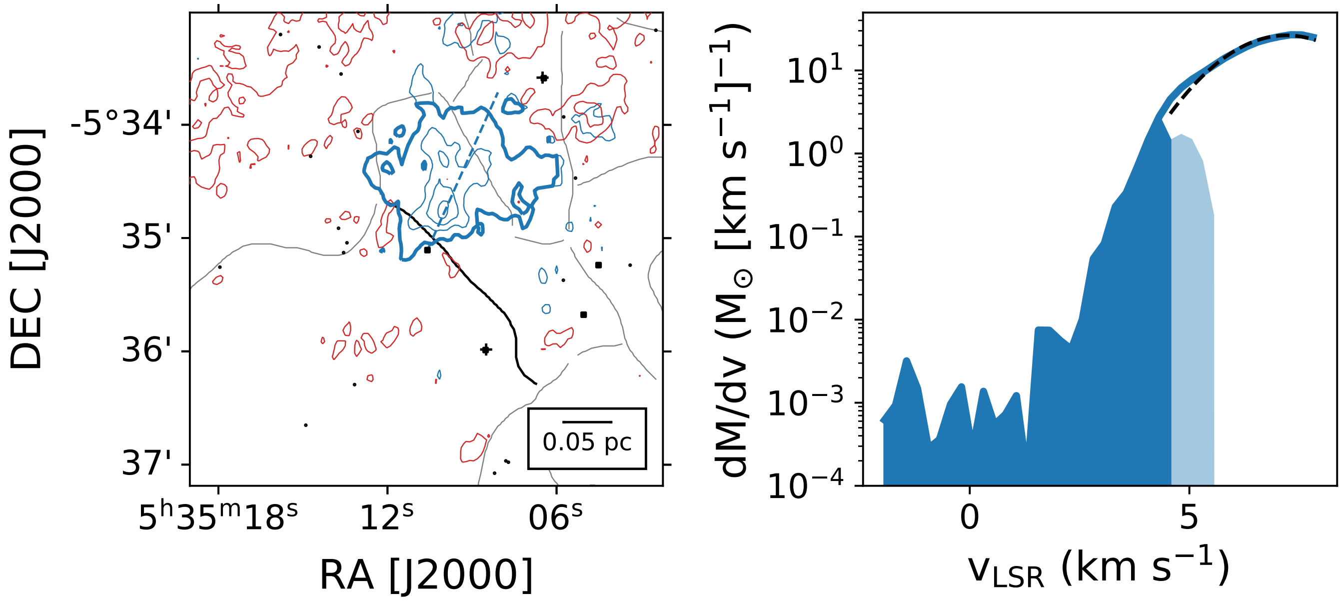

Figure 22: HOPS 44 outflow. The left panel shows the outflow, position angle, nearby sources, and filaments. The velocity range of integration is given by v_{blue}/v_{red} in Table 1 and the contours go from 5 to 50σ in steps of 5σ. Symbols are the same as Figure 2. The right panel shows the mass spectrum with fit. Symbols are the same as Figure 6.

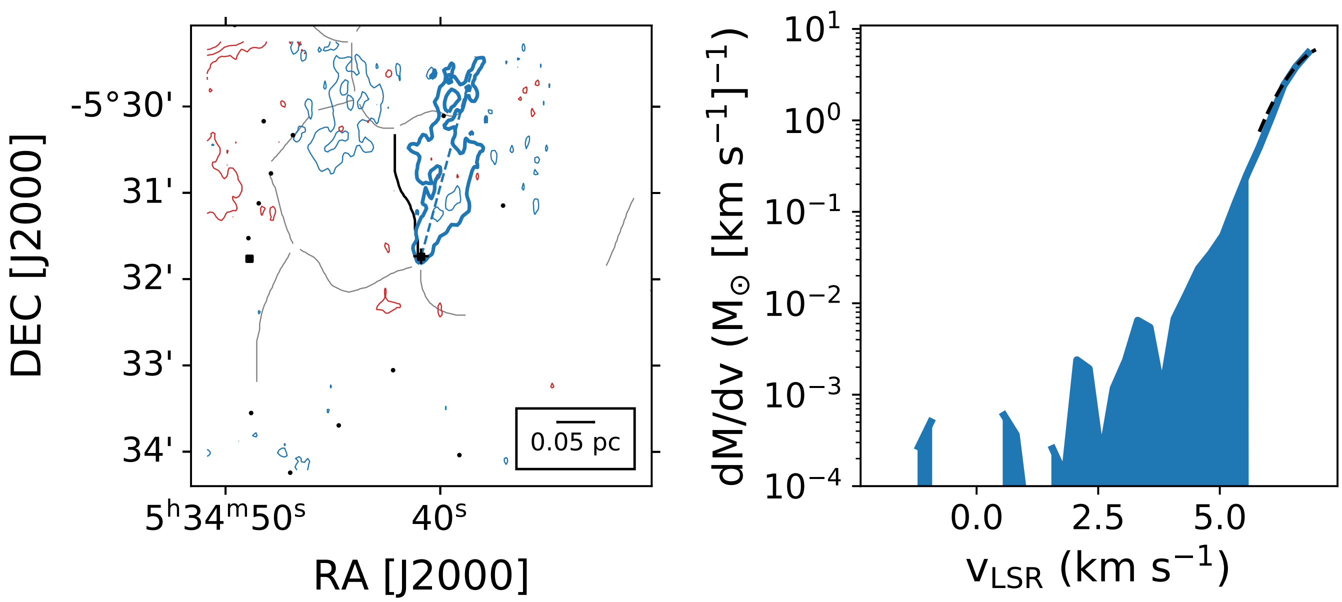

Figure 23: HOPS 50 outflow. The left panel shows the outflow, position angle, nearby sources, and filaments. The velocity range of integration is given by v_{blue}/v_{red} in Table 1 and the contours go from 5 to 50σ in steps of 5σ. Symbols are the same as Figure 2. The right panel shows the mass spectrum with fit. Symbols are the same as Figure 6.

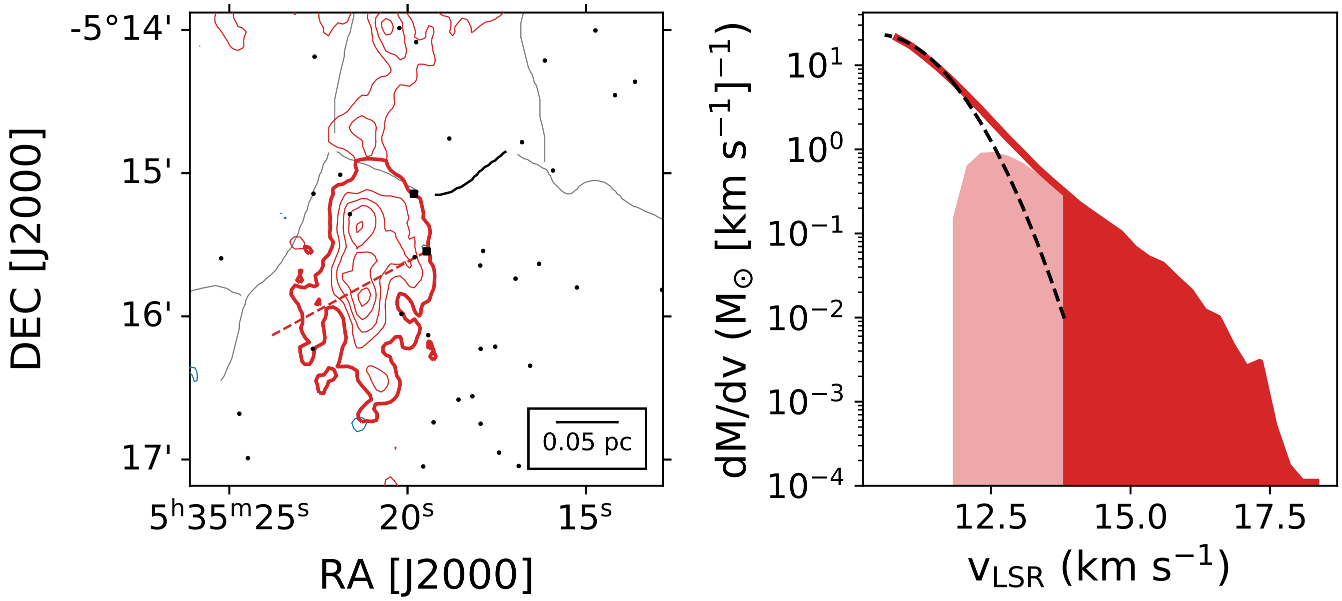

Figure 24: HOPS 56 outflow. The left panel shows the outflow, position angle, nearby sources, and filaments. The velocity range of integration is given by v_{blue}/v_{red} in Table 1 and the contours go from 5 to 50σ in steps of 5σ. Symbols are the same as Figure 2. The right panel shows the mass spectrum with fit. Symbols are the same as Figure 6.

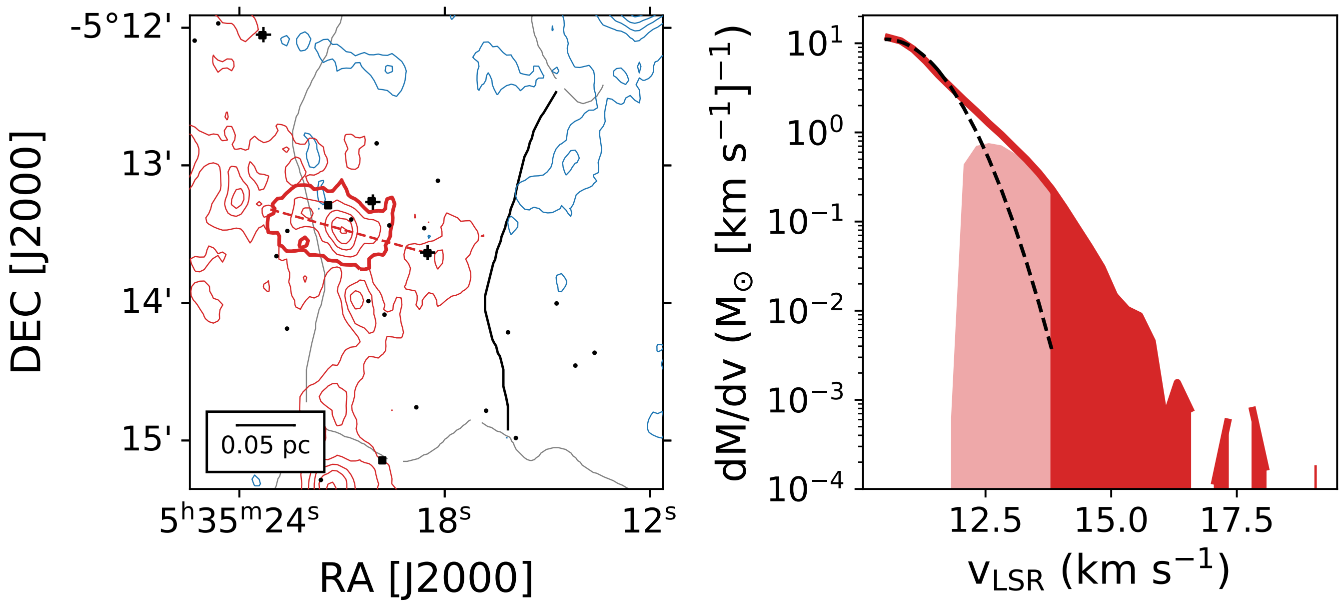

Figure 25: HOPS 58 outflow. The left panel shows the outflow, position angle, nearby sources, and filaments. The velocity range of integration is given by v_{blue}/v_{red} in Table 1 and the contours go from 5 to 50σ in steps of 5σ. Symbols are the same as Figure 2. The right panel shows the mass spectrum with fit. Symbols are the same as Figure 6.

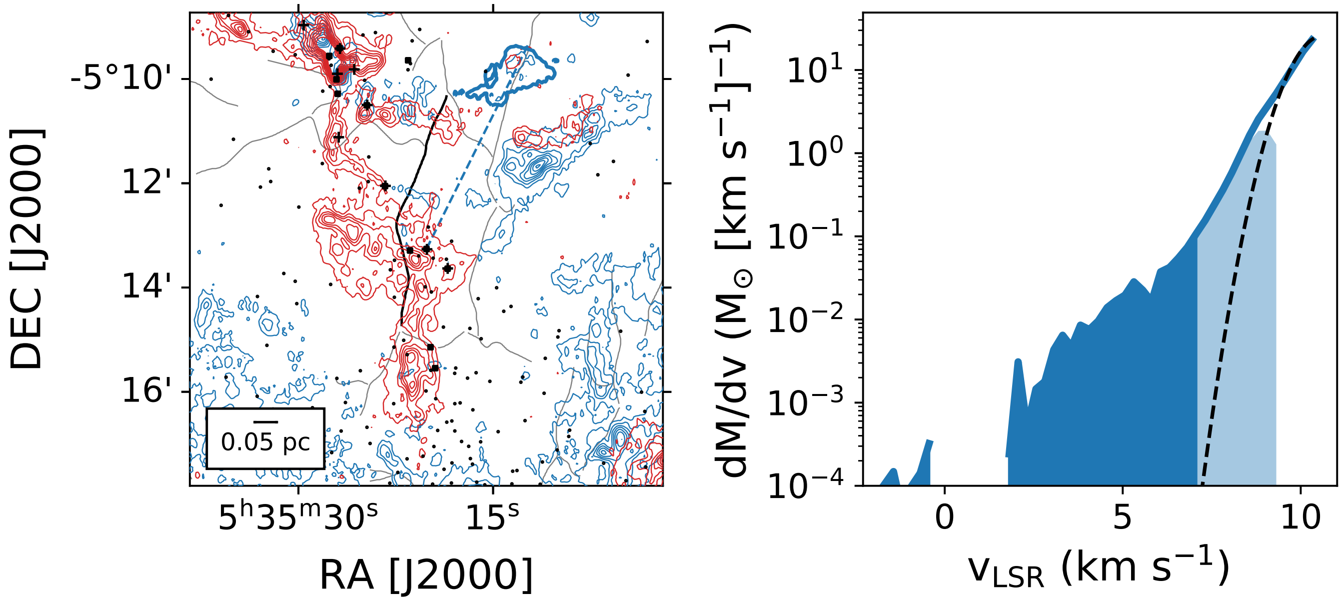

Figure 26: HOPS 59 outflow. The left panel shows the outflow, position angle, nearby sources, and filaments. The velocity range of integration is given by v_{blue}/v_{red} in Table 1 and the contours go from 5 to 50σ in steps of 5σ. Symbols are the same as Figure 2. The right panel shows the mass spectrum with fit. Symbols are the same as Figure 6.

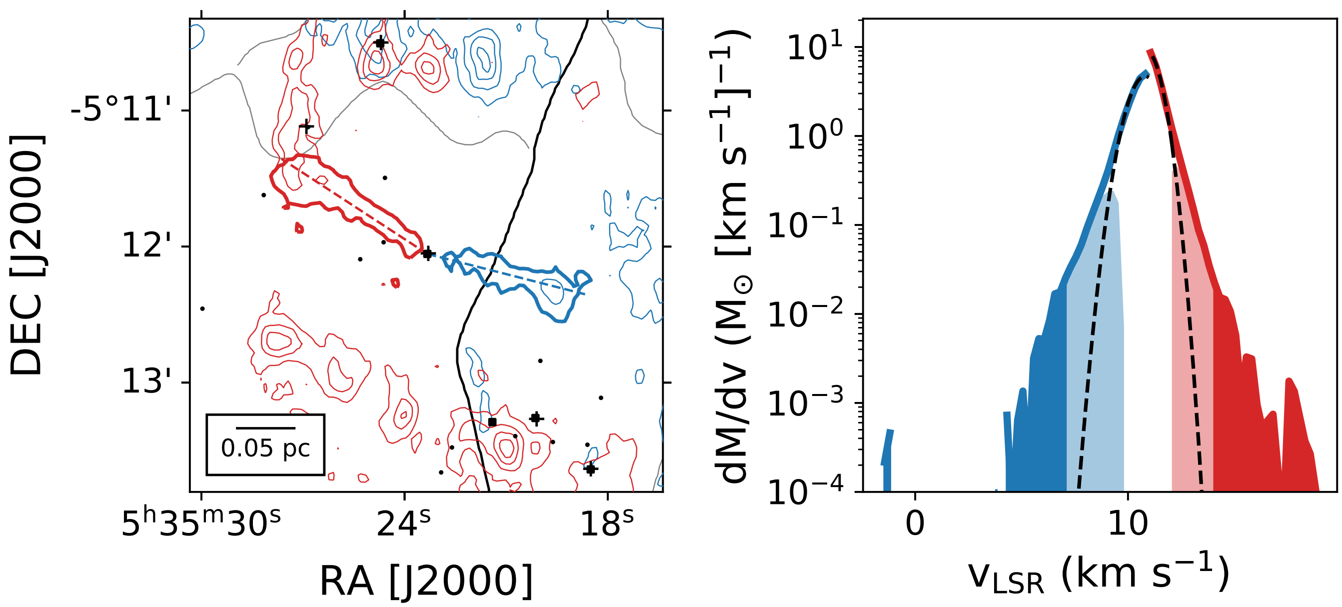

Figure 27: HOPS 60 outflow. The left panel shows the outflow, position angle, nearby sources, and filaments. The velocity range of integration is given by v_{blue}/v_{red} in Table 1 and the contours go from 5 to 50σ in steps of 5σ. Symbols are the same as Figure 2. The right panel shows the mass spectrum with fit. Symbols are the same as Figure 6.

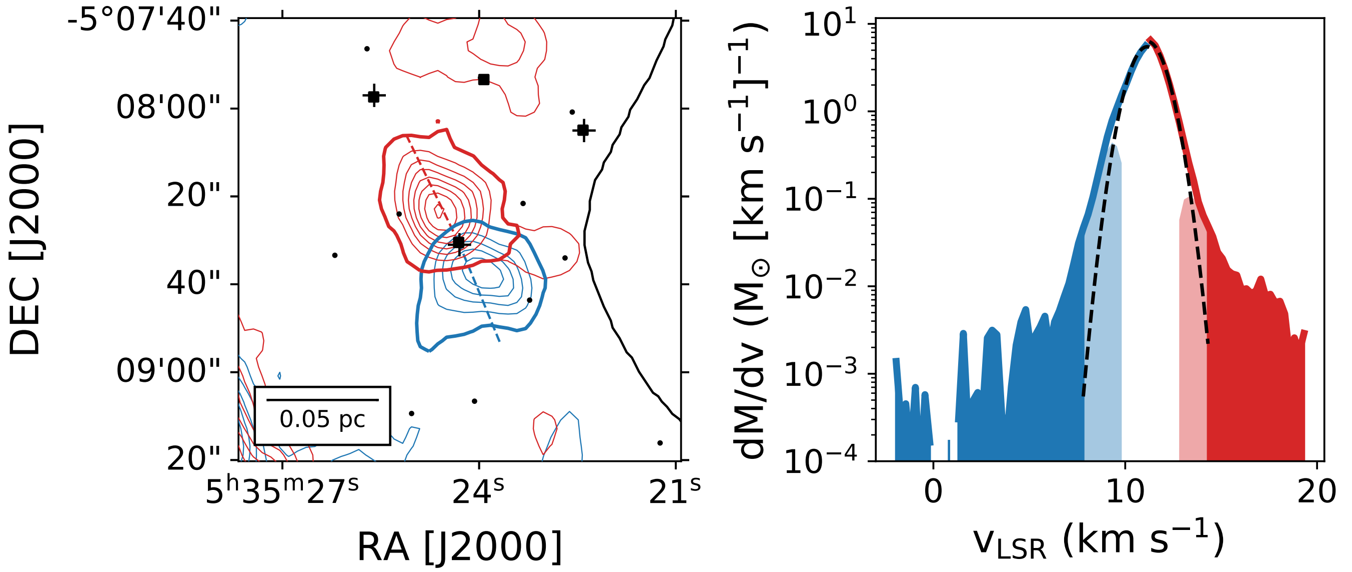

Figure 28: HOPS 68 outflow. The left panel shows the outflow, position angle, nearby sources, and filaments. The velocity range of integration is given by v_{blue}/v_{red} in Table 1 and the contours go from 5 to 50σ in steps of 5σ. Symbols are the same as Figure 2. The right panel shows the mass spectrum with fit. Symbols are the same as Figure 6.

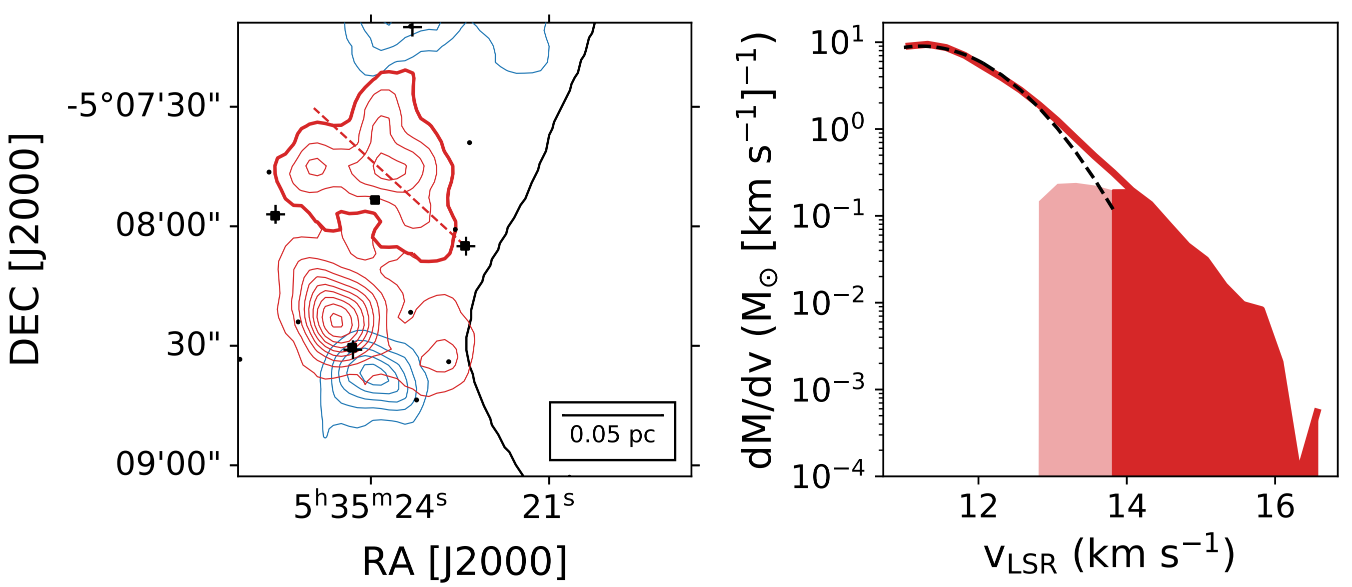

Figure 29: HOPS 70 outflow. The left panel shows the outflow, position angle, nearby sources, and filaments. The velocity range of integration is given by v_{blue}/v_{red} in Table 1 and the contours go from 5 to 50σ in steps of 5σ. Symbols are the same as Figure 2. The right panel shows the mass spectrum with fit. Symbols are the same as Figure 6.

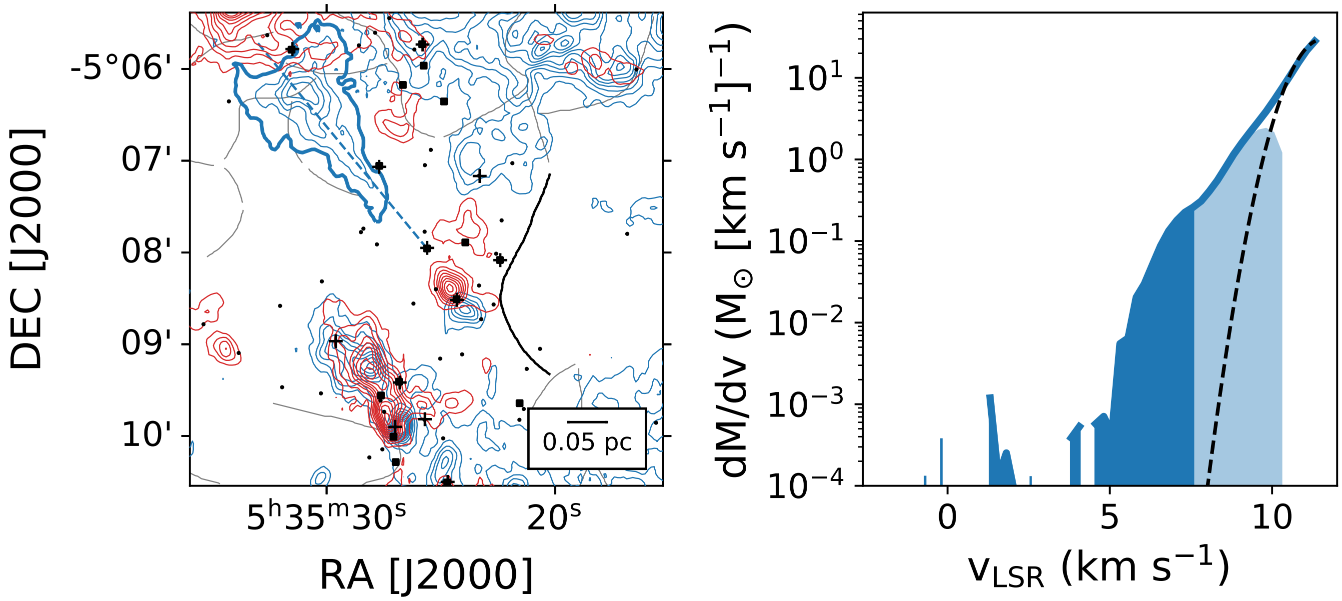

Figure 30: HOPS 71 outflow. The left panel shows the outflow, position angle, nearby sources, and filaments. The velocity range of integration is given by v_{blue}/v_{red} in Table 1 and the contours go from 5 to 50σ in steps of 5σ. Symbols are the same as Figure 2. The right panel shows the mass spectrum with fit. Symbols are the same as Figure 6.

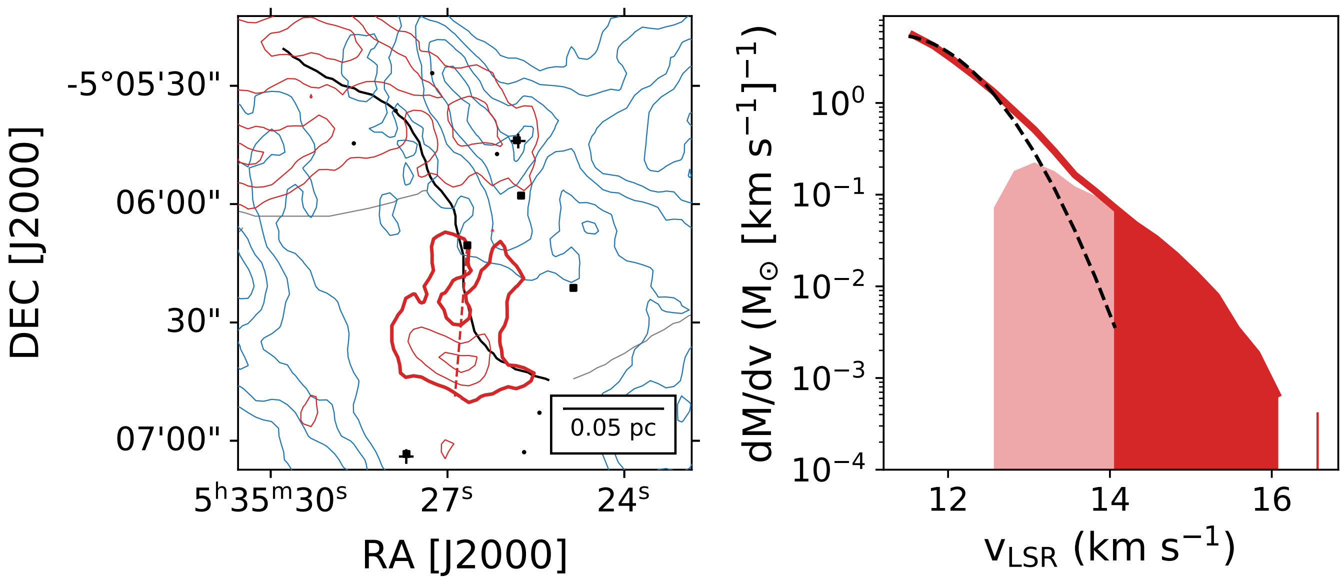

Figure 31: HOPS 75 outflow. The left panel shows the outflow, position angle, nearby sources, and filaments. The velocity range of integration is given by v_{blue}/v_{red} in Table 1 and the contours go from 5 to 50σ in steps of 5σ. Symbols are the same as Figure 2. The right panel shows the mass spectrum with fit. Symbols are the same as Figure 6.

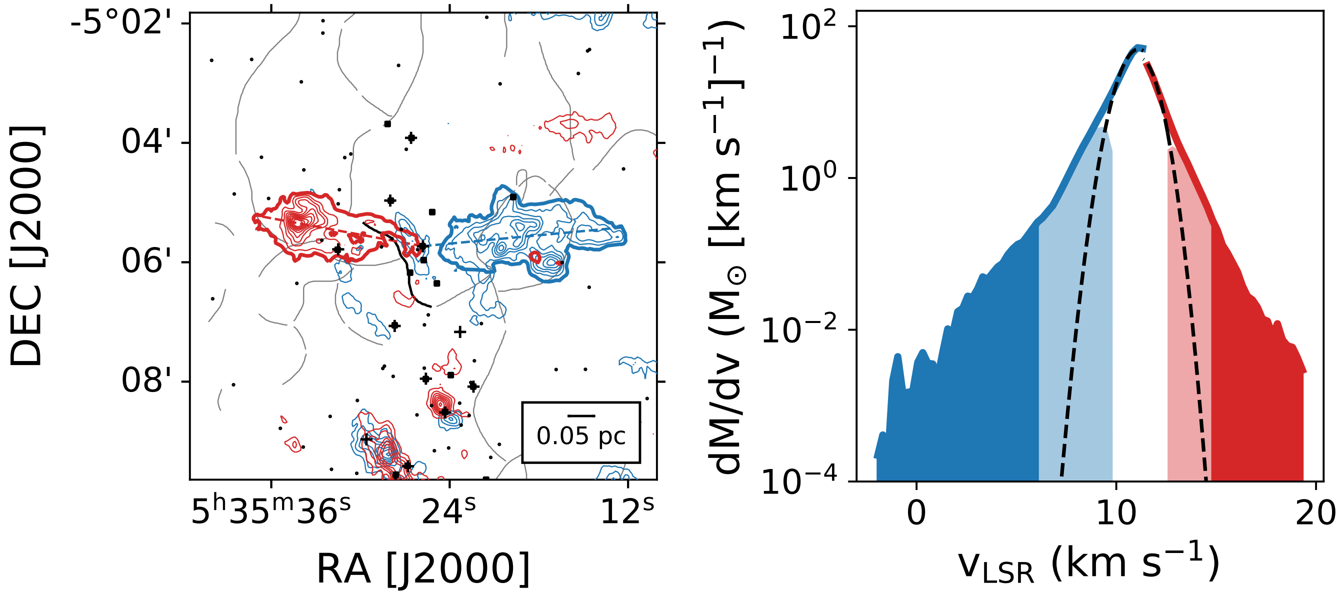

Figure 32: HOPS 78 outflow. The left panel shows the outflow, position angle, nearby sources, and filaments. The velocity range of integration is given by v_{blue}/v_{red} in Table 1 and the contours go from 5 to 50σ in steps of 5σ. Symbols are the same as Figure 2. The right panel shows the mass spectrum with fit. Symbols are the same as Figure 6.

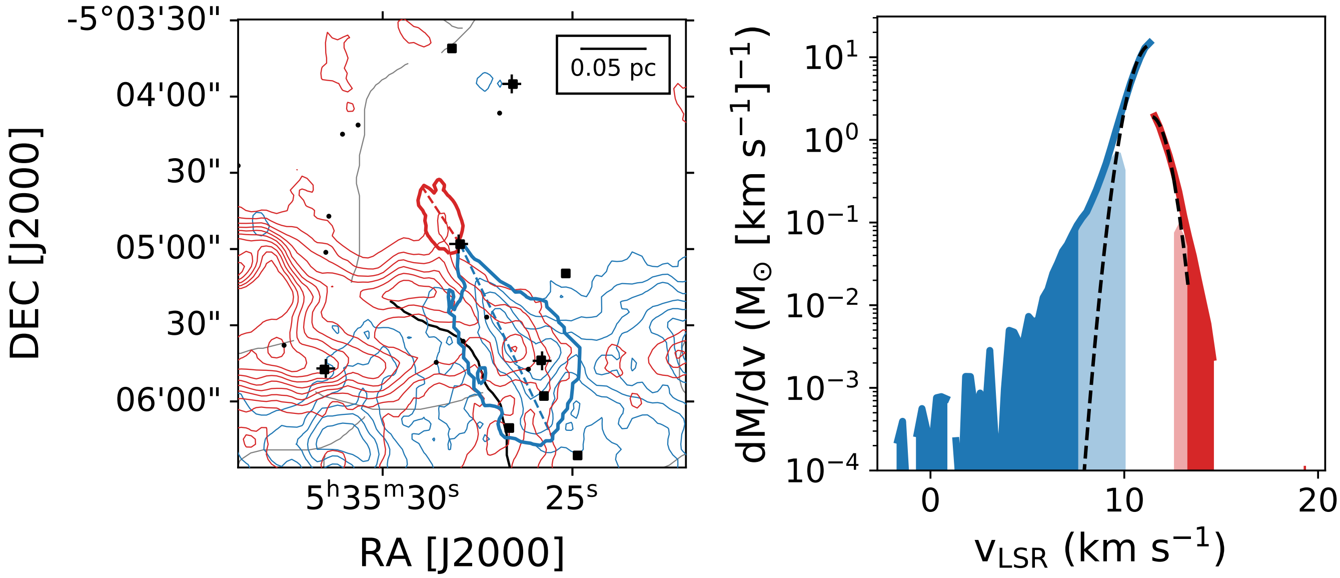

Figure 33: HOPS 81 outflow. The left panel shows the outflow, position angle, nearby sources, and filaments. The velocity range of integration is given by v_{blue}/v_{red} in Table 1 and the contours go from 5 to 50σ in steps of 5σ. Symbols are the same as Figure 2. The right panel shows the mass spectrum with fit. Symbols are the same as Figure 6.

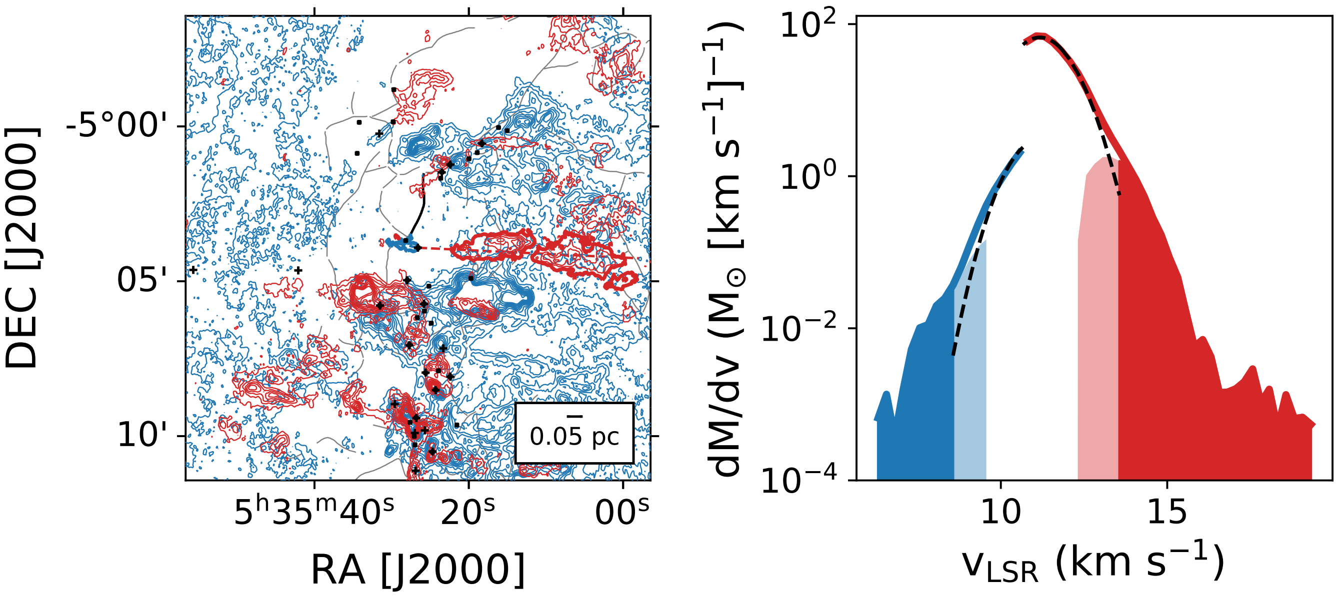

Figure 34: HOPS 84 outflow. The left panel shows the outflow, position angle, nearby sources, and filaments. The velocity range of integration is given by $v_{\rm blue}/v_{\rm red}$ in Table 1 and the contours go from 5 to 50σ in steps of 5σ. Symbols are the same as Figure 2. The right panel shows the mass spectrum with fit. Symbols are the same as Figure 6.

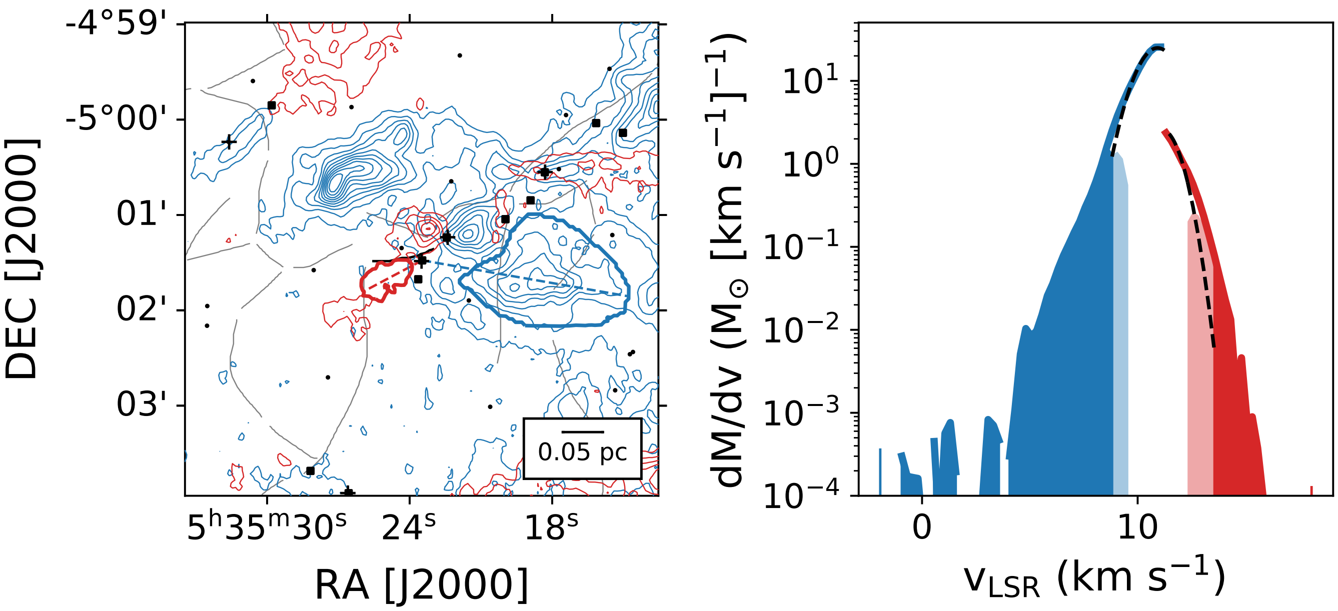

Figure 35: HOPS 87 outflow. The left panel shows the outflow, position angle, nearby sources, and filaments. The velocity range of integration is given by $v_{\rm blue}/v_{\rm red}$ in Table 1 and the contours go from 5 to 50σ in steps of 5σ. Symbols are the same as Figure 2. The right panel shows the mass spectrum with fit. Symbols are the same as Figure 6.

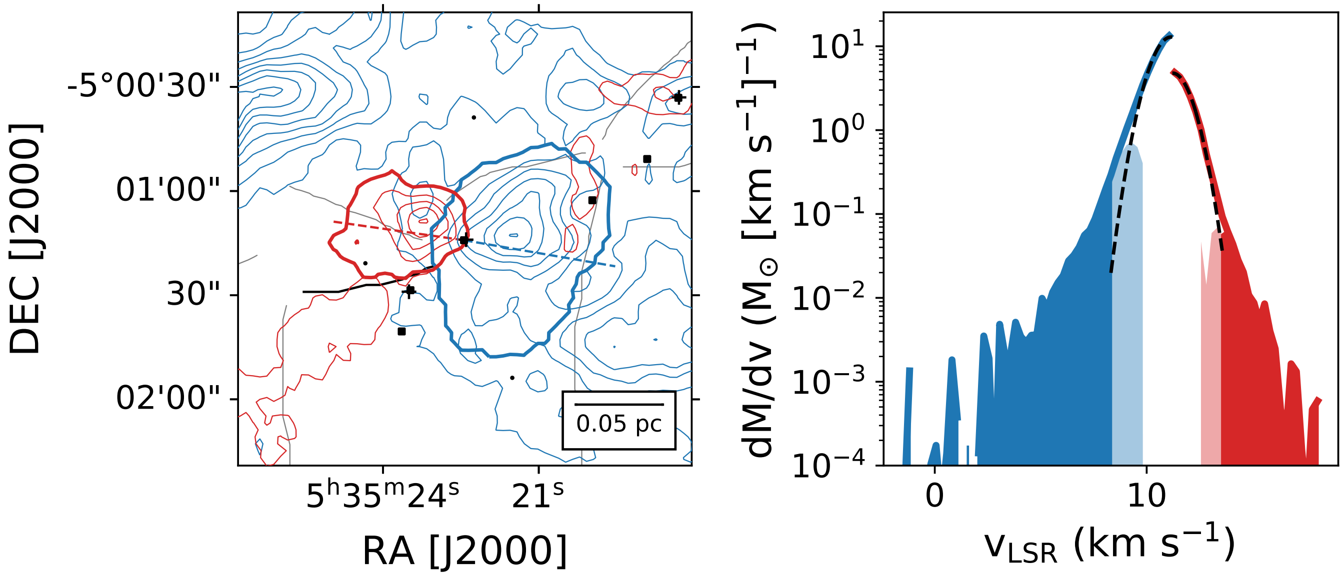

Figure 36: HOPS 88 outflow. The left panel shows the outflow, position angle, nearby sources, and filaments. The velocity range of integration is given by v_{blue}/v_{red} in Table 1 and the contours go from 5 to 50σ in steps of 5σ. Symbols are the same as Figure 2. The right panel shows the mass spectrum with fit. Symbols are the same as Figure 6.

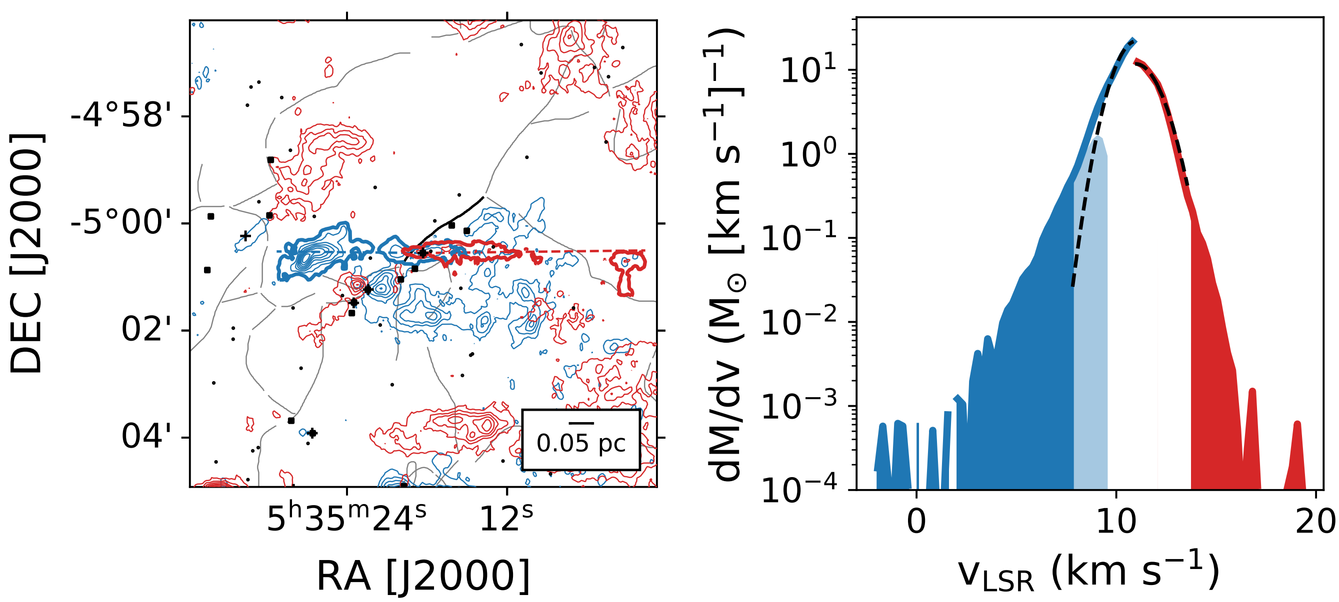

Figure 37: HOPS 92 outflow. The left panel shows the outflow, position angle, nearby sources, and filaments. The velocity range of integration is given by v_{blue}/v_{red} in Table 1 and the contours go from 5 to 50σ in steps of 5σ. Symbols are the same as Figure 2. The right panel shows the mass spectrum with fit. Symbols are the same as Figure 6.

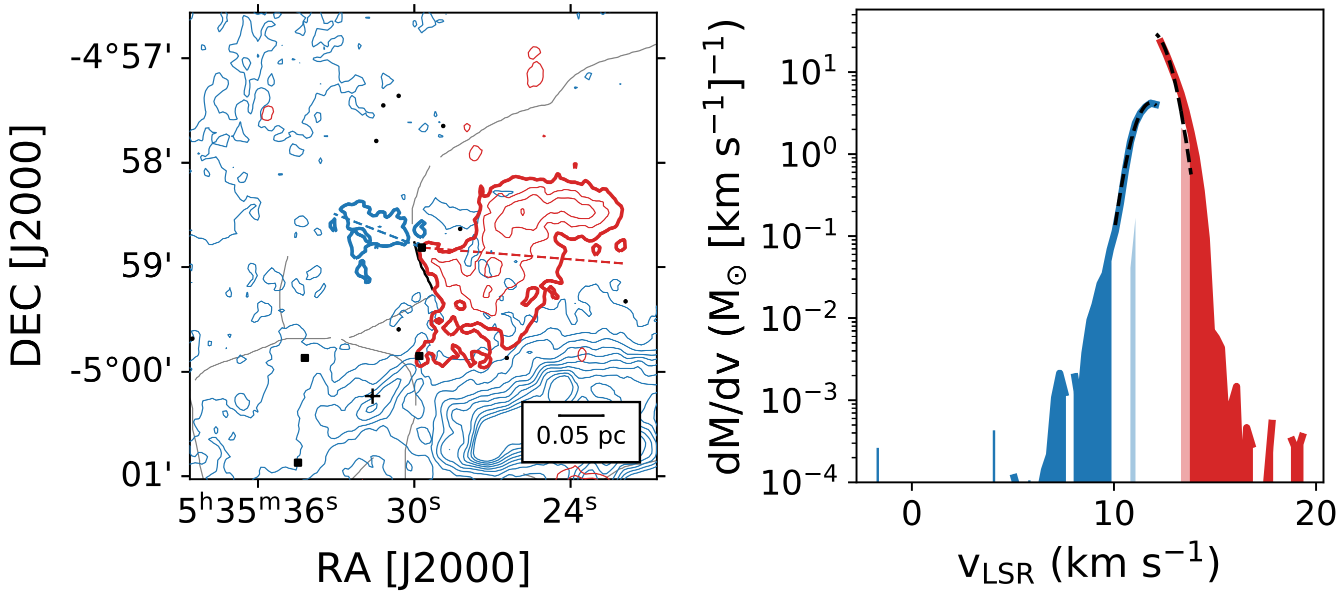

Figure 38: HOPS 96 outflow. The left panel shows the outflow, position angle, nearby sources, and filaments. The velocity range of integration is given by v_{blue}/v_{red} in Table 1 and the contours go from 5 to 50σ in steps of 5σ. Symbols are the same as Figure 2. The right panel shows the mass spectrum with fit. Symbols are the same as Figure 6.

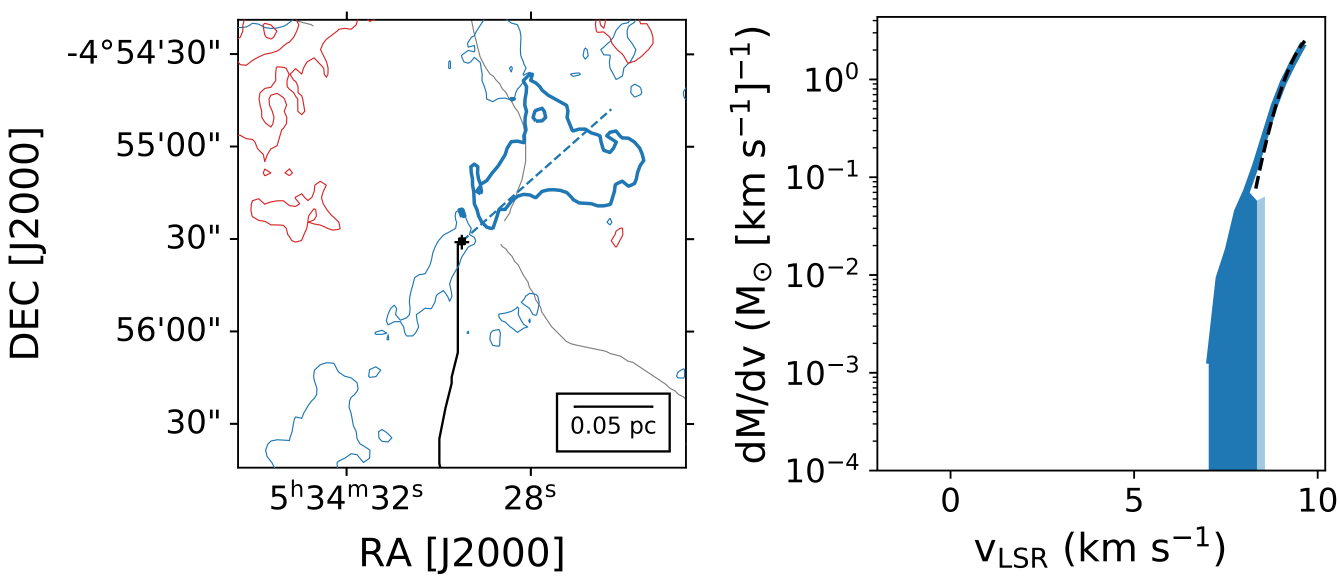

Figure 39: HOPS 99 outflow. The left panel shows the outflow, position angle, nearby sources, and filaments. The velocity range of integration is given by v_{blue}/v_{red} in Table 1 and the contours go from 5 to 50σ in steps of 5σ. Symbols are the same as Figure 2. The right panel shows the mass spectrum with fit. Symbols are the same as Figure 6.

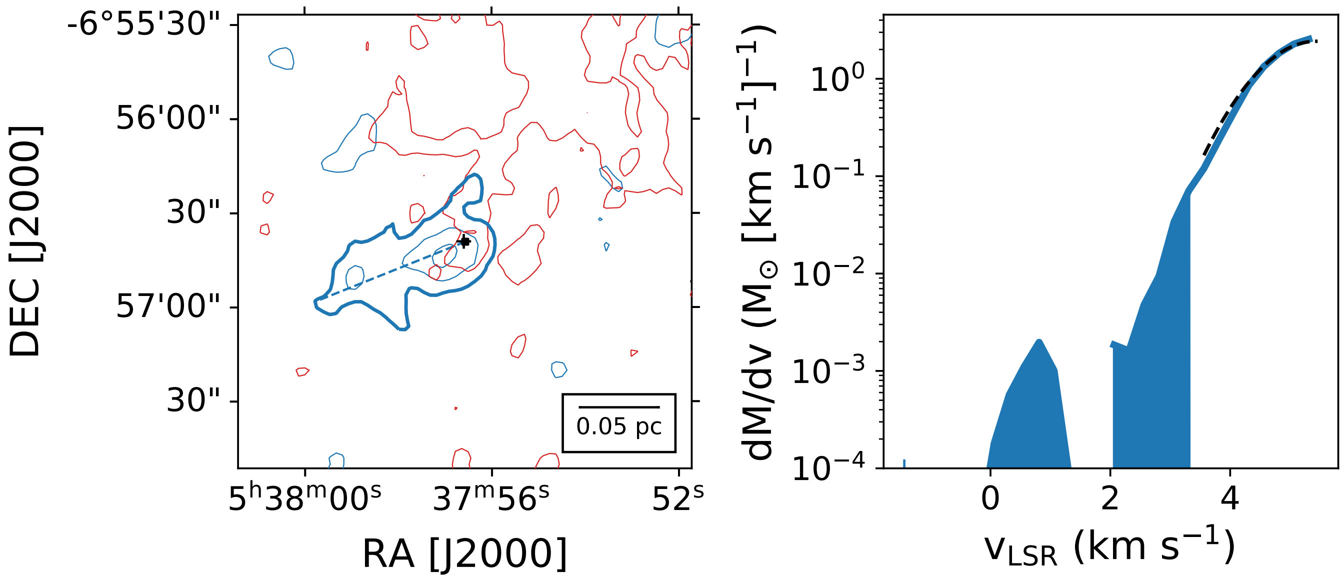

Figure 40: HOPS 157 outflow. The left panel shows the outflow, position angle, nearby sources, and filaments. The velocity range of integration is given by v_{blue}/v_{red} in Table 1 and the contours go from 5 to 50σ in steps of 5σ. Symbols are the same as Figure 2. The right panel shows the mass spectrum with fit. Symbols are the same as Figure 6.

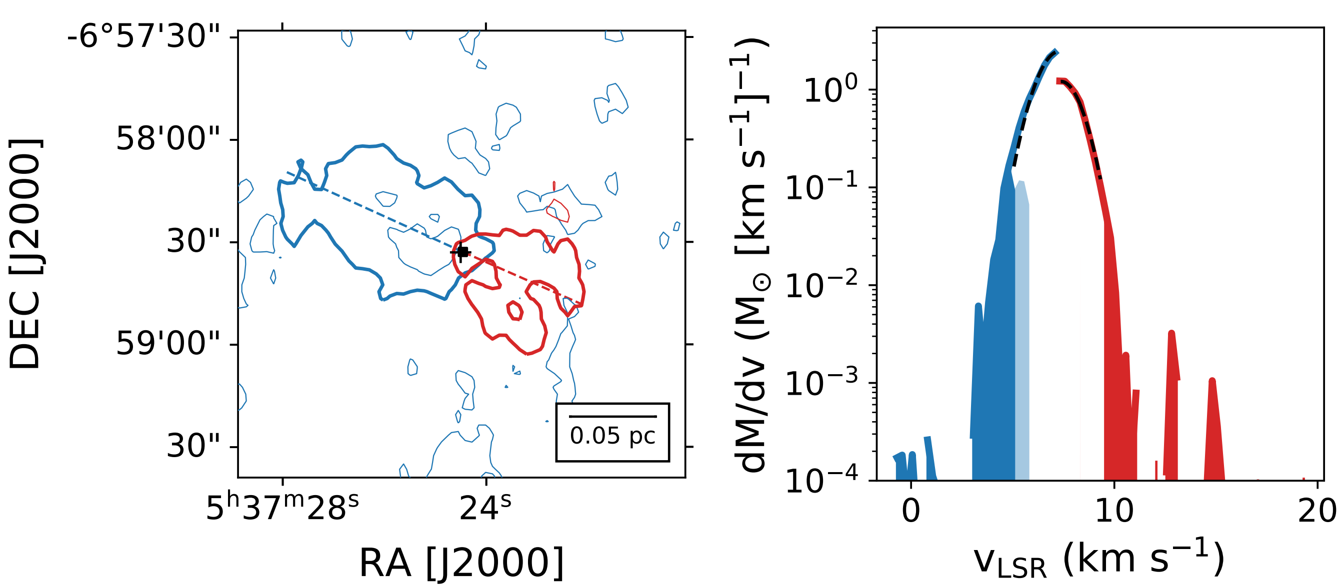

Figure 41: HOPS 158 outflow. The left panel shows the outflow, position angle, nearby sources, and filaments. The velocity range of integration is given by v_{blue}/v_{red} in Table 1 and the contours go from 5 to 50σ in steps of 5σ. Symbols are the same as Figure 2. The right panel shows the mass spectrum with fit. Symbols are the same as Figure 6.

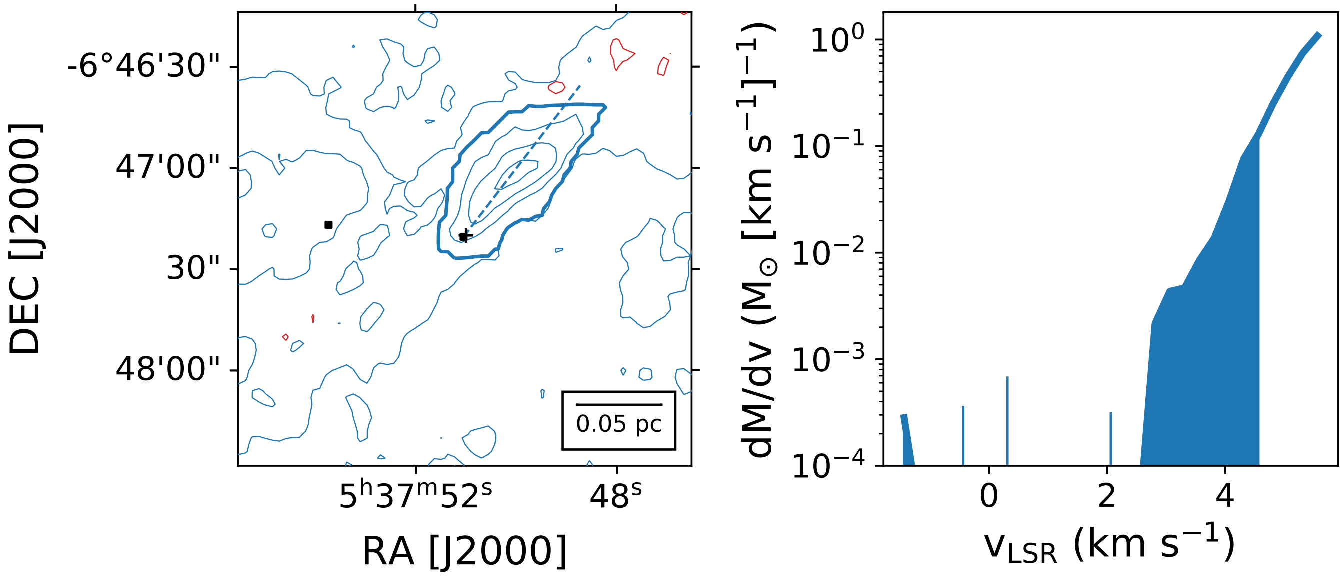

Figure 42: HOPS 160 outflow. The left panel shows the outflow, position angle, nearby sources, and filaments. The velocity range of integration is given by v_{blue}/v_{red} in Table 1 and the contours go from 5 to 50σ in steps of 5σ. Symbols are the same as Figure 2. The right panel shows the mass spectrum with fit. Symbols are the same as Figure 6.

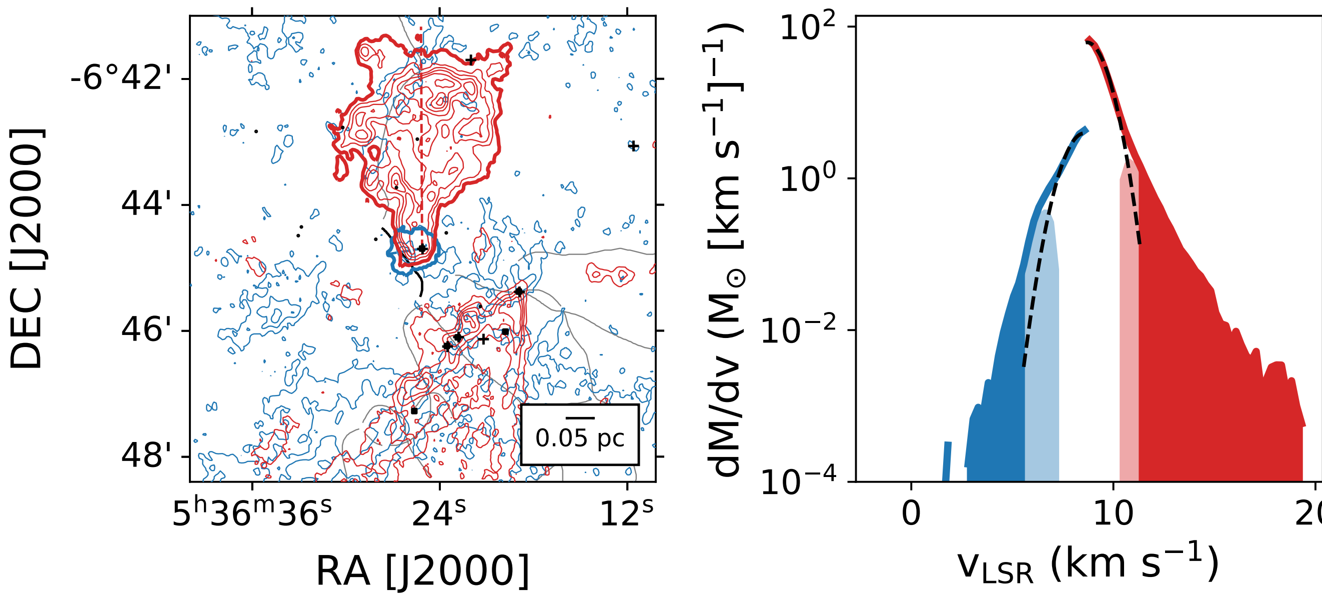

Figure 43: HOPS 166 outflow. The left panel shows the outflow, position angle, nearby sources, and filaments. The velocity range of integration is given by v_{blue}/v_{red} in Table 1 and the contours go from 5 to 50σ in steps of 5σ. Symbols are the same as Figure 2. The right panel shows the mass spectrum with fit. Symbols are the same as Figure 6.

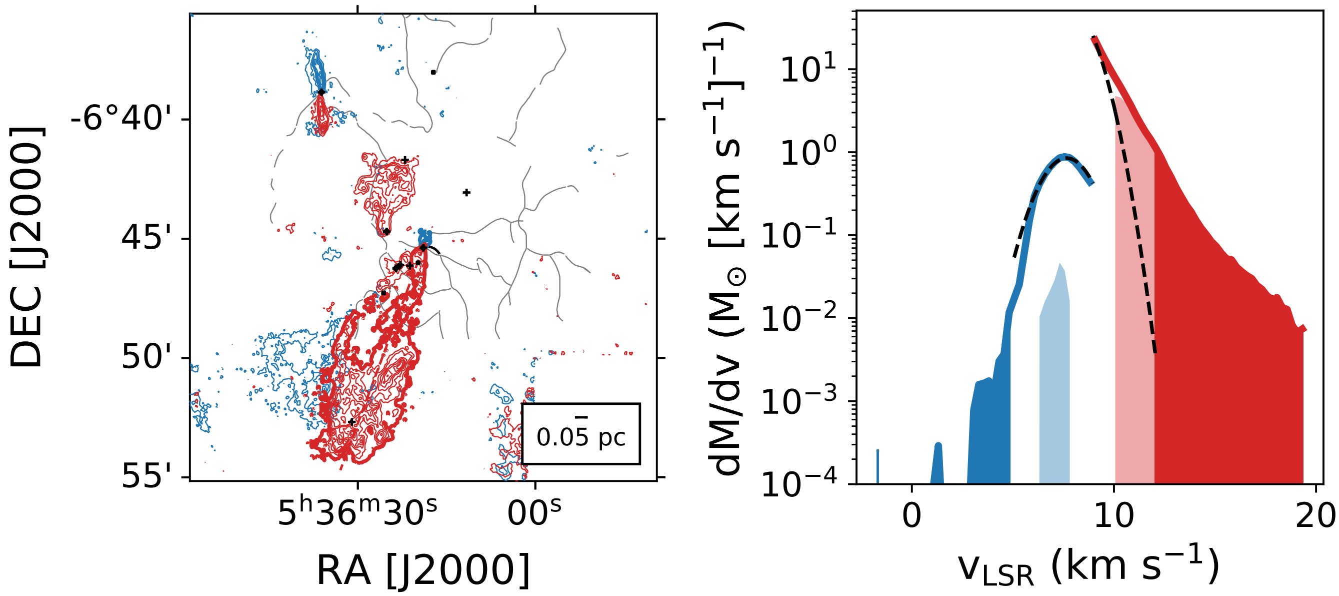

Figure 44: HOPS 168 outflow. The left panel shows the outflow, position angle, nearby sources, and filaments. The velocity range of integration is given by v_{blue}/v_{red} in Table 1 and the contours go from 5 to 50σ in steps of 5σ. Symbols are the same as Figure 2. The right panel shows the mass spectrum with fit. Symbols are the same as Figure 6.

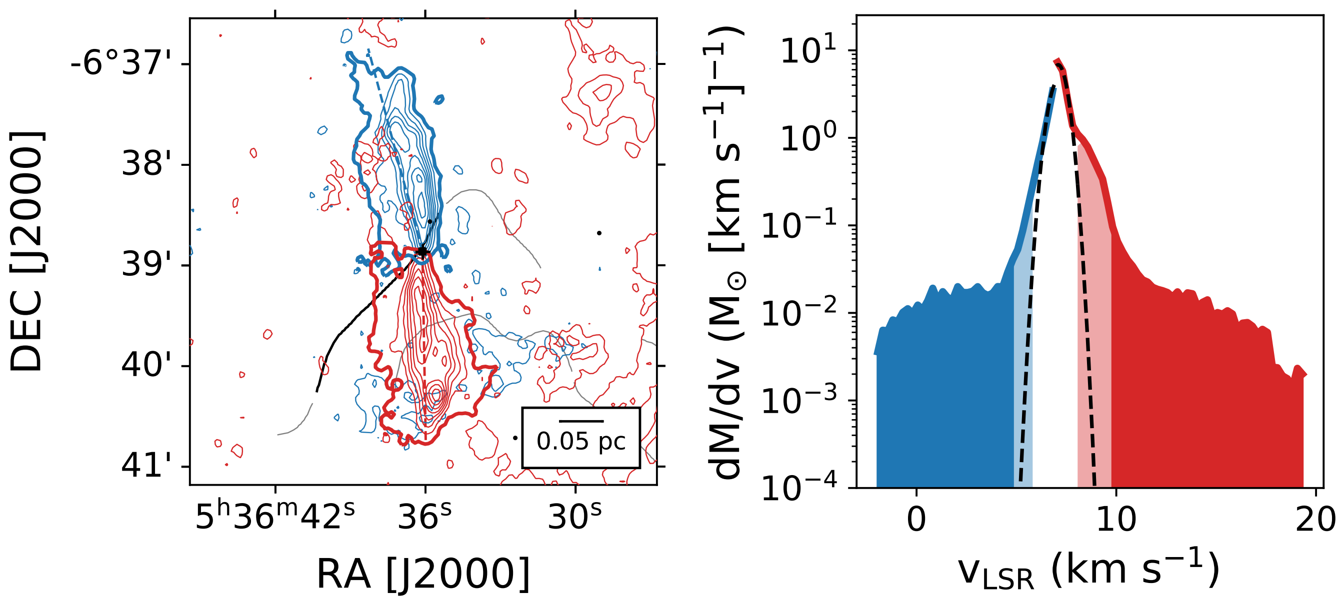

Figure 45: HOPS 169 outflow. The left panel shows the outflow, position angle, nearby sources, and filaments. The velocity range of integration is given by v_{blue}/v_{red} in Table 1 and the contours go from 5 to 50σ in steps of 5σ. Symbols are the same as Figure 2. The right panel shows the mass spectrum with fit. Symbols are the same as Figure 6.

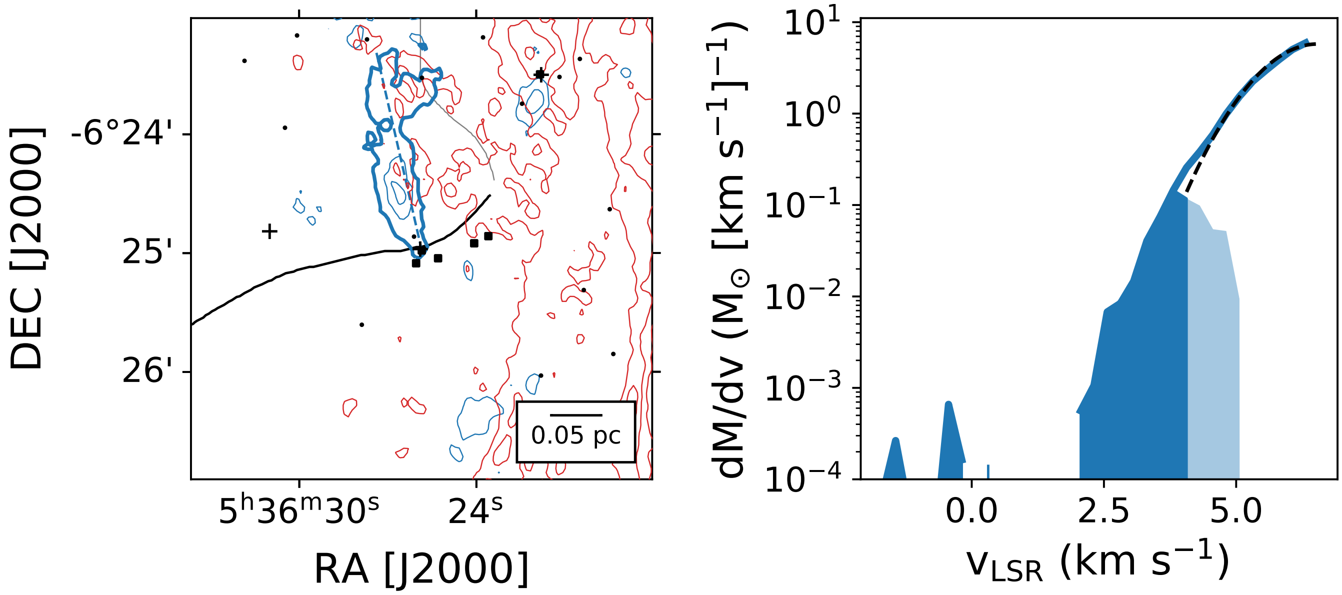

Figure 46: HOPS 174 outflow. The left panel shows the outflow, position angle, nearby sources, and filaments. The velocity range of integration is given by $v_{\rm blue}/v_{\rm red}$ in Table 1 and the contours go from 5 to 50σ in steps of 5σ. Symbols are the same as Figure 2. The right panel shows the mass spectrum with fit. Symbols are the same as Figure 6.

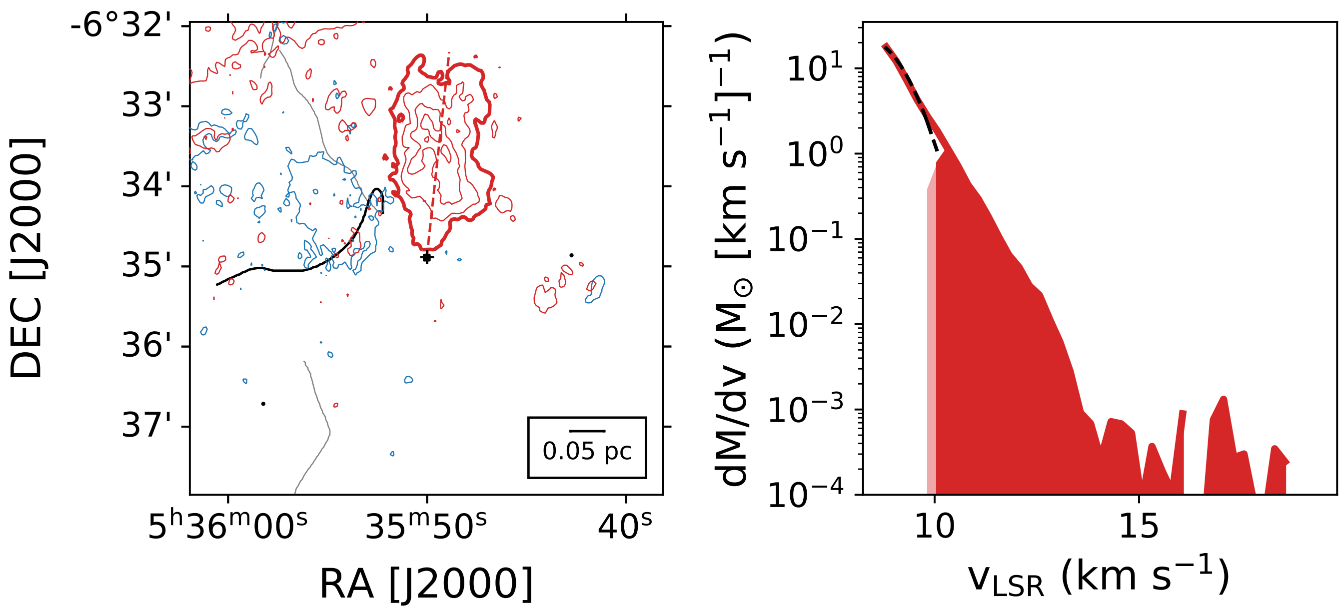

Figure 47: HOPS 177 outflow. The left panel shows the outflow, position angle, nearby sources, and filaments. The velocity range of integration is given by $v_{\rm blue}/v_{\rm red}$ in Table 1 and the contours go from 5 to 50σ in steps of 5σ. Symbols are the same as Figure 2. The right panel shows the mass spectrum with fit. Symbols are the same as Figure 6.

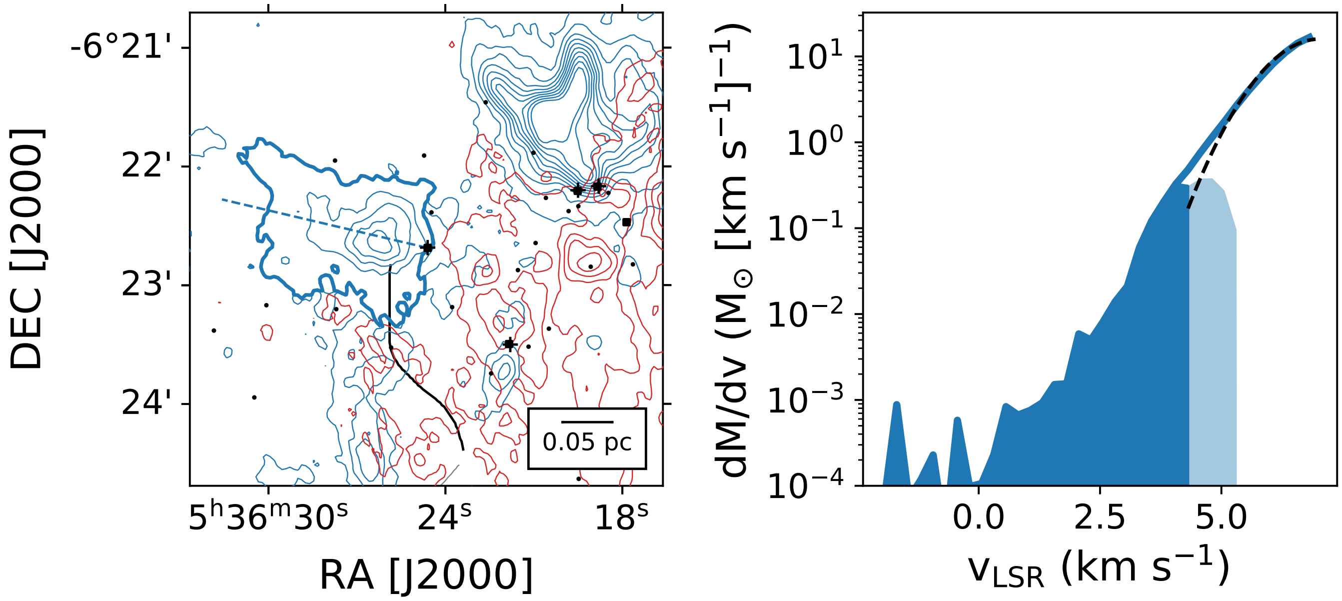

Figure 48: HOPS 178 outflow. The left panel shows the outflow, position angle, nearby sources, and filaments. The velocity range of integration is given by v_{blue}/v_{red} in Table 1 and the contours go from 5 to 50σ in steps of 5σ. Symbols are the same as Figure 2. The right panel shows the mass spectrum with fit. Symbols are the same as Figure 6.

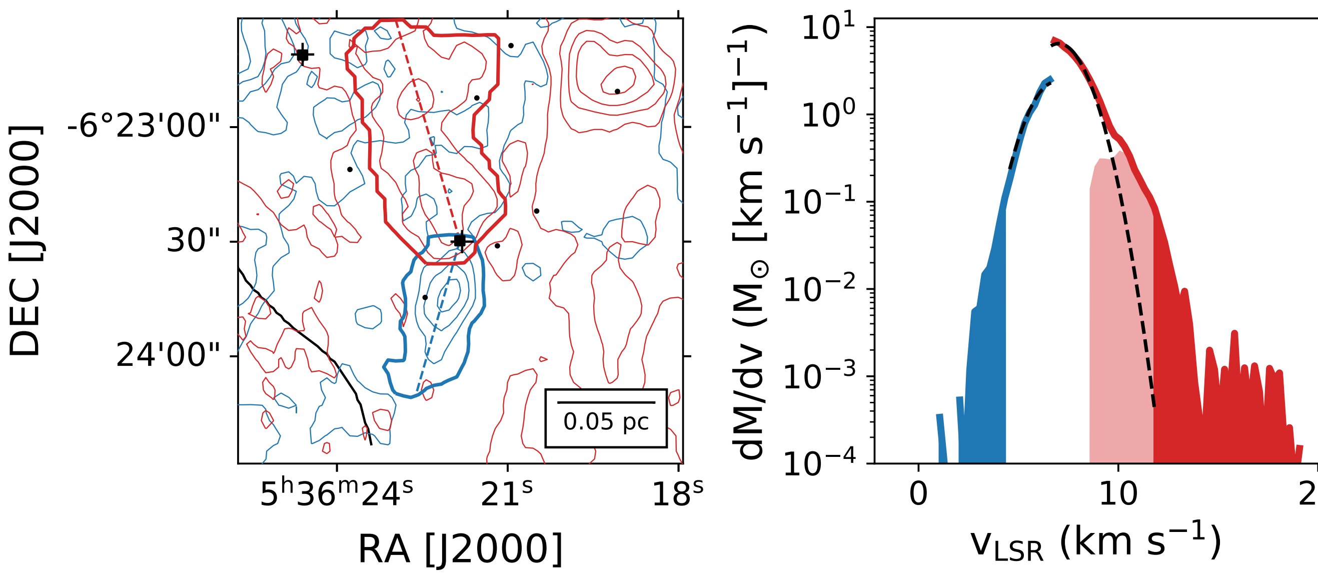

Figure 49: HOPS 179 outflow. The left panel shows the outflow, position angle, nearby sources, and filaments. The velocity range of integration is given by v_{blue}/v_{red} in Table 1 and the contours go from 5 to 50σ in steps of 5σ. Symbols are the same as Figure 2. The right panel shows the mass spectrum with fit. Symbols are the same as Figure 6.

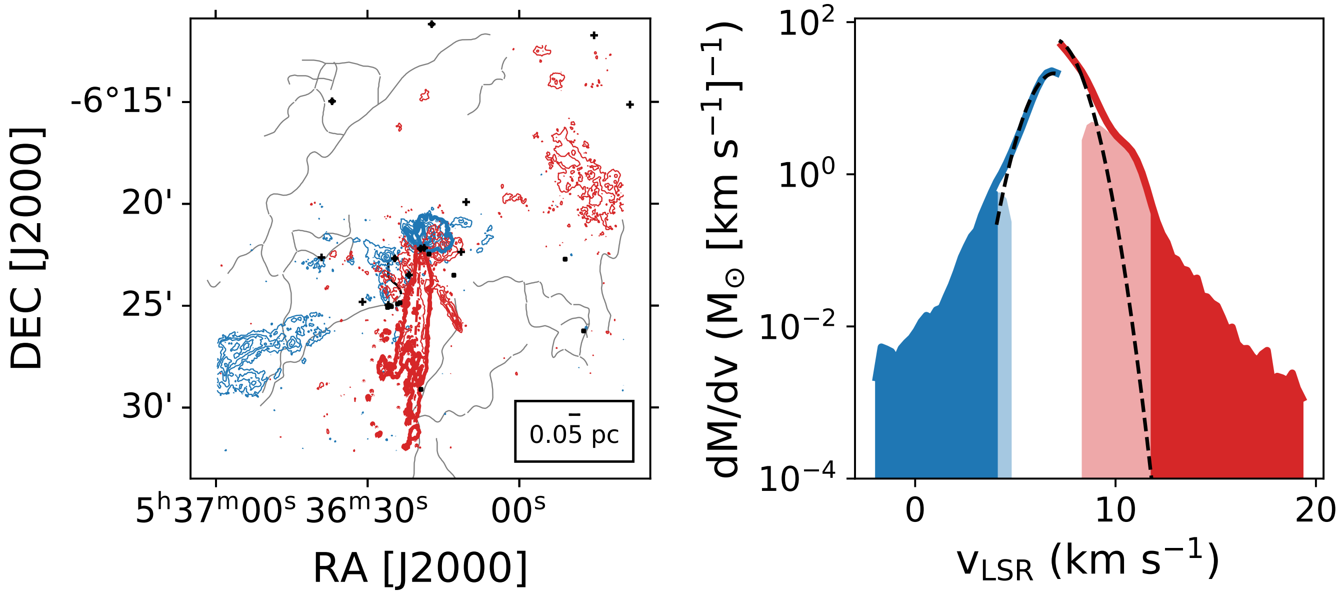

Figure 50: HOPS 181 outflow. The left panel shows the outflow, position angle, nearby sources, and filaments. The velocity range of integration is given by v_{blue}/v_{red} in Table 1 and the contours go from 5 to 50σ in steps of 5σ. Symbols are the same as Figure 2. The right panel shows the mass spectrum with fit. Symbols are the same as Figure 6.

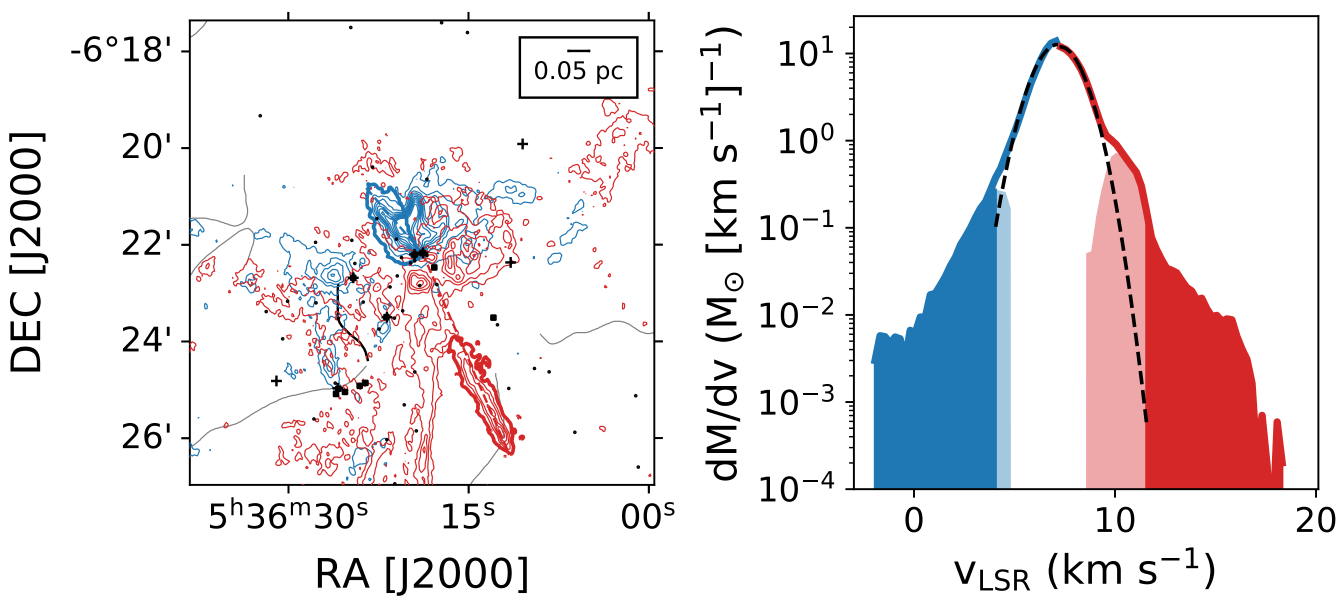

Figure 51: HOPS 182 outflow. The left panel shows the outflow, position angle, nearby sources, and filaments. The velocity range of integration is given by v_{blue}/v_{red} in Table 1 and the contours go from 5 to 50σ in steps of 5σ. Symbols are the same as Figure 2. The right panel shows the mass spectrum with fit. Symbols are the same as Figure 6.

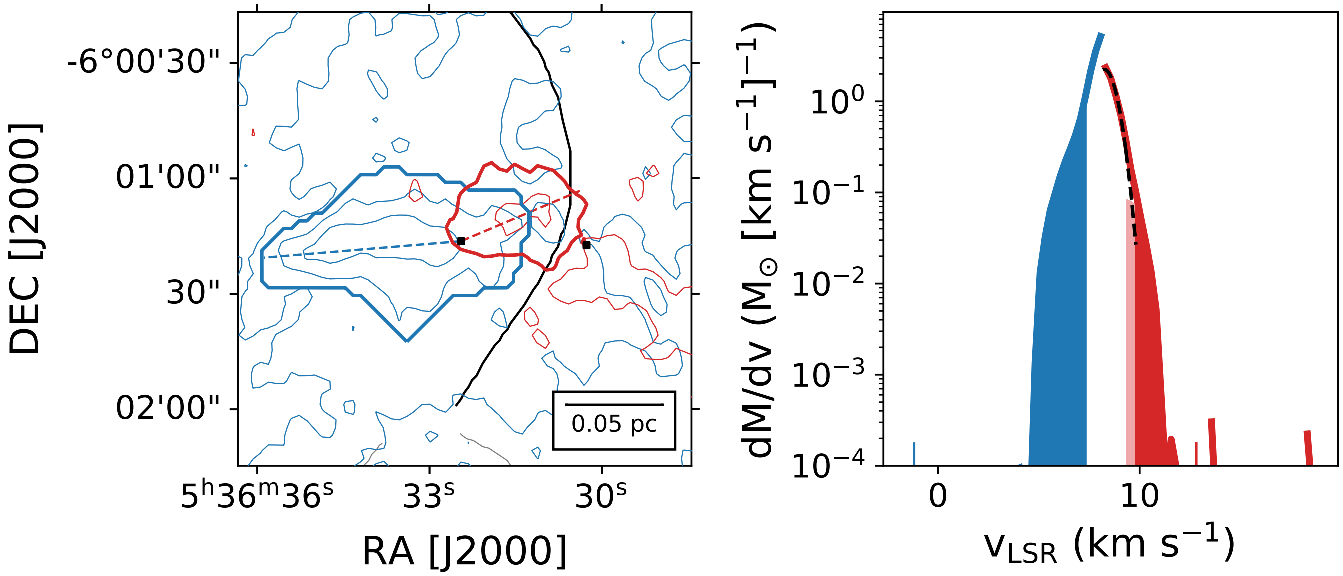

Figure 52: HOPS 192 outflow. The left panel shows the outflow, position angle, nearby sources, and filaments. The velocity range of integration is given by $v_{\rm blue}/v_{\rm red}$ in Table 1 and the contours go from 5 to 50σ in steps of 5σ. Symbols are the same as Figure 2. The right panel shows the mass spectrum with fit. Symbols are the same as Figure 6.

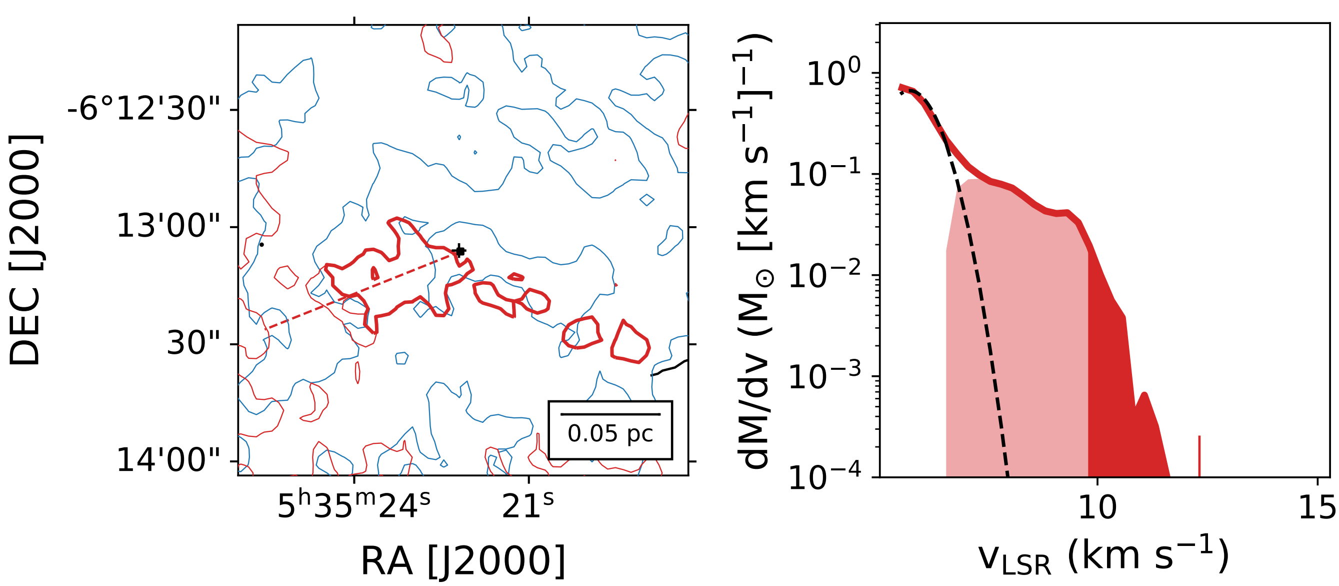

Figure 53: HOPS 198 outflow. The left panel shows the outflow, position angle, nearby sources, and filaments. The velocity range of integration is given by $v_{\rm blue}/v_{\rm red}$ in Table 1 and the contours go from 5 to 50σ in steps of 5σ. Symbols are the same as Figure 2. The right panel shows the mass spectrum with fit. Symbols are the same as Figure 6.

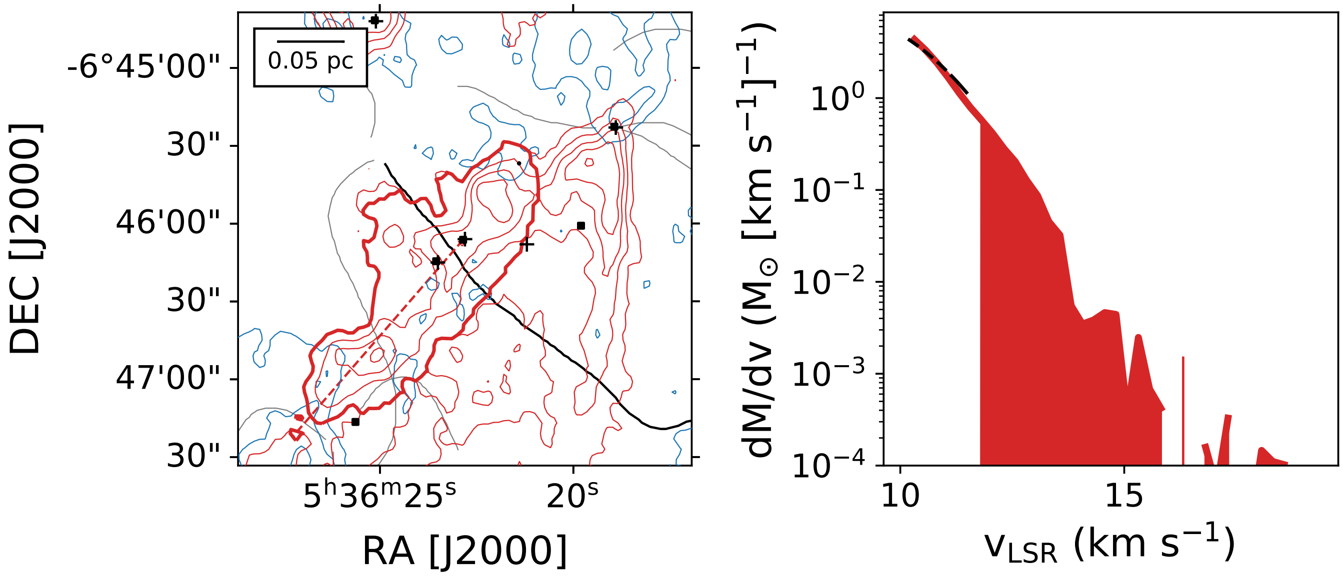

Figure 54: HOPS 203 outflow. The left panel shows the outflow, position angle, nearby sources, and filaments. The velocity range of integration is given by v_{blue}/v_{red} in Table 1 and the contours go from 5 to 50σ in steps of 5σ. Symbols are the same as Figure 2. The right panel shows the mass spectrum with fit. Symbols are the same as Figure 6.

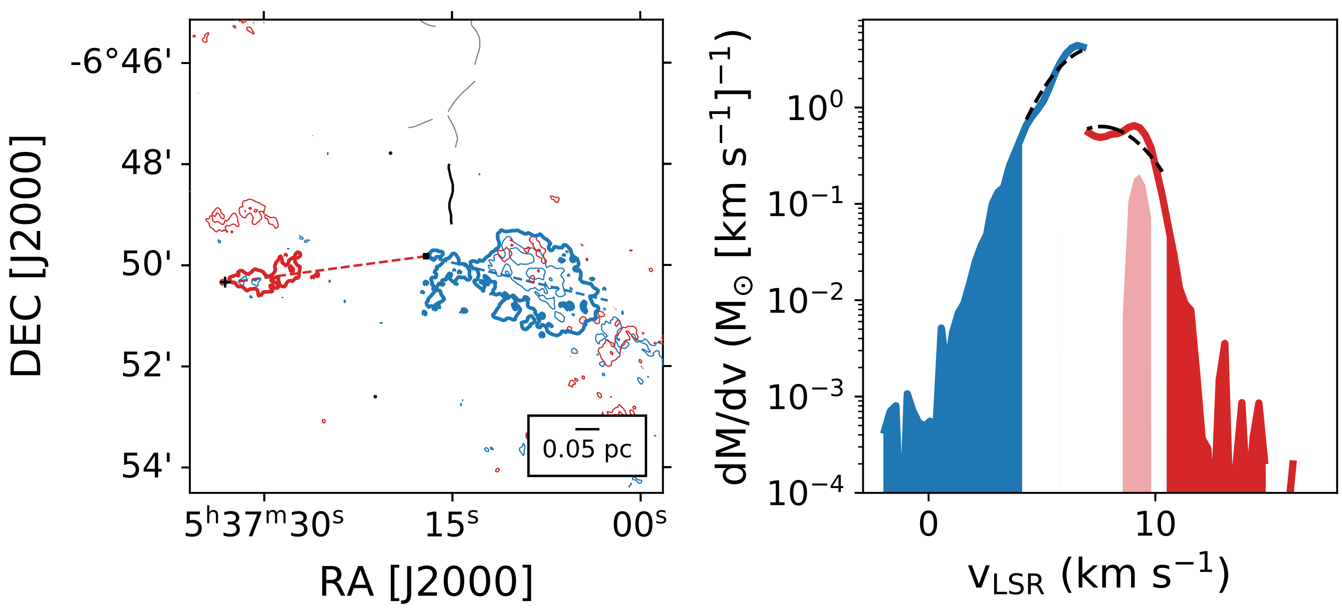

Figure 55: HOPS 355 outflow. The left panel shows the outflow, position angle, nearby sources, and filaments. The velocity range of integration is given by v_{blue}/v_{red} in Table 1 and the contours go from 5 to 50σ in steps of 5σ. Symbols are the same as Figure 2. The right panel shows the mass spectrum with fit. Symbols are the same as Figure 6.

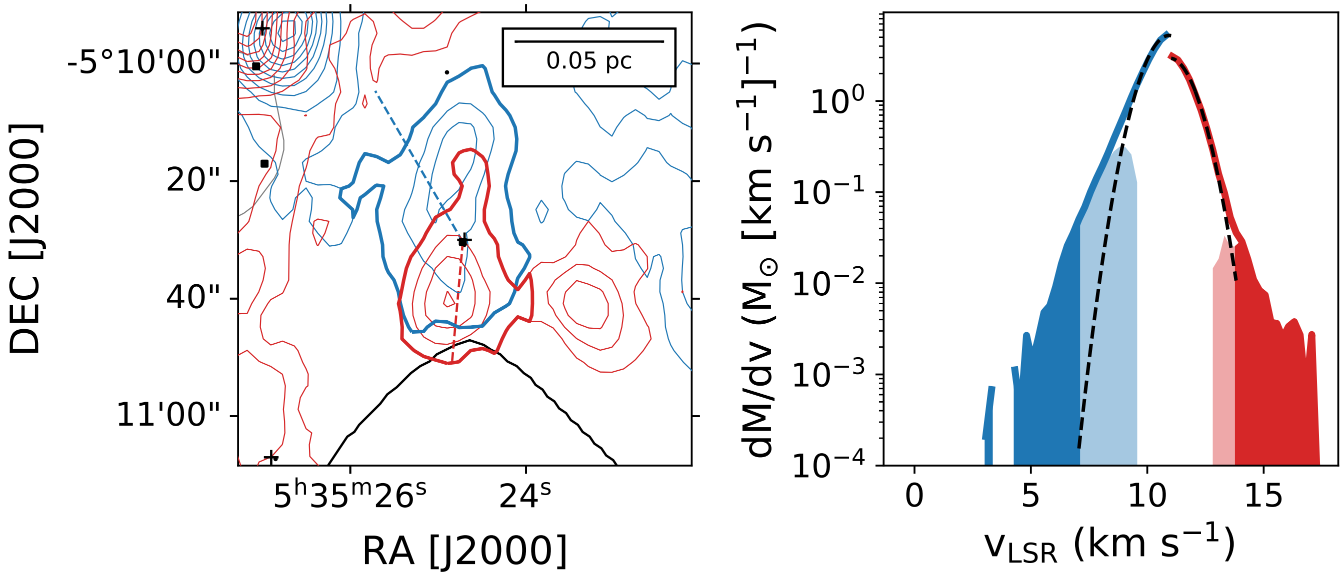

Figure 56: HOPS 368 outflow. The left panel shows the outflow, position angle, nearby sources, and filaments. The velocity range of integration is given by v_{blue}/v_{red} in Table 1 and the contours go from 5 to 50σ in steps of 5σ. Symbols are the same as Figure 2. The right panel shows the mass spectrum with fit. Symbols are the same as Figure 6.

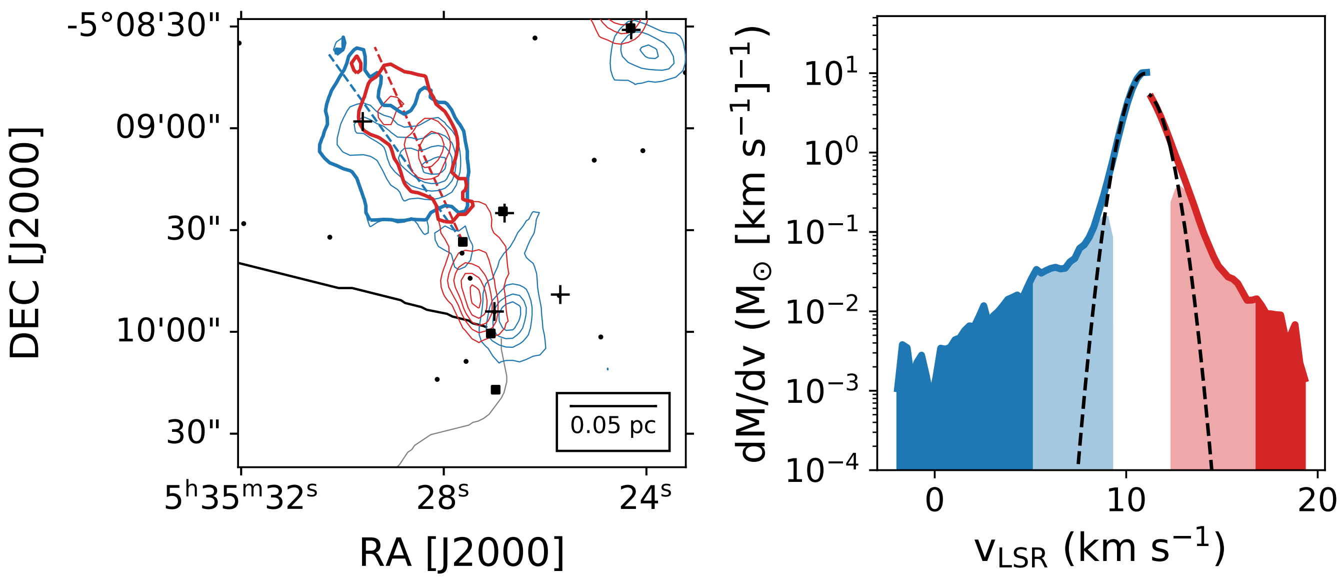

Figure 57: HOPS 370 outflow. The left panel shows the outflow, position angle, nearby sources, and filaments. The velocity range of integration is given by v_{blue}/v_{red} in Table 1 and the contours go from 5 to 50σ in steps of 5σ. Symbols are the same as Figure 2. The right panel shows the mass spectrum with fit. Symbols are the same as Figure 6.

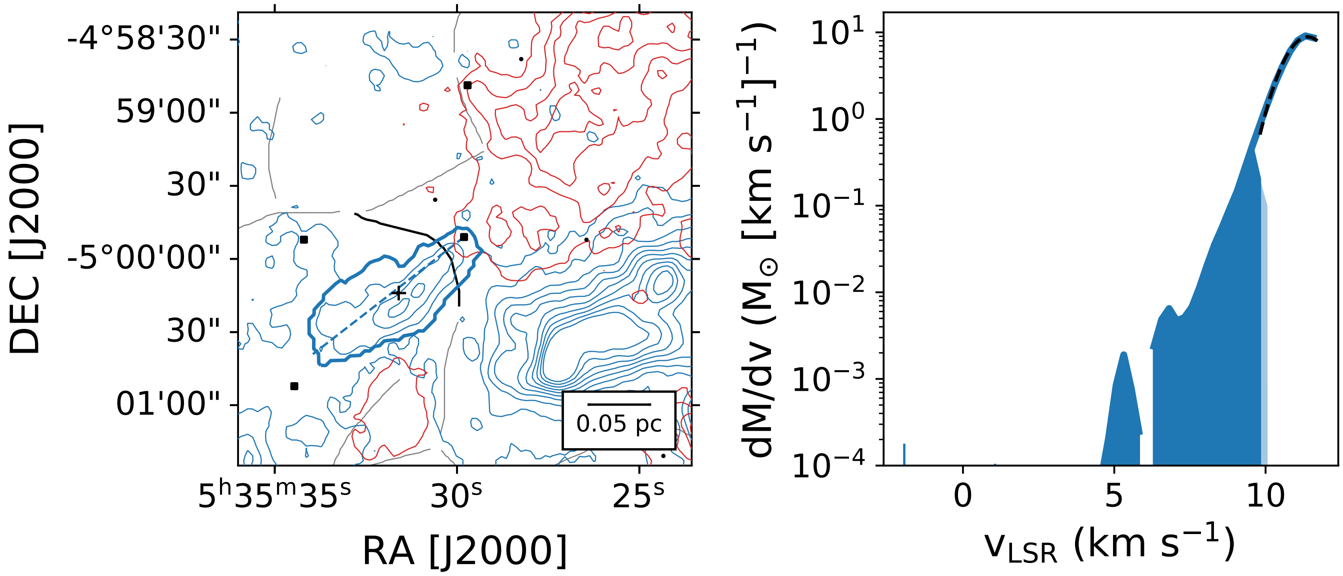

Figure 58: HOPS 383 outflow. The left panel shows the outflow, position angle, nearby sources, and filaments. The velocity range of integration is given by v_{blue}/v_{red} in Table 1 and the contours go from 5 to 50σ in steps of 5σ. Symbols are the same as Figure 2. The right panel shows the mass spectrum with fit. Symbols are the same as Figure 6.